Assembly of Disk Galaxies from the Peak of Cosmic Star-Formation to Today

by

Raymond Clifford Simons

A dissertation submitted to The Johns Hopkins University in conformity with the requirements for the degree of Doctor of Philosophy.

Baltimore, Maryland

June, 2018

Abstract

It was once accepted that galaxies form and maintain thin gas disks at early times. As gas is collisional, its disordered motions should be suppressed quickly. With angular momentum conserved, galaxies should be rotationally-supported within a few galaxy crossing times of their initial formation. The results presented over the chapters of this thesis challenge this picture.

We track the evolution of the ionized gas kinematics of star-forming galaxies from $z = 2$ to the present day, covering 10 Gyrs in cosmic time. First, as a part of a Keck/MOSFIRE spectroscopic survey, we determine that $z = 2$ (3 Gyr after the Big Bang) is still a period of active disk formation. The majority of massive star-forming galaxies at this time have disk-like characteristics — their kinematics are dominated by rotation, they are consistent with a marginally stable disk model, and they form a Tully-Fisher relation — but with disordered motions much higher than galaxies today. These galaxies are unlike disks today — less than 30% of galaxies at all masses have rotational motions at least 3x higher than their disordered motions. Lower mass galaxies are still in the early stages of disk assembly — their kinematics are often

ABSTRACT

dominated by disordered motions and they fall short of the Tully-Fisher relation. Combining this sample with a similar one at $z < 1$, we find that all star-forming galaxy populations, on average, increase in rotational-support with time from $z = 2$ to now. This happens through a dramatic decline in disordered motions, and a mild increase in rotational motions. By the present day, nearly all star-forming galaxies above a stellar mass of $10^{9.5}$ $M_{\odot}$ have formed rotationally-supported disks with regular disk-like morphologies, while below this mass a galaxy may or may not form a disk. To better understand potential biases when interpreting these and other observations, we compare mock images and spectra of realistic hydrodynamic simulations against their intrinsic dynamical state. We determine that late-stager mergers are indistinguishable from disks in seeing-limited kinematic data. This implies that the fraction of galaxies that are measured to be "disks" from seeing-limited observations at $z = 2$ is only an *upper-limit* on the true disk fraction. Using theoretically-derived close pair fractions at $z = 2$, we determine that this effect is significant for low mass galaxies — up to a factor of 2 difference between observed and true disk fractions — but insignificant for high mass galaxies.

Primary Reader: Susan A. Kassin

Secondary Reader: Timothy M. Heckman

Acknowledgments

This work would not have been possible without the love and support of my family, friends, and colleagues.

First, I would like to thank my advisor, Dr. Susan A. Kassin. Thank you for teaching me to always keep an open mind, to respect the data before the model, to question accepted truths, and to always strive to improve as a scientist. Thank you for helping me understand which problems are worth pursuing and which rabbit holes are worth avoiding. Thank you for spending countless hours revising my sloppy sentences and for teaching me how to write good [sic]. Thank you for introducing me to this field — supporting travel to numerous conferences and workshops — and the people in it. Thank you for being a trusted friend. I also need to acknowledge and thank the other members of Susan's group — Greg, Camilla, Alex and Weichen — who have taught me a great deal over these years. I cherish our fun and lively group meeting discussions.

Thank you to Prof. Jon Trump, who provided funding for one of the key Keck/MOSFIRE observing runs in January 2014. Thank you to Dr. Ben Weiner, who provided soft-

ware for analyzing the observational data. Thank you to Profs. Sandy Faber, David Koo, and Joel Primack for serving as gracious hosts during my several trips to UC Santa Cruz and for years of fruitful discussions. Thank you to all of the members of my thesis committee, who have been an invaluable resource.

Thank you to Jess for coming into my life in November 2016 and for making me more happy than I knew possible. I look forward to spending the rest of my life with you. Thank you to my dad, mom, brothers, sister, and grandparents. Without their love, I would not be where I am today. Thank you to all of the friends I've met in grad school. You've kept me in good spirits over the years. I would especially like to thank Duncan for sticking with me as a roommate for six years.

Finally, I would like to acknowledge the uncountable number of colleagues and friends in the Bloomberg and Muller buildings who make coming into work everyday, and doing what we are so fortunate to do, as fun as the previous day.

Dedication

for my parents, grandparents, brothers, sister, and Jess

Contents

List of Tables

List of Figures

LIST OF FIGURES

Chapter 1

Introduction

This introduction gives brief, non-exhaustive context to the rest of the thesis. We start with a short review of galaxy formation and growth in ΛCDM (§1.1, §1.2). Then, we discuss galaxy kinematics and kinematic scaling relations (§1.3), briefly review the state of the literature (§1.4) and, finally, outline the chapters of the thesis (§1.5). Each chapter is supplemented with its own focused introduction.

1.1 Standard Picture of Disk Galaxy Formation in ΛCDM

The majority of today's massive star-forming galaxies are disks. When and how do these galaxies develop rotational-support? These are long-standing questions.

Overview: In the standard picture, baryons and dark matter are endowed with

angular momentum in the early universe (Peebles, 1969). Baryonic gas, being collisional, will eventually cool and condense into the gravitational centers of dark matter halos (Blumenthal et al., 1984). Assuming gas conserves its angular momentum as it cools, the first galaxies will take shape as thin, rotationally-supported disks (Fall & Efstathiou, 1980; Mo et al., 1998). Unless transformed into ellipticals through merging (Toomre, 1977), they survive as disks to the present — i.e., today's rotating disks have been rotating since formation. We now briefly review this picture.

Structure Formation: Following the initial rapid inflation of the Universe, the density of matter — baryonic (protons, neutrons, electrons, neutrinos) and dark (of unknown composition, but assumed thermally cold) — is nearly uniform, but not perfectly so.

In sufficiently over-dense regions, dark matter will collapse via gravitational instabilities to form small irregular protohalos (Zel'dovich, 1970; Peebles, 1980), themselves clustered and beaded along an emerging large-scale filamentary structure, dubbed the cosmic web (Klypin & Shandarin, 1983; Bond et al., 1996). As the Universe expands, and the cosmic radiation field cools, electrons and protons eventually combine together to form neutral atoms. These baryons, now uncoupled and unsupported by cosmic radiation pressure, are dragged into the dark matter protohalos through gravity. At the interface between the protohalo and the intergalactic medium, i.e., the virial radius, cold gas shock heats to the virial temperature of the protohalo (Rees & Ostriker, 1977; White & Rees, 1978; White & Frenk, 1991).

Baryons and Dark Matter Acquire Angular Momentum: Shortly after recombination, dark matter and baryons are co-located in the cosmic web — clumped in protohalos with elongated and irregular structure. Their irregular 3D structure gives them a quadrupole moment. This moment enables long-range gravitational torquing from nearby structure in the cosmic web. These "tidal torques" endow the dark and baryonic matter with angular momentum (Hoyle, 1951; Peebles, 1969; Doroshkevich, 1970; White, 1984). This process becomes ineffective after the (proto-) halo halts its expansion and virializes.

Thin Disks Should Form Fast: Gas is collisional, and so should not remain in a state of high velocity dispersion for long. High-dispersion gas will shock-heat, radiatively cool its kinetic energy, and sink to the gravitational center of its host halo (Blumenthal et al., 1984). With angular momentum from the tidal torques conserved (Fall & Efstathiou, 1980; Mo et al., 1998), cooling gas will spin up as it sinks to the center. *Gas in the first galaxies should be dominated by rotational motions.*

This process should happen fast. Consider a halo with a virial radius defined such that average internal mass density $\overline{\rho}(< R_{vir})$ is 200 times the critical density of the Universe ρ_{crit}. The dynamical timescale, i.e., the time it takes for free-fall collapse, at the virial radius is $\tau_{dyn}(R_{vir}) \simeq (200\,\rho_{crit}\,G)^{-1/2} = 2.8$ Gyr. If the density of the halo within the virial radius takes the form of a simple singular isothermal sphere, i.e., $\overline{\rho}(< r) \propto \rho(r) \propto 1/r^2$, then $\tau_{dyn}(r) = \tau_{dyn}(R_{vir}) \times (r/R_{vir})$.

At the center of the halo, the dynamical time is short — less than 280 Myr inside

0.1 R_{vir} — and is progressively larger at large radii.

Gas should shock heat, radiatively cool and form a thin rotating disk only a few hundred million years after the halo virializes.

1.2 Complicating the Picture: Stellar Feedback, Mergers, and Mass Accretion

This picture — of the smooth, orderly, and fast development of rotational-support — however, is complicated by additional processes.

Stellar Feedback: Where gas is sufficiently dense and cold, stars will form. These stars will take on a distribution in mass (Chabrier, 2003; Kroupa, 2001) — most at or below the mass of the sun ($M_\odot$), with a handful a few or tens times $M_\odot$. The most massive of these stars, O and B stars, are short-lived ($\sim$10 Myr) and end their lives in violent core-collapse supernovae explosions (SNe). Each SNe will send a blast wave through the interstellar medium (ISM) and impart random kinetic energy/momentum into the ISM (McKee & Ostriker, 1977; Silk, 1997). These blast waves disrupt existing motions and stir turbulence in the surrounding gas (Dib et al., 2006; Joung & Mac Low, 2006). If the specific mechanical energy injected into the gas is comparable to the gravitational potential of the galaxy, a substantial fraction of the ISM will be removed (Dekel & Silk, 1986; Strickland & Heckman, 2009). In more massive galaxies, most of this ejected gas will fall back, but not before cycling through, and

interacting with, the circumgalactic medium (Übler et al., 2014; Ford et al., 2014; Muratov et al., 2017). These dynamically violent SNe-induced outflows/inflows are thought to play a leading role in regulating the gas content, and thus stellar mass growth, of high-redshift galaxies (Bouché et al., 2010; Davé et al., 2012; Dekel & Mandelker, 2014).

Mergers and Mass Accretion: Following their initial formation, haloes grow through hierarchical merging (White & Rees, 1978) — with smaller halos merging to form bigger halos. Each halo brings one or more galaxies with it. These accreted galaxies are either destroyed on infall, maintain a stable and long-lasting orbit as a satellite or, through dynamical friction, merge with the central galaxy.

Galaxy - galaxy mergers are gravitationally violent, especially in cases where the galaxies are of similar mass. Mergers tend to rearrange angular momentum and reshape existing galaxy structure (Naab & Burkert, 2003). As gas-rich galaxies merge, they tend to induce short-lived, starbursts (Hernquist & Mihos, 1995), from which a new, dynamically hotter disk will form (Robertson et al., 2006; Hopkins et al., 2009; Governato et al., 2009; Snyder et al., 2015).

Galaxies accrete mass through means other than merging, too. Although yet to be detected, cold flow accretion along the cosmic web is thought to be the dominant form of mass accretion at high redshift. Unlike smooth cooling from the hot gaseous halo — which is dynamically quiet and undisruptive — cold mode accretion can inject random kinetic energy into a galaxy, rearranging its angular momentum in the process

(Kimm et al., 2011; Danovich et al., 2015).

1.3 Galaxy Kinematics

These processes affect the internal motions of a galaxy. They tend to destroy ordered motion and elevate disordered motion — the former being the rotation velocity (V_{rot}) and the latter being the velocity dispersion (σ_g[1]).

These motions, hereafter refereed to as "kinematics", can be measured from the doppler shifting of spectral features, relative to the net velocity of the galaxy. An emission line will blueshift if emitted from an object moving away from an observer, and redshift if emitted from an object moving towards an observer. For a collection of randomly-moving emitters, i.e., each with a random blueshift or redshift relative to the bulk motion of the collection, an emission line will be broadened. The rotation velocity and velocity dispersion can be readily measured from the center and width of observed emission lines (examples shown in Chapter 2 and 3).

Kinematics are typically measured from the bright optical emission lines, e.g., Hα, [OIII]λ5007, and [OII]λ3727. These lines are generated in hot, ionized regions around massive, short-lived O and B stars. As such, they trace the active star-forming regions of galaxies.

As galaxies are gravitationally-bound systems, their internal motions are intimately tied to their total mass. This manifests in the Tully-Fisher relation (Tully &

[1]Unless otherwise noted, σ_g refers to the 1D line-of-sight velocity dispersion of the ionized gas.

Fisher 1977) for rotationally-supported disk galaxies and the Faber-Jackson relation (Faber & Jackson 1976) for dispersion-supported elliptical galaxies.

The Tully-Fisher relation is a empirical scaling between a disk galaxy's rotation velocity and its stellar mass. The relation is extremely tight for massive ($> 10^{9.5}$M$_\odot$) disk galaxies in the local Universe (Verheijen, 2001; Bell & de Jong, 2001; Pizagno et al., 2005; Kassin et al., 2006; Courteau et al., 2007; Masters et al., 2008; Reyes et al., 2011). However, towards higher redshift and lower masses, not all star-forming galaxies fall on the Tully-Fisher relation (e.g., Kassin et al. 2007; Puech et al. 2010). These galaxies are neither purely rotationally-supported or purely dispersion-supported, instead containing a mix of both forms of dynamical support.

This finding motivated Weiner et al. (2006b) and Kassin et al. (2007) to introduce a new kinematic parameter $S_{0.5} = \sqrt{0.5V_{rot}^2 + \sigma_g^2}$. This quantity accounts for both forms of internal motions, disordered (σ_g) and ordered (V$_{rot}$), and is a better tracer of the total gravitational potential (Weiner et al., 2006b; Covington et al., 2010). The quantity is independent of galaxy morphology or kinematic state — galaxies that fall to low rotation velocity from the standard Tully-Fisher relation are re-established on a tight $S_{0.5}$-M$_*$ relation (Kassin et al., 2007). This revised Tully-Fisher relation is coincident with the local Faber-Jackson relation for dispersion-supported galaxies (Kassin et al., 2007). A relatively tight $S_{0.5}$-M$_*$ relation has now been detected out to $z = 2$ (e.g. Cresci et al. 2009; Price et al. 2016).

1.4 Evolution of Galaxy Kinematics Over Cosmic Time

The past decade has seen major observational advances in our understanding of the evolution of galaxy kinematics over $0 \lesssim z \lesssim 3$.

Since $z = 1$, star-forming galaxies evolve significantly, increasing in rotational support and declining in dispersion support with time (Kassin et al., 2012). These trends, dubbed "disk settling", are also a function of mass, with massive galaxies being the most evolved at any time (dubbed "kinematic downsizing"; Kassin et al. 2012). This finding is corroborated in the evolution of the stellar morphology of galaxies — from $z = 1$ to now, morphologically-regular stellar disks become increasingly common towards lower redshift and higher mass (e.g., Mortlock et al. 2013; van der Wel et al. 2014b; Huertas-Company et al. 2016).

Whether or not the disk settling trends extend to higher redshifts and earlier times (namely $z = 2$) remains an open question.

The cosmic star-formation rate peaks at $z = 2$ (Madau & Dickinson, 2014) — that is 3 Gyrs after the Big Bang or, equivalently, 10 Gyr before the present day. This marks an incredibly active period of galaxy assembly. Compared to galaxies today at the same mass, typical galaxies at $z = 2$ are $\sim\times4$ times more gas-rich with $\sim\times10$ higher molecular gas surface mass densities (Tacconi et al., 2013). They form stars $\sim\times10$ faster (Whitaker et al., 2012), accrete mass at rates $\sim\times100$ higher (Scoville

et al., 2017), and experience mergers with other galaxies $\sim\times 5-10$ more frequently (Rodriguez-Gomez et al., 2015). In the short period spanning $1 < z < 3$, star-forming galaxies typically quadruple in stellar mass (Muzzin et al., 2013) and double in size (van der Wel et al., 2014a).

The processes that regulate this abrupt mass and structural growth (Somerville & Davé, 2015), i.e., stellar feedback, merging, outflows + inflows, also tend to be dynamically disruptive, as discussed above. This motivates the intense ongoing efforts, including in this thesis, to measure the kinematics of the galaxies at this epoch. They should be directly tied to these regulatory processes.

Until recently, detailed observations of galaxy kinematics at higher redshifts have lagged behind due to the increased difficulty of observing from the ground in the near infrared (near-IR), where the strong optical lines fall. With the advent of sensitive near-IR detectors and the development of a new generation of near-IR multi-object spectrographs — in particular, KMOS (Sharples et al., 2004) on the VLT and MOSFIRE (McLean et al., 2012) on Keck — we are beginning to probe this important epoch with great numbers (e.g., Genzel et al. 2006; Förster Schreiber et al. 2006; Law et al. 2007; Kassin et al. 2007; Wright et al. 2007; Genzel et al. 2008; Shapiro et al. 2008; Law et al. 2009; Förster Schreiber et al. 2009; Lemoine-Busserolle & Lamareille 2010; Jones et al. 2010; Gnerucci et al. 2011; Swinbank et al. 2012; Law et al. 2012; Kassin et al. 2012; Contini et al. 2012; Newman et al. 2013b; Glazebrook 2013; Wisnioski et al. 2015; Mieda et al. 2016; Price et al. 2016; Olivares et al. 2016; Simons

et al. 2016; Contini et al. 2016; Stott et al. 2016; Mason et al. 2017; Straatman et al. 2017; Turner et al. 2017b; Übler et al. 2017).

Contesting conclusions were reached in the literature prior to this thesis. There seemed to be general agreement that high redshift galaxies have higher velocity dispersions ($\sim$50-60 km s^{-1}; Förster Schreiber et al. 2009) compared to local galaxies ($\sim$25-30 km/s; Epinat et al. 2010). In the most massive galaxies, kpc-scale star-forming clumps can reach velocity dispersions $\sim$100 km/s (Genzel et al., 2011). The picture of disk settling at lower redshifts (Kassin et al., 2012) supports the argument that higher mass systems are more kinematically settled (ordered rotation dominates dispersion terms) than lower mass galaxies. It is unclear if the same holds true at higher redshifts. Estimates for the fraction of disk galaxies at high redshift is highly disparate between studies, ranging anywhere between $20\% - 100\%$. The largest resolved kinematic surveys at redshifts $z > 1$, e.g., (SINS (Förster Schreiber et al., 2009) and KMOS-3D (Wisnioski et al., 2015)), have argued that disks are common, while others (e.g., Erb et al. 2006; Law et al. 2009) found little to no evidence of rotational-support.

These differences are, at least partly, due to biases introduced between different methods and differences in sample selection. Both of the current observational approaches in the literature, single slit spectroscopy and integral field spectroscopy (IFS), suffer from a number of limitations. Major uncertainties arise with single slit spectroscopy since these observations are limited to only one spatial dimension of

information. Information regarding kinematic gradients perpendicular to the slit axis are lost. To measure rotation in a system, one must know the kinematic axis a priori. While the photometric axis may provide reasonable constraints on the kinematic axis for disk galaxies, morphologically disturbed systems often exhibit high misalignment between the photometric and kinematic major axis (Förster Schreiber et al., 2009).

While IFS provides a better alternative for resolving detailed kinematic information, it comes at the cost of sensitivity. Recent IFS surveys (e.g., Wisnioski et al. 2015) have improved on sampling typical star-forming galaxies at $z = 2$ (i.e., galaxies that lie on the star-formation main sequence), but they are generally limited to the more massive systems ($\log M_*/M_\odot > 10$). Kinematic data for low stellar mass ($\log M_*/M_\odot < 10$) galaxies — those galaxies we expect to be the ancestors of MW-mass galaxies today — is only available for a handful of systems, with the highest-quality data coming from rare lensed systems (e.g., Jones et al. 2010).

Important questions remain on the buildup and evolution of present day galaxies: what is the kinematic state of the general population of star-forming galaxies at high redshifts? Is there a transition at low stellar mass from ordered to disordered galaxies at higher redshift (as is found at lower redshift)?

1.5 This Thesis

This thesis tackles the following question: *when do galaxies first assemble their disks?* We take advantage of premiere observing facilities, both on the ground and in space, and state-of-the-art galaxy formation simulations.

In Chapter 2, we examine the Tully-Fisher relation at $z \sim 0.2$ and its dependance on galaxy morphology. In Chapter 3, we adopt a novel observing strategy and perform a Keck/MOSFIRE kinematics survey of star-forming galaxies at $z \sim 2$. In Chapter 4, we link star-forming galaxy populations over $0.1 < z < 2.5$ and examine the kinematic evolution of galaxies over the past 10 Gyr. In Chapter 5, we analyze mock observations from a suite of hydrodynamical simulations of galaxy formation and test and quantify biases in interpreting modern observations. We summarize our conclusions in Chapter 6.

Chapter 2

A Transition Mass in the Local Tully-Fisher Relation

In this chapter, we study the stellar mass Tully-Fisher relation (TFR; stellar mass versus rotation velocity) for a morphologically blind selection of emission line galaxies in the field at redshifts $0.1 < z < 0.375$. Kinematics (σ_g, V_{rot}) are measured from emission lines in Keck/DEIMOS spectra and quantitative morphology is measured from V- and I-band Hubble images. We find a transition stellar mass in the TFR, $\log M_* = 9.5\ M_\odot$. Above this mass, nearly all galaxies are rotation-dominated, on average more morphologically disk-like according to quantitative morphology, and lie on a relatively tight TFR. Below this mass, the TFR has significant scatter to low rotation velocity and galaxies can either be rotation-dominated disks on the TFR or asymmetric or compact galaxies which scatter off. We refer to this transition mass

as the "mass of disk formation", M_{df} because above it all star-forming galaxies form disks (except for a small number of major mergers and highly star-forming systems), whereas below it a galaxy may or may not form a disk.

2.1 Introduction

The Tully-Fisher relation (TFR; Tully & Fisher 1977) is an empirical scaling between the luminosity of a disk galaxy and its rotation velocity. Later work replaced luminosity with the more physical quantity stellar mass, M_*. In the local Universe, the TFR is remarkably tight (Verheijen, 2001; Bell & de Jong, 2001; Pizagno et al., 2005; Kassin et al., 2006; Courteau et al., 2007; Masters et al., 2008; Reyes et al., 2011) and its parameterization serves as an important constraint for models of disk galaxy formation (e.g. Mo et al. 1998; Somerville & Primack 1999; Navarro & Steinmetz 2000; Dutton et al. 2007).

Although the TFR is well behaved for ordered disk galaxies, morphologically disturbed or compact galaxies tend to fall below the local relation, exhibiting low rotation velocity for a given stellar mass (Kassin et al., 2007, 2012). Ordered velocity fields may be disturbed in major merging events or tidal disruptions (Rampazzo et al., 2005; Kronberger et al., 2007; Covington et al., 2010; De Rossi et al., 2012), through the accretion of non-ordered external angular momentum from cold flows (Brooks et al., 2009; Elmegreen & Burkert, 2010) and/or disruptive feedback (Mac Low & Ferrara,

1999; Lehnert et al., 2009).

Weiner et al. (2006b) and Kassin et al. (2007) demonstrated that accounting for both the disordered motions (σ_g) and ordered rotation velocity (V_{rot}) in a new kinematic quantity, $S_{0.5} = \sqrt{0.5V_{rot}^2 + \sigma_g^2}$, re-establishes a tighter $S_{0.5}$-M_* scaling relation. This relation is independent of galaxy morphology and coincident with the Faber-Jackson relation for early type galaxies. Numerical simulations have shown that $S_{0.5}$ traces the overall potential well of galaxy-dark halo systems, even for galaxies undergoing drastic kinematic events, such as a major merger (Covington et al., 2010). The measurement of a disordered velocity component has been incorporated more in recent years (e.g. Förster Schreiber et al. 2009; Puech et al. 2010; Lemoine-Busserolle & Lamareille 2010; Catinella et al. 2012; Vergani et al. 2012; Cortese et al. 2014; Wisnioski et al. 2015).

With further investigation, Kassin et al. (2012) demonstrated that since $z \sim 1$ star-forming galaxies have been kinematically settling from systems with a dominant dispersion component to rotationally supported disks. Such galaxies follow kinematic downsizing: more massive galaxies exhibit the most ordered kinematics (high V_{rot}/σ_g) at all epochs. While high and intermediate mass galaxies are likely settling to disks, it is unclear whether low mass galaxies follow the same evolutionary path.

It is well known locally that morphological type is a strong function of stellar mass, with dwarf systems exhibiting more irregular morphology, distinct from their large disk counterparts (e.g. Roberts & Haynes 1994; Bothwell et al. 2009; Mahajan et al.

2015). Moreover, there is mounting evidence that disturbed galaxies are increasingly more common at low masses in the early Universe (Mortlock et al., 2013).

However, kinematic surveys often select against galaxies with disturbed morphologies with regards to other interests, e.g. performing distance measurements or studying dark matter (e.g. Bershady et al. 2010). In the local Universe, dwarf galaxies can show rotational signatures in both their HI and stellar components (e.g. Swaters et al. 2002, 2009; McConnachie 2012). When the morphological selection is opened to include irregular galaxies, compact galaxies, and close pairs, the presence of features such as peculiar velocity fields and thick disks are found. Indeed, complex kinematics and low rotational support is frequently found for both low luminosity (e.g. Barton et al. 2001; Kannappan et al. 2002; Young et al. 2003; Vaduvescu et al. 2005; Kirby et al. 2014; Cortese et al. 2014) and highly star-forming dwarfs (e.g. van Zee et al. 1998; Cannon et al. 2004; Lelli et al. 2014). However, locally, limited studies have been performed placing large samples of these disordered systems on the TFR, or relating the relative contributions of V and σ to the morphology of the galaxy.

In this chapter we study the resolved kinematics for a morphologically unbiased sample of star-forming galaxies at z $\sim$ 0.2. Compared to nearby samples, a survey at z $\sim$ 0.2 benefits from the smaller angular sizes of galaxies and the higher target density. Large homogenous samples can be efficiently obtained with a multi-object spectrograph. This sample is unique from other local samples in that we include galaxies with both disturbed and disk-like morphologies. Furthermore, we incorporate

measurements of the non-negligible contributions from random motions as well as the rotation velocity.

In section 2, we discuss the sample selection, the method used for measuring kinematics from emission lines and the measurements of quantitative morphologies. In section 3, we present the main result of this chapter: a transition stellar mass in the TFR. In section 4, we illustrate the correlation between gas phase kinematics and galaxy morphology. In section 5, we compare our results with measurements of kinematics for low mass galaxies in the literature both locally and at intermediate redshift. Our conclusions are presented in section 6. In the Appendix, we test our ability to recover kinematics for the galaxies with the smallest angular extent in our sample. We adopt a ΛCDM cosmology defined with (h, Ω_m, Ω_Λ) = (0.7, 0.3, 0.7).

2.2 Data and Sample Selection

In this section we detail the sample selection and the measurements of the kinematics and morphological indices. We reference the Appendix for further analysis and discussion of the effects of seeing on our kinematic measurements.

We focus on the lowest redshift bin in the galaxy sample used by Kassin et al. (2007) and Kassin et al. (2012) (hereafter referred to as K07 and K12, respectively), namely $0.1 < z < 0.375$. At these redshifts, the K12 sample is sensitive to low mass dwarf galaxies. We briefly review how this sample was selected and defer to K12 for

further details. The K12 sample is drawn from field 1 of the DEEP2 Redshift Survey (Newman et al., 2013a). DEEP2 employed the DEIMOS multi-object spectrograph (Faber et al., 2003) on the Keck-II telescope. The 1200 line/mm grating was used and the slits were fixed at $1''$, leading to a spectral resolution of R $\sim$ 5000. The K12 sample was cut on nebular line strength ($> 10^{-17}$ erg s^{-1} cm ^{2}), available Hubble Space Telescope (HST) imaging and slit alignment from the photometric major axis ($\leq 40^{\circ}$).

We use HST imaging in two passbands with the Advanced Camera for Surveys (ACS), V (F606W) and I (F814W), from the AEGIS survey (Davis et al., 2007). Each of the images has a pixel scale of $0.03''$ and a typical FWHM PSF of $0.1''$ (0.33 kpc at z = 0.2). Inclinations are measured with the SExtractor software (Bertin & Arnouts, 1996) using the V-band HST image. The V-band traces the young stars and thus should not be very different from the nebular emission line morphology. A further cut is applied to the sample, limiting inclinations to $30^{\circ} < \mathrm{i} < 70^{\circ}$, to avoid uncertain inclination corrections for face-on galaxies and dust effects in edge on systems. However, a handful (4) of severely disturbed galaxies for which inclinations and PAs are uncertain are included. The exclusion of these galaxies does not alter our conclusions.

Stellar masses were derived using the rest frame B-V color and absolute B-band magnitude (Bell & de Jong, 2001; Bell et al., 2005) with refined empirical corrections from SED fitting (Bundy et al., 2006), as described in Lin et al. (2007). The adopted

IMF is from Chabrier (2003). Errors on stellar masses are approximately 0.2 dex.

Spectral slits must be aligned to within 40° of a galaxy's major axis to reliably recover rotation (Weiner et al. 2006a). K07 removed galaxies with slits misaligned by more than 40° from the HST derived photometric major axis, except for the 4 galaxies with severely disturbed morphologies. Beyond this cut there are no residual correlations between measured kinematics (rotation or dispersion) and slit alignment in our sample. The scale of the atmospheric turbulence sets a limiting angular size for measuring rotation velocity in a galaxy. The seeing tends to smooth and eliminate small scale rotation gradients. We test the limiting resolving power imposed by beam smearing in the Appendix. For the observational conditions of DEEP2 and for the lowest S/N in our sample, kinematics can be measured for galaxies to diameters encompassing 95% of the light (D_{95}) of (0.87±0.06) × seeing. We make a further cut on the K07 sample and remove 12 galaxies which are not extended enough to confidently measure kinematics.

Our final sample contains 119 galaxies and uniformly covers the "blue cloud" (Figure 1 in K12). The qualifying feature of our selection is that, aside from the inclination cut, there was no explicit selection on morphology. Contrary to previous TFR studies, this sample selection includes disturbed and compact galaxies. This allows us to more fully sample the population of emission line galaxies.

2.2.1 Kinematics

We adopt kinematics measured from bright nebular emission lines (Hα λ6563 or [OIII] λ5007) in K07. The rotation velocity, uncorrected for inclination, and spatially resolved gas dispersion, σ_g, were measured with the program ROTCURVE (Weiner et al., 2006a), taking into account the effects of seeing. The seeing was measured through alignment stars on each slit mask (see Newman et al. 2013a). For our sample, the seeing varied between 0.55″ and 1.2″ FWHM, with a median value of 0.75″ (1.36 kpc at z = 0.1, 3.84 kpc at z = 0.375).

The kinematic measurements have been described in previous papers, so we will briefly review them here and refer to Weiner et al. (2006a) for the details. In short, ROTCURVE builds model arctan rotation curves where V is the velocity on the flat part of the rotation curve ($V_{rot} \times \sin(i)$), with an additional dispersion term (σ_g), which is constant with radius. Due to the seeing, the rise of the rotation curve is not well resolved and the turnover radius for the rotation curve (r_t) is not well constrained. The turnover radius is kept fixed to a value of 0.2″. The recovered rotation velocity and turnover radius are only slightly covariant, with a marginal ± 0.1 dex change in V for a ±0.1″ change in r_t. Models with varying V and σ_g are blurred with the seeing and fit to the data. V and σ_g are explored with a grid spacing of 5 km s^{-1} and the best fit value is determined through a χ^2 minimization on this grid.

The spectral resolution of the 1200 line/mm grating used by the DEEP2 survey allows measurements for $V_{rot} \times \sin(i)$ down to $\sim$ 5 km s^{-1} and σ_g to $\sim$ 15 km s^{-1}.

Measurements with best fits below these limitations are set to these values as upper limits. This is the case for 7 galaxies for V_{rot} and 22 galaxies for σ_g. Example kinematic fits and the corresponding χ^2 spaces are shown later in this chapter in Figure 2.4.

HST imaging is used to measure inclinations in order to correct the measured rotation velocity. As mentioned previously, corrections were not applied to four galaxies with severely disturbed morphologies where the inclination was highly uncertain. They are marked with carets in Figure 3.5.

We note that the quantity σ_g is *not* like the typical pressure supported velocity dispersion measured from stellar absorption lines in early-type galaxies. Since σ_g is tracing hot gas which can radiate, a high dispersion system can not remain in equilibrium after a crossing time. Therefore σ_g is effectively measuring velocity gradients below the seeing limit, as illustrated by the simulations of Covington et al. 2010. The typical thermal broadening for T $\sim 10^4$ K Hydrogen gas is 10 $\mathrm{km\,s^{-1}}$, so a measure of $\sigma_g > 25$ $\mathrm{km\,s^{-1}}$ is tracing the relative motions of HII regions and/or disordered motions associated with unresolved velocity gradients (Weiner et al. 2006a, K12).

2.2.2 Quantitative Morphology

High resolution HST-ACS images allow us to quantify morphologies for each galaxy. In particular, we examine three indices: the Gini coefficient, asymmetry, and concentration. We find little difference between the indices for the V- and I-

band and so we simply adopt the I-band measurements (approximately rest V-band at z=0.2) for our analysis. We describe these parameters now and examine how they correlate with kinematics in section 4.

The Gini coefficient was adopted from economic theory. As applied to the study of galaxy morphology, the Gini coefficient provides a non-parametric measurement of the distribution of light among the pixels associated with a galaxy (Abraham et al., 2003; Lotz et al., 2004). The Gini coefficient approaches unity for systems with a large fraction of intensity confined to only a few pixels and approaches zero for a uniform intensity distribution. It compliments the more standard concentration index (Abraham et al., 1994), as both trace intensity clustering, but the Gini coefficient is insensitive to the location of the clustering. The typical uncertainty on the Gini coefficient is 0.02, as determined from empirical comparisons of deep (UDF) and shallow fields (GOODS) (Lotz et al., 2006).

The concentration index (defined in e.g. Abraham et al. 1994 and Simard et al. 2002) measures the ratio of flux contained in two isophotes. The outer isophote is defined by the 2σ background contour with a normalized radius of 1 and the inner isophote is defined by a normalized radii of α. Concentration, asymmetry, and size were measured with the GIM2D software (Simard et al., 2002), which simultaneously fit to both the V- and I-band images. The concentration index is measured for $\alpha = (0.1, 0.2, 0.3, 0.4)$. We find no significant differences in trends between alpha levels and adopt $\alpha = 0.1$ for our analysis.

The asymmetry index in GIM2D is as defined in Abraham et al. (1994, 1996). Asymmetry is measured by first assigning contiguous pixels to the galaxy, rotating the image by 180° and then self-subtracting the mirrored image from the original image.

The error bars we use in the figures below for asymmetry and concentration represent the typical 1σ scatter between the four GIM2D measurements for each individual V-Band image. These do not represent the additional uncertainty from the image S/N (limiting magnitude $\sim$ 28.7 AB), for which comparisons with deeper fields are needed. Shallower studies than ours (limiting magnitude $\sim$ 26.5 AB; e.g. Peth et al. 2016) find relative uncertainties in Concentration and Asymmetry of $\sim$ 0.05 with respect to deeper data (limiting magnitude $\sim$ 27.4 AB).

2.3 A Transition Mass in the TFR, the Mass of Disk Formation (M_{df})

In the top panel of Figure 3.5 we show the stellar mass TFR for our sample. There is a noticeable transition at a stellar mass of $\log M_*/M_\odot \cong 9.5$. Above this mass, all galaxies in our sample are on the local TFR. Below this mass, galaxies may or may not lie on the local TFR, with the galaxies falling off tending to display systematically high measurements of σ_g. We posit that $\log M_*/M_\odot \cong 9.5$ marks an important stellar mass associated with the stabilization and formation of a disk. We will refer to this

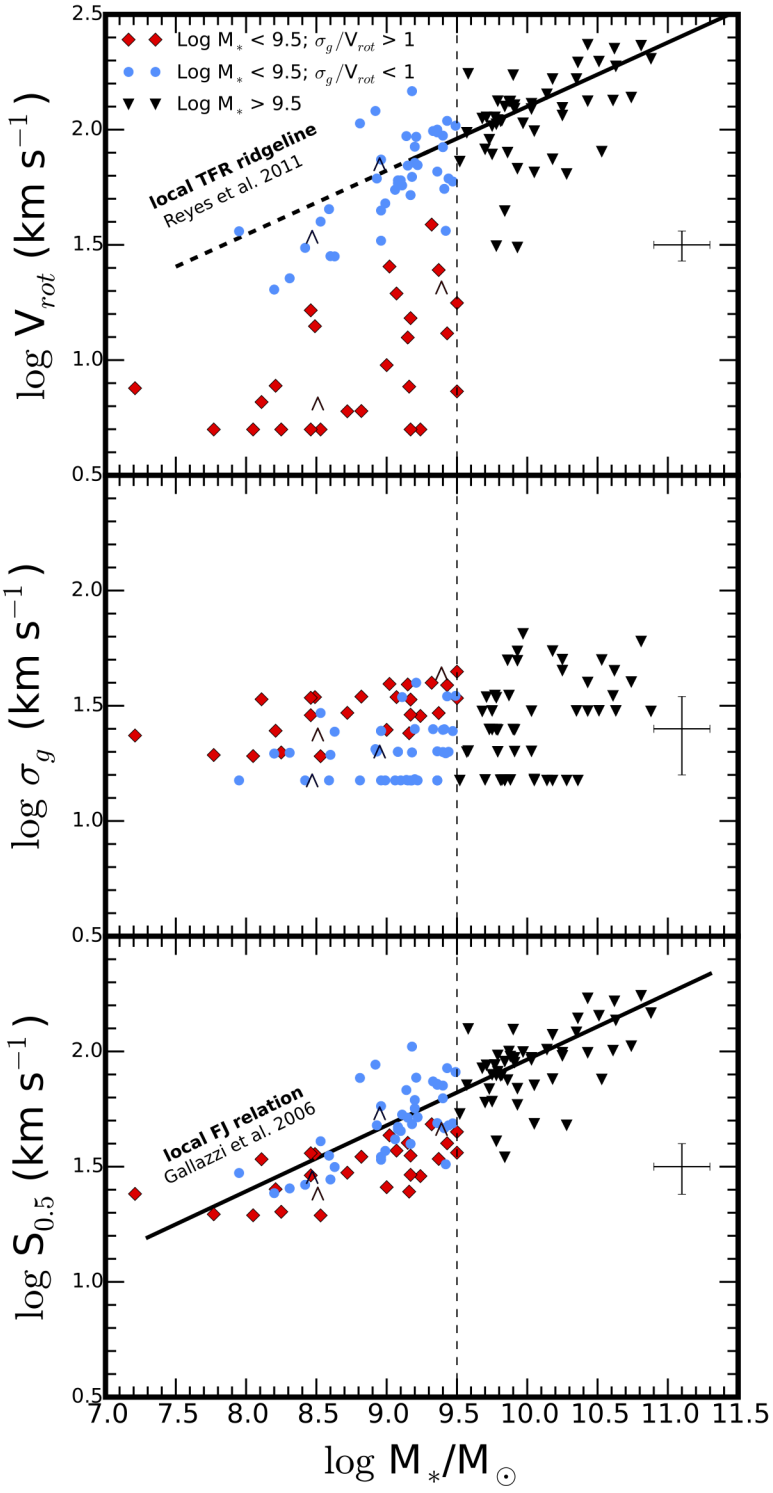

Figure 2.1: Caption on next page.

Figure 2.1: The stellar mass Tully-Fisher relation for the K07/K12 sample of galaxies at $0.1 < z < 0.375$ is shown. Below a stellar mass of $\log M_*/M_\odot \cong 9.5$, there is significant scatter to low V_{rot} (red points). The local TFR (Reyes et al., 2011) (black line), adjusted for a Chabrier (2003) IMF, and its extrapolation to lower stellar masses (dashed line) is shown. b) For the same galaxies the integrated gas velocity dispersion, a measure of disordered motions, is shown versus stellar mass. c) Accounting for both ordered and disordered motions in the $S_{0.5}$-M_* relation results in a relatively tight scaling, coincident with the local Faber-Jackson relation from Gallazzi et al. (2006). Galaxies are color/shape coded according to whether they are on the TF ridgeline and whether they have high or low stellar mass. This coding is repeated in other plots in the chapter. The rotation velocities for the four galaxies with carats are not inclination corrected due to their highly uncertain inclination.

mass as "the mass of disk formation", M_{df}.

In Figure 3.5 we separate our sample into 3 bins, motivated by their location on the TFR. We define these populations as high mass ($\log M_*/M_\odot > 9.5$) disks (on the TFR; black triangles), low mass ($\log M_*/M_\odot < 9.5$) ordered ($\sigma_g/V_{rot} < 1$) disks (on the TFR; blue circles), and low mass ($\log M_*/M_\odot < 9.5$) disordered ($\sigma_g/V_{rot} > 1$) systems (scattering to low V_{rot} from the TFR; red diamonds). This notation will be continued for successive plots.

We compare the slope in the TFR, $\log V_{rot} \propto \alpha \log M_*$, with a local sample ($z < 0.1$) of 189 disk galaxies from SDSS (Reyes et al., 2011), who find a value of $\alpha = 0.278 \pm 0.13$ over a mass range $9.0 < \log M_*/M_\odot < 11.0$. We refer to this relation

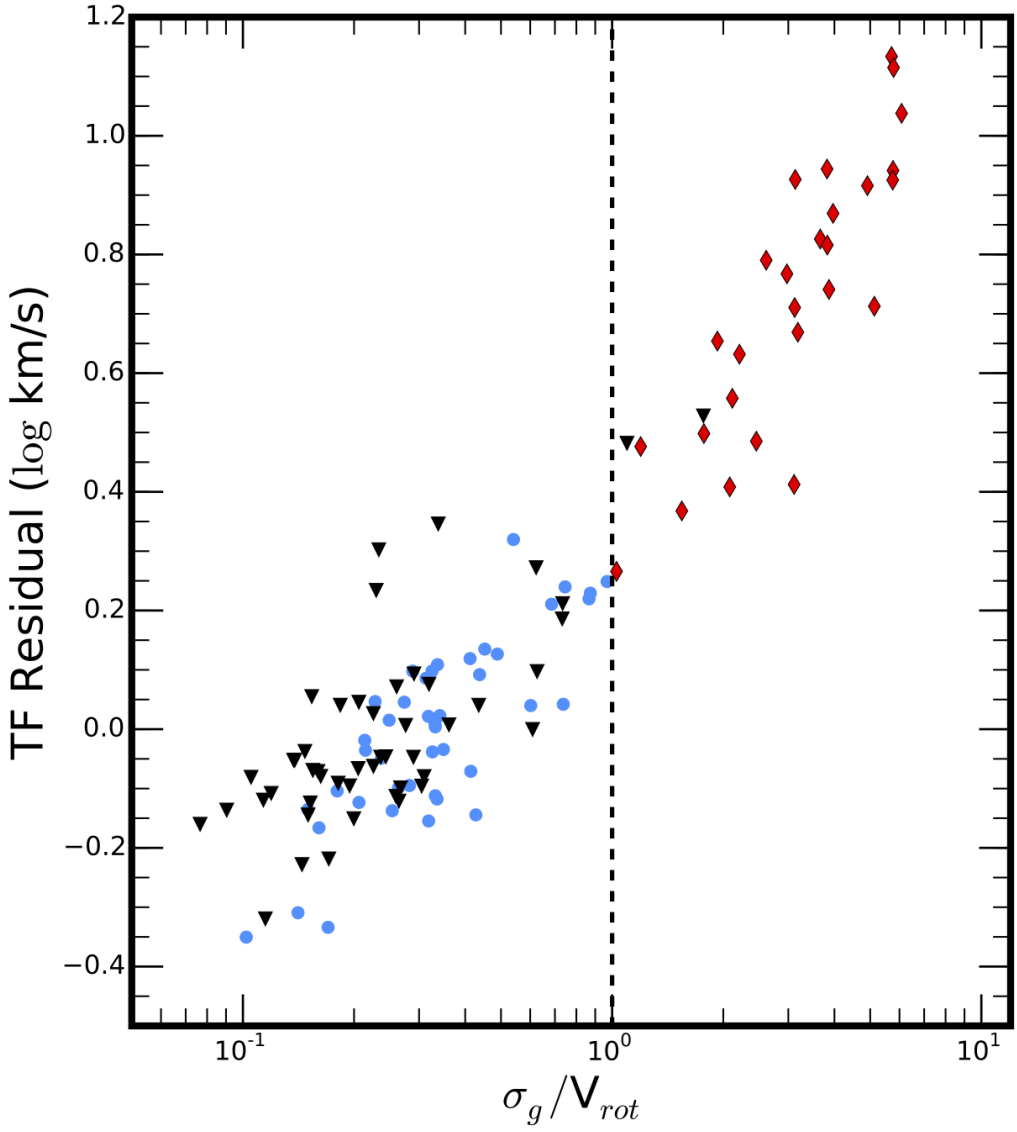

Figure 2.2: The residual from the local Tully-Fisher ridge line (Reyes et al., 2011) is plotted versus the ratio of disordered to ordered motions (σ_g/V_{rot}). As expected from K07 and K12, these quantities trace each other well. We use σ_g/V_{rot} to quantify the location of a galaxy on the TFR in the remainder of this paper.

as the TF "ridgeline" and mark it and its extrapolation to lower stellar masses in our TF plots. The high and low mass disks in our sample are well fit by the local ridgeline.

In the middle panel of Figure 3.5 we plot M_* versus σ_g. As mentioned previously, σ_g integrates unresolved velocity gradients in our systems, probing disordered components to the velocity field. The subset of galaxies that fall short of the Tully-Fisher ridgeline (red points) exhibit higher integrated velocity dispersions than the galaxies on the ridgeline at similar stellar mass.

As shown in K07 and K12, combining both the velocity dispersion and rotation velocity into a new kinematic parameter, $S_K = \sqrt{KV_{rot}^2 + \sigma_g^2}$, establishes a relatively tight relation. In the bottom panel of Figure 3.5 we plot S_K versus M_* for K=0.5. The choice of K=0.5 is motivated by virial arguments for a spherically symmetric tracer distribution (see Weiner et al. 2006a). Combining both the velocity dispersion and rotation velocity into $S_{0.5}$ re-establishes a tight analogue to the TFR, independent of morphology and coincident with the Faber-Jackson relation (K07, K12).

As expected, for galaxies in our sample, the residual from the local TF ridgeline is a strong function of σ_g/V_{rot}. In Figure 2.2 we demonstrate this correlation, demarcating the region where ordered disk galaxies fall (i.e. those on the TFR) would fall. We will use σ_g/V_{rot} as a proxy for the location of a galaxy on the TFR plot (Figure 3.5, top).

2.4 Morphology and Gas Kinematics

In Figure 2.3 we reproduce the TFR in Figure 3.5, but replace the data points with HST V + I-band color images. Upon visual inspection we note distinct morphological characteristics among the regions of this plot identified in Figure 3.5. The galaxies with stellar masses higher than log $M_*/M_\odot \cong 9.5$ exhibit extended disk-like morphologies. Galaxies with stellar masses log $M_*/M_\odot < 9.5$ that are rotation dominated ($\sigma_g/V_{rot} < 1$) also show disk morphology, although they are less extended than the higher mass systems. Galaxies that fall below the TF ridgeline have dispersion dominated kinematics ($\sigma_g/V_{rot} > 1$) and show irregular or compact morphologies.

In Figure 2.4, we show two representative galaxies from each of the three defined regions in Figure 3.5 (from left to right): (1) low mass dispersion dominated galaxies which have compact morphology and irregular asymmetric features, (2) low mass rotationally supported galaxies which have characteristic morphologies of disks: they are more or less symmetric and elongated, and (3) high mass ordered galaxies which have similar disk-like morphologies.

These trends were noted by visual inspection in previous work (K07). We will now demonstrate that gas phase kinematics are related to quantitative galaxy morphology by comparing σ_g/V_{rot} (ratio of disordered to ordered motions) to quantitative morphological indices (Gini coefficient, concentration, asymmetry). As described in the rest of this section, we find that the galaxies which fall on the Tully-Fisher ridgeline tend to exhibit low values of asymmetry, concentration, and Gini. In addition, they

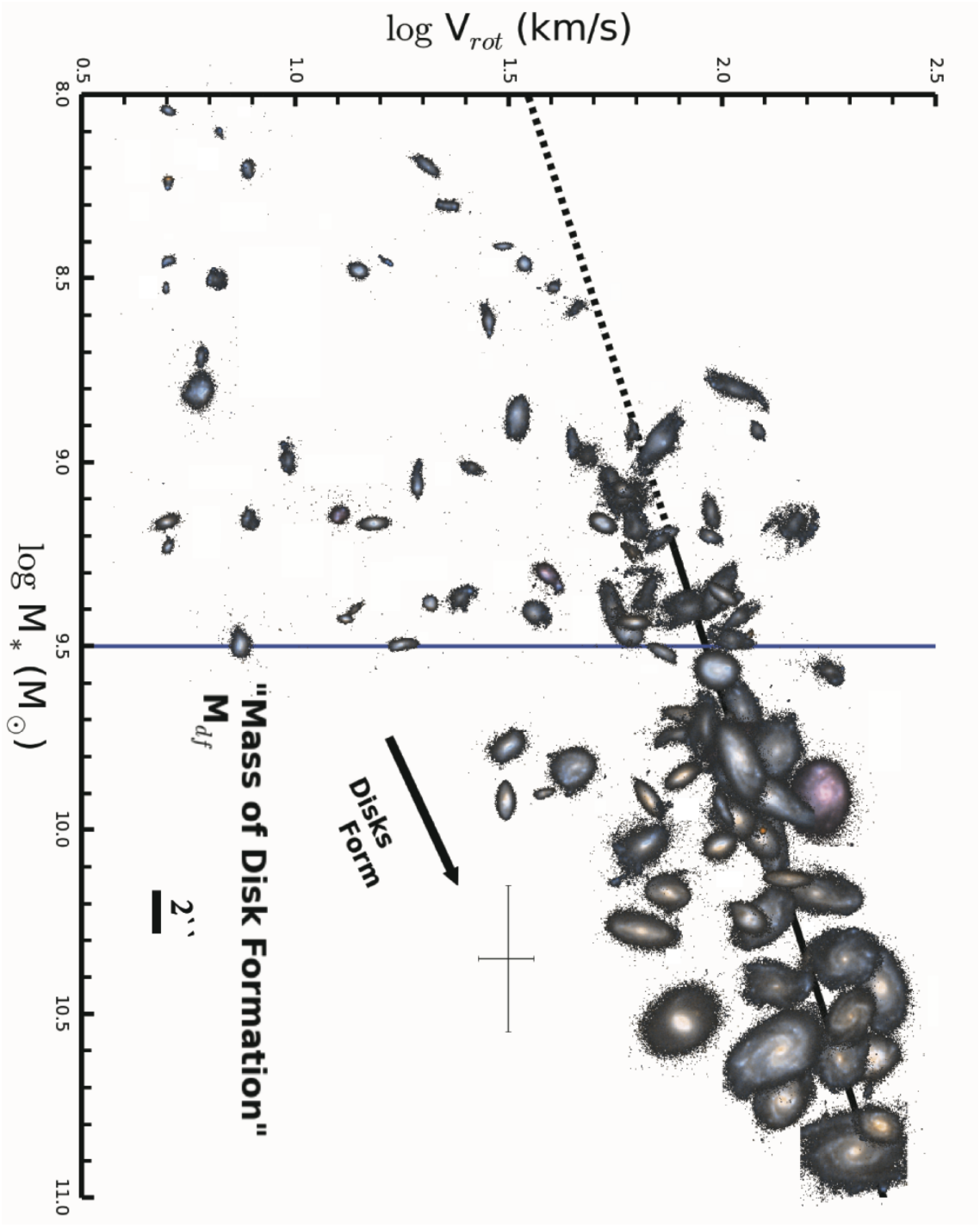

Figure 2.3: Caption on next page.

Figure 2.3: The Tully-Fisher relation for a morphologically unbiased sample of blue galaxies over $0.1 < z < 0.375$. V and I-band Hubble images are shown in place of points. A $2''$ size scale is included for reference. The local TFR from Reyes et al. (2011) is shown as a solid line and is extrapolated to lower masses with a dotted line. Galaxies with stellar masses log $M_* \gtrsim 9.5$ $M_\odot$ fall on the TFR and on average have disk-like morphologies. Below this mass, a galaxy may or may not have formed a disk. We therefore call this mass the "mass of disk formation" (M_{df}). Low mass galaxies which fall from the TFR appear less extended and more irregular than the counterpart galaxies on the TFR. To make the figure manageable, a surface brightness cut on the images was selected based on the higher mass galaxies. This cut leads to a few of the low mass galaxies appearing smaller on this image than their true extent.

tend to have larger sizes consistent with the disk size-mass relation. Kinematically ordered galaxies ($\sigma_g/V_{rot} < 1$) at both low and high mass are consistent with being drawn from identical parent distributions for these indices. Galaxies which are kinematically disordered ($\sigma_g/ V_{rot} > 1$) and fall from the TFR ridgeline tend to exhibit quantitative morphologies characteristic of disturbed or compact systems (high asymmetry, concentration and Gini) and are statistically distinct from the galaxies on the TF ridgeline. Below we detail these findings.

The top panel in Figure 2.5 shows the asymmetry index versus σ_g/V_{rot} for our galaxy sample. Low mass disordered galaxies (red diamonds) on average have a higher distribution in asymmetry than the galaxies with ordered kinematics which lie on the TF ridgeline (blue circles and black triangles). The asymmetry index is distributed

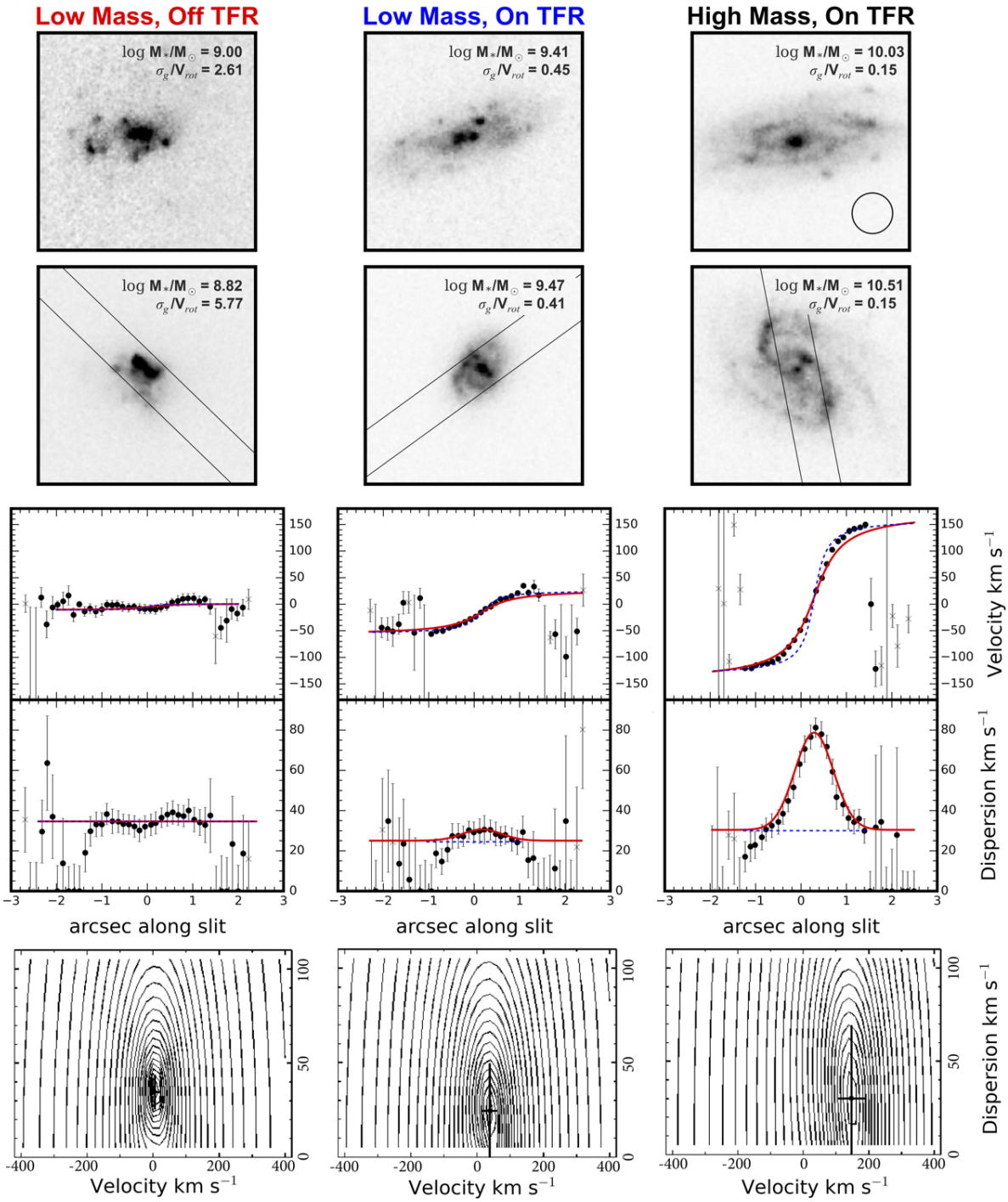

Figure 2.4: Caption on next page.

Figure 2.4: Upper Panels: HST V-band images of characteristic galaxies in the three regions of the TFR, Figure 3.5 (top). Individual images are 4″ on a side. Outer low surface brightness features are present but not apparent in the images of the low mass images due to the contrast settings chosen. The black circle represents a seeing of 0.75″. Top Left: Low mass galaxies which scatter to low V_{rot} from the TFR are shown. These exhibit compact emission with irregular asymmetric features. Top Middle: Low mass galaxies on the TFR are shown. They exhibit disk-like morphologies characterized by symmetric and elongated intensity distributions. Top Right: High mass ordered galaxies on the TFR are shown. They also exhibit more extended disk-like morphologies. Lower Panels: Example kinematic fits are shown for the three galaxies in the second row. Filled circles were used in the fitting routine, while the crosses were rejected. The blue dashed line is the intrinsic model and the red curve is the seeing blurred model which is fit to the data. For galaxies with rotation gradients, the seeing creates a classic artificial central peak in the velocity dispersion profile and slightly lowers the rotation velocity. Bottom Panels: χ^2 contours for the model parameters.

with an average and standard deviation 0.18 ± 0.06 for low mass disordered systems and 0.11 ± 0.06 and 0.11 ± 0.04 for the low and high mass ordered systems, respectively. We run a two-sample Kolmogorov-Smirnov (K-S) test to determine the probability that the three distributions in asymmetry are drawn from identical parent distributions. The p-value returned from the K-S test represents the probability that data drawn from identical parent distributions would be as disparate as observed. The K-S test between the low and high mass ordered populations yields a p value of

0.77, indicating a high probability of being drawn from identical parent distributions. However, the K-S tests between the low mass disordered galaxies and the high/low mass ordered distributions yield near zero probabilities of being identical ($p = 10^{-5}$ and 10^{-4}, for comparisons with high and low mass ordered samples, respectively.)

The second panel in Figure 2.5 shows the Gini coefficient versus σ_g/V_{rot}. The disordered low mass population of galaxies exhibits a trend towards higher values of Gini. Average values of Gini increase from $G = 0.48 \pm 0.04$ and 0.48 ± 0.09 for the low and high mass ordered systems, respectively, to $G = 0.52 \pm 0.04$ for the disordered low mass systems. The K-S test between the ordered populations yields a p value of 0.48, while the dispersion dominated systems are unique compared with either distribution of ordered galaxies ($p = 10^{-5}$). While statistically significant, the relative change in Gini is small, reflecting the fact that even disk galaxies exhibit a level of non-uniformity (i.e. spiral features and clumpy star-formation). In large heterogeneous samples of galaxies the range of the Gini coefficient is relatively small (e.g. Lotz et al. 2008; Peth et al. 2016), with a floor at a value of around 0.40 for the most uniform galaxies and a peak value of only 0.65. In relation to this small range, a change of 0.04 reflects a non-negligible difference in galaxy type.

The third panel of Figure 2.5 shows the concentration index versus σ_g/V_{rot}. Similar to the Gini coefficient, kinematically disordered systems typically display higher values of concentration. The concentration index increases from 0.51 ± 0.09 and 0.53 ± 0.07 for the low and high mass ordered systems, respectively, to 0.65 ± 0.12 for the

disordered low mass systems. The K-S test between the ordered populations yields a p value of only 0.02, due to the large scatter in the low mass ordered distribution. The p value between the low mass disordered distribution and the ordered distributions is once again near zero ($p = 10^{-5}$).

We now examine the correlation between size with disordered motions in our sample. We use the HST V-band half-light radius R_{50} as measured using GIM2D. The low mass dispersion dominated galaxies have a mean value of $R_{50}/\mathrm{kpc} = 1.8 \pm 1.2$ rms. The low and high mass ordered systems are close to a factor of 2 larger, 3.1 ± 1.5 and 4.5 ± 2.0 kpc, respectively. To account for the well known mass dependance on size, we examine residuals from the SDSS DR7 median fit to the disk mass-size relation (Equation 3 in Dutton et al. 2011). In the bottom panel of Figure 2.5 we plot the log residual from the size mass relation ($\log(R_{50}/R_{50,RM})$) versus σ_g/V_{rot}. The ordered galaxies in our sample are distributed around the relation with an average scatter of 0.22 dex, consistent with the intrinsic width of the relation. The residuals for the dispersion dominated systems are centered 0.15 dex below the relation, although there are a few outliers that lie on or above the relation. At a given mass, the dispersion dominated systems tend to be smaller than expected from the radius-mass relation.

In the concentration-asymmetry plane (Figure 2.6) these differences become more apparent, with both the low and high mass ordered galaxies occupying relatively narrow regions of low asymmetry and concentration. The dispersion dominated systems,

however, tend to exhibit markedly high scatter in this plane, tending towards higher values of both concentration and asymmetry.

In summary: The ordered systems in our sample display quantitative indices characteristic of disks: low asymmetry and low concentration. Kinematically disordered galaxies on the other hand exhibit concentrated emission with asymmetric features, statistically distinct from their ordered counterparts.

2.4.1 Comparison with Previous Studies

2.4.1.1 Local Universe

Large local studies of the TFR have primarily focused on massive disk galaxies with $\log M_*/M_\odot \gtrsim 9.5$ (e.g. Verheijen 2001; Pizagno et al. 2007; Courteau et al. 2007; Bershady et al. 2010; Reyes et al. 2011). We find that the majority of star-forming galaxies above this mass are morphologically disk-like and the TFR is well behaved. In fact, the only populations of dispersion dominated systems at high stellar masses in the local Universe are the relatively rare and interaction induced (U)LIRGs systems (e.g. Arribas et al. 2014) and merging galaxies (e.g. the HI Rogues Gallery of Hibbard et al. 2001).

The TFR for $\log M_*/M_\odot < 9.5$ is less well-studied, especially for a morphologically unbiased sample. Furthermore, velocity dispersion is not frequently measured. Integrated line widths are often used as a proxy for the rotation velocity, with corrections

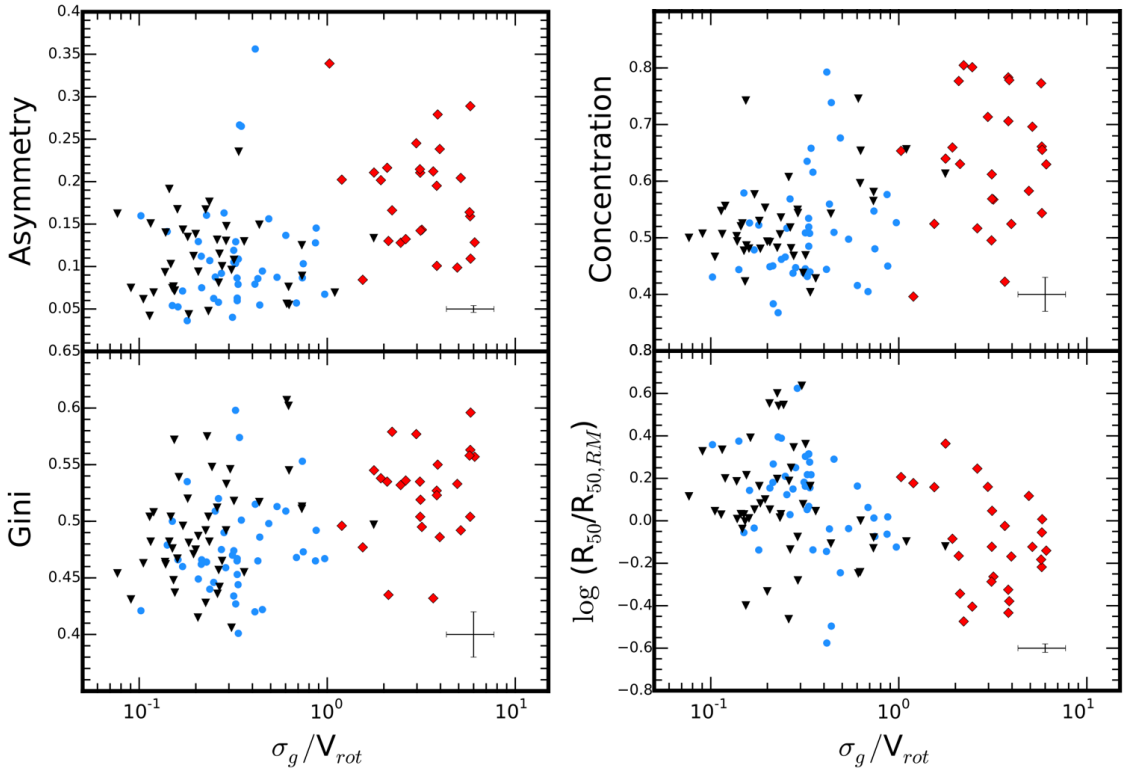

Figure 2.5: Quantitative morphological indices and V-band half-light radius (R_{50}) are shown as a function of kinematics for the galaxies in our sample. The bottom right panel shows the log residuals from the SDSS g+r derived disk mass-size relation (RM; Dutton et al. 2011). The quantity σ_g/V_{rot} measures the relative contributions from disordered motions and ordered rotation. Galaxies which scatter to low V_{rot} off of the TF ridgeline (red diamonds) are on average more asymmetric, have higher Gini and concentration values, and are smaller than galaxies on the TF ridgeline (blue circles for low mass and black triangles for high mass).

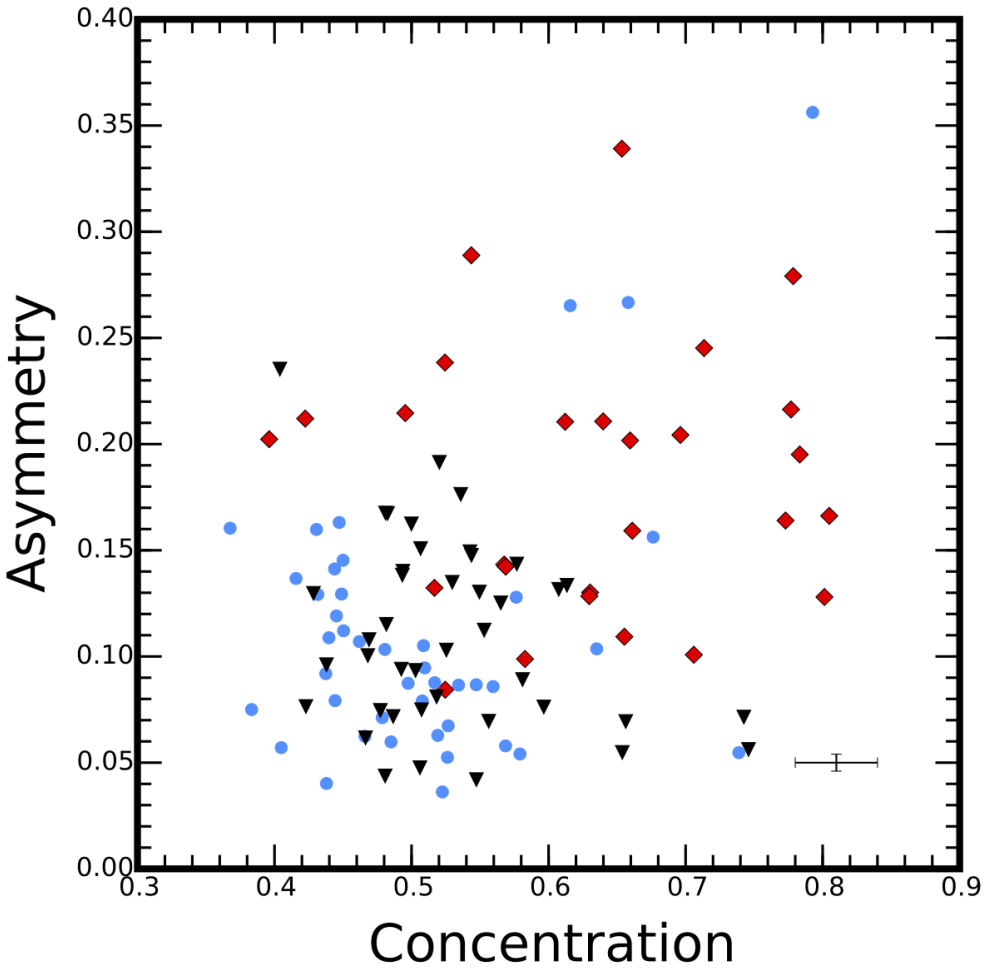

Figure 2.6: In the concentration-asymmetry plane, the high and low mass systems (black triangles and blue circles, respectively) are relatively localized to low asymmetry and concentration values. Low mass dispersion dominated galaxies (red diamonds) tend to scatter to larger values of both asymmetry and concentration.

assumed for anomalous contributions from random motions.

Most TFR studies of dwarf galaxies have focused on gas dominated systems ($M_g \geq M_*$). These galaxies typically show large residuals from the TFR to lower masses at a given rotation velocity, in the opposite direction to our sample. A tight baryonic Tully-Fisher relation is established once gas masses are included (McGaugh, 2005) and it has been well calibrated for a local sample of gas-dominated galaxies (e.g. Stark et al. 2009).

For local dwarf galaxies with both σ_g and V_{rot} measured, evidence for a luminosity dependence on V/σ_g has been long established (e.g. Mateo 1998). This trend is to be expected even for galaxies on the TFR, if we assume that σ_g is independent of mass and V_{rot} declines with mass. When available, though, resolved kinematics of irregular or compact dwarf systems typically show complex velocity fields which depart from a regularly rotating thin disk (e.g. Barton et al. 2001; Kannappan et al. 2002; Vaduvescu et al. 2005). For instance, the well studied SMC ($M_*/M_\odot \sim 10^{8.7}$) and LMC ($M_*/M_\odot \sim 10^9$) are both rotationally supported in their stellar and neutral gaseous components ($V/\sigma \sim 3$), while the kinematics of the smallest local dI systems, traced through neutral HI gas, typically showing no signs of rotation (e.g. Young et al. 2003).

Recent surveys of HI in the local volume have helped further characterize the dynamics of dwarfs, e.g. THINGS (Walter et al., 2008), FIGGS (Begum et al., 2008b), VLA-ANGST (Ott et al., 2012) and LITTLE THINGS (Hunter et al., 2012). These

surveys find mixed evidence among dwarf galaxies for both the existence of (i) rotationally supported disks (e.g. Begum et al. 2008a; Walter et al. 2008) and (ii) systems with thick disks or high/dominant contributions of dispersion (e.g. Roychowdhury et al. 2010; Ott et al. 2012).

The current data for resolved ionized gas kinematics in low mass galaxies is more limited. Interest in actively star-forming blue compact dwarfs (BCD) has led to measurements of velocity fields for a relatively large sample ($\sim$ 100) of these systems, usually in HI (e.g. van Zee et al. 1998, 2001; Thuan et al. 2004). Star-bursting systems, of which BCDs are a subset, make up close to 5% of the population of local dwarf galaxies (Lee et al., 2009). The origin of the compactness and late stage star-formation in the low mass (log $M_*/M_\odot \sim$ 7.0 - 9.6; Zhao et al. 2013) BCDs is up for debate. Recent HI investigations suggest high fractions of kinematically disturbed disks ($\sim$ 50%), although only a handful of systems fall short of the baryonic Tully-Fisher relation (Lelli et al., 2014). The ionized velocity fields are often found to exhibit high or dominant contributions from dispersion as well (e.g. Pérez-Gallego et al. 2011).

One of the largest surveys of resolved ionized gas kinematics in local galaxies is the GHASP survey (Gassendi Hα Survey of Spirals; Epinat et al. 2008, 2010). The GHASP survey selection was focused on galaxies with both spiral and irregular morphologies, although most of the more luminous galaxies display characteristic disk morphologies. The GHASP survey samples a wide range in stellar mass 9.0 $<$ log

$M_*/M_\odot < 11.7$ (Epinat et al., 2008). The TFR for a subset of galaxies is found to be relatively tight down to M_K = -18 or log M_*= 8.0 $M_\odot$ (Torres-Flores et al., 2011). While galaxies with large non-circular motions and corresponding rotation curve asymmetries show the largest scatter from the TF relation, to both low V_{rot} and low luminosity, the scatter is small compared to the dispersion dominated systems in our sample. Aside from a few outliers, no large break to low rotation velocity was found in the TFR for the GHASP sample. This may be due to a combination of both small sample sizes at masses log $M_*/M_\odot < 9.5$ (9 galaxies) and/or selection functions for rotating galaxies playing a role in constructing the stellar mass TFR. The σ/V for these 9 low mass galaxies ranges between 0.1 - 0.7 (i.e. all would be kinematically ordered in this chapter). On visual inspection of their optical morphologies in NED, we note that seven of these galaxies appear to have disk morphologies, with the presence of spiral arms in most cases. The low σ/V in these galaxies is consistent with the picture presented in this chapter, that disk morphologies indicate ordered kinematics. Two of the galaxies (UGC 5721, UGC 10757) do appear to have disturbed morphologies, so it is interesting to note that their σ/V is still less than 1 (0.16 and 0.35, respectively). The mean velocity dispersion for the GHASP sample is 25 $\pm$ 5 km s^{-1}, typical of local disks in general. This level of dispersion is expected for a combination of the thermal broadening from H atoms (T$\sim 10^4$ K; $\sim$ 10 km s^{-1}) and internal turbulence of HII regions ($\sim$ 20 km s^{-1}; Shields 1990). These measurements are comparable to the mean velocity dispersions for our ordered disks (21.0 $\pm$ 8.1

km s^{-1}) and slightly lower than our systems with more disturbed kinematics (34 $\pm$ 7.3 km s^{-1}). For the few compact rotators in GHASP we ran mock tests (see Appendix A for an example with galaxy UGC 528) to ensure that we could accurately recover their rotation if they were in our sample at z $\sim$ 0.2. The results of these tests indicate that if these galaxies were included in our sample we would recover their rotating disks.

Our understanding of the ionized kinematics of dwarf galaxies at low redshifts will substantially increase in the near future with ongoing and upcoming Integral Field Spectroscopy (IFS) surveys. The CALIFA (0.005 $<$ z $<$ 0.03, R $\sim$ 850-1650; N $\sim$ 600), SAMI (z $<$ 0.12, R $\sim$ 1700-4500; N $\sim$ 3400) and MaNGA (z $\sim$ 0.03; R $\sim$ 2000; N $\sim$ 10,000) surveys will provide velocity fields for large ensembles of local low mass galaxies. First results from CALIFA (García-Lorenzo et al., 2015) have reported that about half of the galaxies in their sample (8.5 $<$ log M$_*$/M$_\odot$ $<$ 11.5) have structure in their velocity fields which departs from a rotating disk. However, resolved velocity dispersions were not measured in this study and the coarse spectral resolution (R $\sim$ 1200) may not allow for measurements of the dispersion at the differences outlined in this chapter. First results from SAMI show a large fraction of both low and high mass local galaxies falling to low V_{rot} from the TFR (Cortese et al., 2014). The SAMI survey improves upon the GHASP sample with a large coverage of low mass systems, pushing down to stellar masses log M$_*$/M$_\odot$ $\sim$ 8. Below a stellar mass log M$_*$/M$_\odot$ $\cong$ 9, they find a precipitous trailing of galaxies from the well-defined 1 R$_e$ TF relation (Yegorova & Salucci, 2007). High spectral resolution in the red band (6300-7400 $\mathring{A}$, R

~ 4500) allow measurements of velocity dispersions. A tight scaling relation (M_*-S_K) is established once they account for the average measured velocity dispersion, similar to previous findings at high redshift (Weiner et al., 2006b; Kassin et al., 2007; Puech et al., 2010). The SDSS-III MaNGA survey will provide extensive additional coverage of this low mass regime, with a flat selection distribution down to a stellar mass of 10^9 $M_\odot$ and sampling out to at least 1.5 times the effective radius (R_e) (Bundy et al., 2015).

In summary, when studied in large numbers, local studies of the TFR have been biased towards massive disk galaxies and moreover will often not have the spectral resolution to resolve velocity dispersion. When resolved gas phase kinematics are available in low mass galaxies, complex velocity fields are often found in both neutral and ionized gas. The local TFR for dwarf galaxies will be expanded upon in the upcoming years, with surveys probing kinematics in ionized gas to low stellar masses in unprecedented numbers. Early results indicate an increase in complexity in the resolved 2D velocity fields of these low mass galaxies.

2.4.1.2 Low-Intermediate Redshift

Due primarily to sensitivity limits, there have been few studies of the kinematics in more distant ($z > 0.1$) dwarf galaxies. Furthermore, most studies do not measure resolved velocity dispersions and do not include irregular or compact galaxies.

Using deep 8 hour DEIMOS exposures, Miller et al. (2014) constructed the stellar

mass TFR for half of their sample (N = 41) of dwarf galaxies ($7 < \log M_*/M_\odot < 9$) out to z = 1, demonstrating that at least a fraction of dwarf galaxies are settled into rotationally supported systems at intermediate redshift. The remaining galaxies were either missing emission or were too small to reliably resolve rotation.

Recently, interest in dispersion dominated galaxies at high redshift (e.g. Law et al. 2009; Förster Schreiber et al. 2009) has motivated searches for high dispersion low redshift analogs. These studies typically select highly star-forming systems and find complex kinematics with low V/σ_g compared to local disk galaxies (e.g. Gonçalves et al. 2010; Amorín et al. 2012; Green et al. 2014).

Compact Lyman Break analogues (LBA) are an example of such a selection. LBAs are highly star-forming galaxies at z $\sim$ 0.2, selected from their high GALEX NUV luminosity (Heckman et al., 2005). Although these systems have slightly higher stellar masses $9.5 \leq M_*/M_\odot \leq 10.7$ than the break in our sample, they exhibit morphologies and kinematics which are similar to some of our more compact dwarf galaxies. Gonçalves et al. (2010) report on AO-assisted IFS observations of 19 compact LBAs at z $\sim$ 0.2 with stellar masses near our transition mass, $9.1 < \log M_*/M_\odot < 10.7$. They find a very high contribution of disordered motion in these rare systems (σ_g $\sim$ 70 km s^{-1}) and evidence that disk-like structure is more common in high mass LBAs. Similarly, Green et al. (2014) measured Hα kinematics for 67 extremely star-forming systems down to a stellar mass of 10^9 $M_\odot$ and found that one fifth of their sample shows no signs of rotation. The rotating disk galaxies in their sample fall on

the TFR while still exhibiting values of V/σ_g lower than local disks, comparable to dynamically hot high redshift galaxies. The dispersion dominated galaxies $V/\sigma_g \leq 1$ in both the intermediate redshift IFS samples have typical stellar masses above our observed mass of disk formation ($\log M_{df}/M_\odot \sim 9.5$). Although the unique selections (e.g. high star-formation, high surface mass density) for these samples are not necessarily representative, they do demonstrate the important contribution of σ_g to the kinematics in active systems.

At high redshifts ($1.5 < z < 3$), complex velocity fields and thick disks with high velocity dispersions are ubiquitous in the samples currently available in the literature (e.g. Law et al. 2009; Förster Schreiber et al. 2009; Wisnioski et al. 2015). A stellar mass dependence on the relative contributions of σ_g and V_{rot} appears to exist, although beam smearing (see Appendix) may provide the enhanced dispersion in some of the the smallest systems (Newman et al., 2013b). Kinematic data for low mass galaxies at these redshifts is currently limited. The advent of high sensitivity near-IR instruments (e.g. MOSFIRE, KMOS) will soon provide large samples of kinematics for galaxies with low stellar masses.

2.5 Conclusions

We study the stellar mass Tully-Fisher relation (TFR; stellar mass versus rotation velocity) for a morphologically blind sample of emission line galaxies in the field. The

galaxies are at a redshift of ~ 0.2, or a lookback time of about 2 Gyrs, and therefore we expect little evolution from the local TFR.

We report on a transition mass in the TFR which we call the "mass of disk formation," M_{df}. This mass separates galaxies which always form disks (masses greater than M_{df}) from those which may or may not form disks (masses less than M_{df}). For $M_* > M_{df}$, all galaxies in our sample are settled onto the local TFR. However, for $M_* < M_{df}$, galaxies can either lie on the TFR or scatter off of it to low rotation velocity. The galaxies which scatter off have higher disordered motions, as measured through integrated gas velocity dispersions (σ_g). Moreover, we find that galaxies on the TFR are morphologically distinct from those which scatter off. The quantitative morphologies of galaxies on the relation are on average less asymmetric and concentrated than those galaxies which scatter off.

2.6 Appendix

We perform mock observations of the 3D kinematics of local galaxies to investigate how well we are able to recover the rotation velocity of the smallest galaxies in our sample. These simulations show that we are able to recover rotation, if present, in the smallest galaxies in our sample.

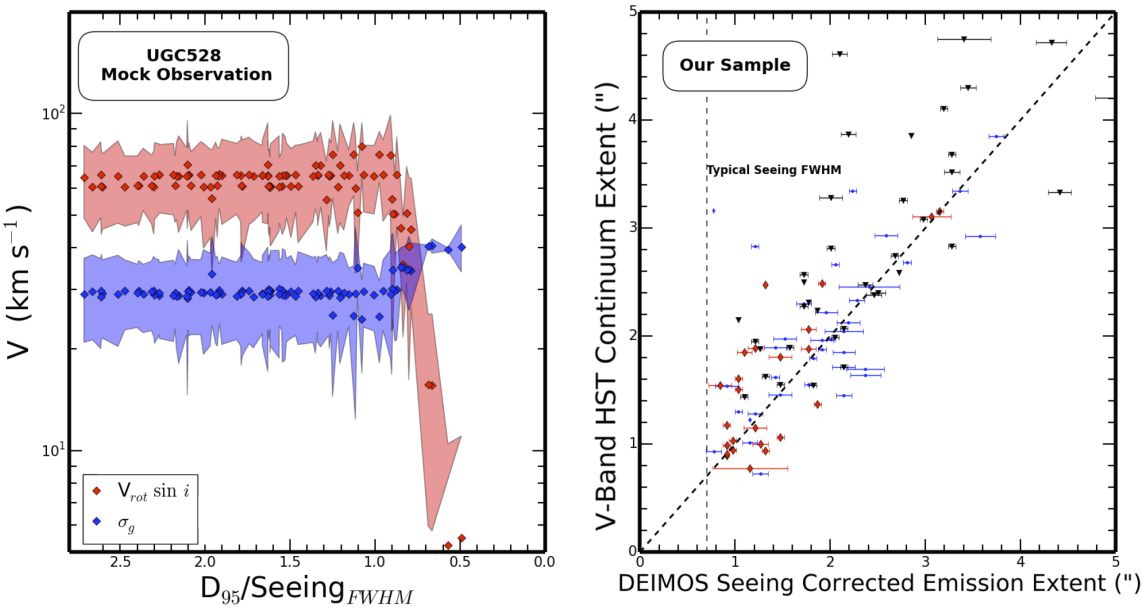

Figure 2.7: Left: Mock observations of UGC 528 at varying apparent sizes. The seeing is kept constant at 0.75″ for all mock observations. We are able to recover the true rotation velocity and average gas velocity dispersion down to a diameter, D_{95} = (0.87 ± 0.06) × seeing. Right: Measurements of the continuum and emission line extent for the galaxies in our sample. The continuum extent is defined as 4 × σ_{cont} of the intensity profile. For a Gaussian profile, this will equal D_{95}. For galaxy profiles with broader wings than a Gaussian, D_{95} will be larger than this value. The continuum is derived from the V-band image (rest B at z = 0.2) and should trace the young star forming regions. The seeing-corrected DEIMOS emission line extent is defined as 4 × $\sigma_{emission}$. The seeing for the observations in our sample ranged between 0.55″-1.20″ The number of galaxies for each bin in seeing are: [0.55 - 0.70”] 26 galaxies, [0.70 - 0.85”] 44 galaxies, [0.85 - 1.0”] 35 galaxies, [1.0 - 1.2”] 14 galaxies. The typical seeing for our sample is demarcated by the vertical black line. All of the galaxies in our sample are sufficiently large enough to reliably measure a rotation velocity, if present.

2.6.1 Modeling the effects of apparent size on measuring kinematics

Reliably measuring resolved kinematics for a galaxy depends critically on its apparent size relative to the seeing, i.e. beam smearing (Begeman 1987). Atmospheric turbulence blurs together intrinsically spatially separate velocity gradients, leading to a smoothing of the rotation field and a boosted central velocity dispersion (e.g. Weiner et al. 2006a). ROTCURVE models the seeing and recovers rotation curves and average integrated gas velocity dispersions for galaxies with apparent sizes larger than the seeing (see examples in Weiner et al. 2006a). Overcoming beam smearing with galaxies whose intrinsic size is comparable to the seeing is challenging and has been addressed by several papers with respect to IFS measurements at high redshift (e.g. Epinat et al. 2010; Davies et al. 2011).

To understand the effects of beam smearing on our measurements we perform mock observations of observed velocity and dispersion maps for a nearby galaxy from the literature. In particular, we use Fabry-Perot observations of UGC 528 from the GHASP survey (Epinat et al., 2010). We determine the apparent galaxy size (defined as the extent of the line emission) at which the intrinsic rotation velocity is no longer recovered under the observing conditions and instrumental set-up used by the DEEP2 Survey.

2.6.2 Mock Observations of UGC 528

UGC 528 is a small rotating local spiral galaxy of Hubble Type SAB(rs)b (Garrido et al., 2003). It has a rotation velocity $V_{rot}\sin(i) \sim 60$ km s^{-1} and a relatively high average dispersion across its face of $\sigma_g = 26.0 \pm 9.6$ km s^{-1}.

We build mock spectral cubes (3D: spatial $\times$ spatial $\times$ λ) from the available velocity, dispersion and flux maps. This allows us to perform mock observations for an arbitrary velocity sampling without needing to interpolate between slices. To do this, we first construct an empty cube with velocity sampling matching DEEP2, namely $\Delta v = 12.6$ km s^{-1} at z = 0.2. Next, using the flux, velocity and dispersion maps we fill the cube with model Hα emission. For each spaxel in the map with valid velocity information we create a Gaussian line profile with a mean line of sight velocity V_{los}, dispersion σ_g and amplitude scaled to match the integrated flux. This cube is then projected from its original redshift to z = 0.2 by resizing the spaxel scale. Each slice in the cube is then convolved with a 2D spatial Gaussian kernel (FWHM = 0.75″) to simulate seeing.

A mock 1″ wide slit is placed along the kinematic PA of the galaxy. From this we produce a mock spectrum using the DEEP2 pixel scales (0.118 ″/pixel, 0.33 $\AA$/pixel) and spectral resolution (R $\sim$ 5000). Noise is added to the 2D spectrum to match the typical pixel to pixel S/N profiles of our faintest sources.

We create separate cubes in this manner, each time varying the spatial size to simulate different apparent sizes for UGC 528. The final product is a set of 100

mock observations of UGC 528 at z = 0.2 ranging in size 0.4 -2.2″ with a 0.018″ step size. Each mock observation results in a 2D spectrum of the emission line for a given apparent size.

Next we run each of the mock spectra through ROTCURVE to measure kinematics. We fix the scale radius of UGC 528 in physical units to its true value of 0.6 kpc (Epinat et al., 2010). For reasonable values, we find that the chosen scale radius has little impact on the kinematic measurements, as was also found by Weiner et al. (2006a). We measure $V_{rot} \times \sin(i)$ and σ_g for each of the 100 mock spectra. The results of our test are demonstrated in Figure 2.7. As expected, at large intrinsic sizes relative to the seeing ($D_{95} > 1.5 \times$ seeing) we are able to recover the intrinsic rotation and integrated dispersion well. As the mock observations reach closer to and beyond the scale of the seeing, we note that the measured rotation velocity decreases and the measured dispersion increases as expected. To quantify the scale at which this turnover occurs, we fit a simple change point model using PyMC (Patil et al., 2010). The turnover to artificially low V_{rot} occurs at a scale of D_{95}/Seeing = 0.87 ± 0.06. This error incorporates both the measurement error imposed by the slit (red shading in Figure 2.7, left) and the error in the fit to the model.

We conclude from these mock observations that we can reliably measure rotation velocities for the galaxies in our sample down to D_{95}/Seeing = 0.87 ± 0.06.

2.6.3 Emission sizes vs HST Continuum sizes

We now compare the intrinsic sizes of the galaxies in our sample to the size of the seeing. In the right panel of Figure 2.7 we plot the size of the galaxy in emission, tracing areas of star-formation, against the size in continuum, tracing the young stellar population. The Hubble sizes are measured from the HST V-Band images and the emission sizes are measured directly from the DEIMOS spectra. The observed emission lines ($\sigma_{em,obs}$) are broadened by the combined PSF of the instrument and the seeing (σ_{PSF}). We can recover the true extent of the emission line ($\sigma_{em,corr}$):

$$\sigma_{em,corr} = \sqrt{\sigma^2_{em,obs} - \sigma^2_{PSF}} \tag{2.1}$$

For an approximate 1-D Gaussian profile, the diameter containing 95% of the flux will be 4 times this value. In reality, intrinsic emission profiles of galaxies will be broader than a Gaussian distribution and the value of $\sigma_{em,corr}$ is primarily determined by the profile of the core. A galaxy profile with broader wings than a Gaussian will have a D_{95} that is larger than that given by $4 \times \sigma_{em,corr}$. The HST V-band (rest B at z $\sim$ 0.2) extent correlates well with the seeing-corrected emission line sizes (Figure 2.7, right). We demarcate the typical seeing size of $0.75''$.

The smallest galaxies in our sample reach down to seeing-corrected emission extents of $\sim 1.2''$ (or 1.6 times the typical seeing FWHM), well into the predicted regime for accurately recovering the kinematics (Figure 2.7; left panel). In conclusion, it is unlikely that our low mass dispersion dominated galaxies are dispersion-dominated

because of beam-smearing.

Chapter 3

Kinematic Downsizing at $z \sim 2$

In this chapter, we present results from a survey of the internal kinematics of 49 star-forming galaxies at $z \sim 2$ in the CANDELS fields with the Keck/MOSFIRE spectrograph (SIGMA, Survey in the near-Infrared of Galaxies with Multiple position Angles). Kinematics (rotation velocity V_{rot} and gas velocity dispersion σ_g) are measured from nebular emission lines which trace the hot ionized gas surrounding star-forming regions. We find that by $z \sim 2$, massive star-forming galaxies ($\log M_*/M_\odot \gtrsim 10.2$) have assembled primitive disks: their kinematics are dominated by rotation, they are consistent with a marginally stable disk model, and they form a Tully-Fisher relation. These massive galaxies have values of V_{rot}/σ_g which are factors of 2–5 lower than local well-ordered galaxies at similar masses. Such results are consistent with findings by other studies. We find that low mass galaxies ($\log M_*/M_\odot \lesssim 10.2$) at this epoch are still in the early stages of disk assembly: their kinematics are often dominated by gas

velocity dispersion and they fall from the Tully-Fisher relation to significantly low values of V_{rot}. This "kinematic downsizing" implies that the process(es) responsible for disrupting disks at $z \sim 2$ have a stronger effect and/or are more active in low mass systems. In conclusion, we find that the period of rapid stellar mass growth at $z \sim 2$ is coincident with the nascent assembly of low mass disks and the assembly and settling of high mass disks.

3.1 Introduction

The cosmic star-formation rate peaks between $z = 1.5$ and $z = 2.5$ (Madau & Dickinson, 2014) and marks a critical period for galaxy assembly. In the classic model of galaxy formation, collisional baryons cool and dissipate into the center of dark matter halos while conserving primordial angular momentum, leading to the formation of a thin rotating disk galaxy (Fall & Efstathiou, 1980; Mo et al., 1998). Although this gas is expected to collapse to a disk in a few crossing times, external processes can disrupt or destroy disks on timescales shorter than the rotational period. In an emerging new picture, clumpy and smooth accretion from the cosmic web can efficiently carry external angular momentum inside the halo viral radius and directly onto the central galaxy (Brooks et al., 2009; Kimm et al., 2011; Stewart et al., 2013; Danovich et al., 2015), disrupting the velocity field (Aumer et al., 2010; Elmegreen & Burkert, 2010; Genel et al., 2012; Zolotov et al., 2015). Additionally, ordered disks

can be disturbed or destroyed through major mergers (Barnes & Hernquist, 1996; Hopkins et al., 2009; Covington et al., 2010), violent disk instabilities (Dekel et al., 2009; Inoue et al., 2016) and stellar feedback (Mac Low & Ferrara, 1999; Lehnert et al., 2009; Agertz & Kravtsov, 2016; Wheeler et al., 2017).

These processes are prominent at $z \sim 2$, coincident with the assembly of stellar mass in galaxies and may play a stronger role in the shallow potential wells that host low mass galaxies. In general, the formation and development of a galaxy depends strongly on its mass. Massive galaxies tend to assemble their stellar mass first ("downsizing", e.g., Cowie et al. 1996; Brinchmann & Ellis 2000; Juneau et al. 2005) and develop disks earlier (e.g., Kassin et al. 2012; van der Wel et al. 2014b). In contrast, low mass ($\log M_*/M_\odot \lesssim 10$) galaxies tend to exhibit more disturbed and irregular morphologies at both low and high redshift (e.g., Mortlock et al. 2013; Simons et al. 2015), indicating that they lack mature structure. Recent evidence from imaging suggests that a significant fraction of low mass galaxies at $z > 1.5$ have elongated stellar distributions (van der Wel et al., 2014b). A similar phenomenon has been seen in hydrodynamic simulations of galaxy formation (Ceverino et al., 2015; Tomassetti et al., 2016) which indicate that oblate (stellar) disks form at late times ($z \lesssim 2$), when the central potential becomes baryon-dominated. The star-forming gas in these simulated galaxies starts off in a highly perturbed and triaxial state, eventually collapsing to form thick oblate disks (Tomassetti et al., 2016; Mandelker et al., 2017).

From $z \sim 1.2$ to now, star-forming systems appear to have evolved through kinematic downsizing in a process known as "disk settling" (Kassin et al., 2012). In this picture, galaxies hierarchically settle from turbulent systems with high dispersion to regularly rotating disks, with more massive galaxies forming disks earlier. Locally: the majority of high mass galaxies are ordered rotating disks, with kinematically disordered galaxies appearing only below a stellar mass of $\log M_*/M_\odot < 9.5$ (Simons et al., 2015). However, it is unclear whether the kinematic downsizing picture extends beyond $z \sim 1.2$ and into the peak of cosmic star-formation.

With recent advancements in near infrared detectors and instrumental multiplexing capabilities, space and ground based instruments have provided a wealth of knowledge regarding the physical properties of galaxies during this period, the cosmic noon. Ground based kinematic data for high redshift ($z \gtrsim 1$) galaxies is rapidly growing, as reviewed in Glazebrook 2013, with several recent and ongoing surveys: e.g., SINS (Förster Schreiber et al., 2009), WiggleZ (Wisnioski et al., 2011), MASSIV (Contini et al., 2012), MOSDEF (Kriek et al., 2015), KMOS3D (Wisnioski et al., 2015) and KROSS (Stott et al., 2016).

Emerging from these surveys is the general picture that star-forming galaxies at $z \sim 2$ are *unlike* the thin disk galaxies that make up the massive end up the local Hubble sequence. High redshift galaxies tend to be thick and gas-rich with velocity dispersions that are factors of a few higher than local thin disks. The typical velocity dispersion tends to increase with increasing redshift (e.g., Puech et al. 2008; Kassin

et al. 2012) and may reflect a similar rise in gas fractions (Wisnioski et al., 2015). Even still, rotational support appears to be relatively common in the more massive galaxies ($M_*/M_\odot \gtrsim 10$) at $z \sim 2$, with $\sim$ 75% of the population exhibiting rotational motions comparable to or greater than their velocity dispersion (Wisnioski et al., 2015).

Only very recently, kinematic data for low mass galaxies ($\log M_*/M_\odot \lesssim 10$) at high redshift is becoming available in gravitationally lensed systems (e.g., Jones et al. 2010; Livermore et al. 2015) and in larger numbers in the ongoing surveys with multi-object single slits (MOSDEF; Price et al. 2016) and integral field spectrographs (KMOS-3D; Wisnioski et al. 2015). While the imaging data at this epoch indicates that massive galaxies tend to be disk-like and the low mass galaxies tend to be irregular, similar conclusions have not yet been drawn from kinematic measurements, and it is unclear whether kinematic downsizing is in effect at $z \sim 2$.

In this chapter we aim to take advantage of the multiplexing capabilities and the high sensitivity of Keck/MOSFIRE multi-object near-infrared spectrograph (McLean et al., 2012) as well as the high resolution and sensitivity of Hubble Space Telescope (HST)/WFC3 H-band imaging to explore the kinematic state of star-forming galaxies at $z \sim 2$. This survey is named SIGMA, Survey in the near-Infrared of Galaxies with Multiple Angles. The sample is morphologically diverse and is selected along the star-formation main sequence in two redshift bins from $1.3 < z < 1.8$ and $2.0 < z < 2.5$.

In §2 we discuss the observations and sample selection. In §3 we describe mea-

surements of the galaxy physical properties from multi-wavelength imaging. In §4 we detail the measurements of the gas-phase kinematics of our sample, and discuss multi-PA observations. In §5 we present the $z \sim 2$ Tully-Fisher relation. In §6 we examine trends between the kinematics and physical properties, and in §7 we present a comparison of our galaxies with a model for marginally stable gas-rich disks. In §8 we present our conclusions and in the appendix we present simulations to determine the effects of spatial resolution on the measurement of kinematics. We adopt a ΛCDM cosmology defined with (h, Ω_m, Ω_Λ) = (0.7, 0.3, 0.7).

3.2 Observations and Sample Selection

The SIGMA sample is drawn from three of the fields (GOODS-S, GOODS-N and UDS) of the HST/WFC3 CANDELS survey (Grogin et al., 2011; Koekemoer et al., 2011). All of the spectra in GOODS-N were taken as a part of the TKRS-2 survey (Wirth et al., 2015) and a subset of the spectra in GOODS-S and UDS have been presented in previous papers (Trump et al., 2013; Barro et al., 2014). The SIGMA galaxy sample is shown in a star formation rate - stellar mass (SFR - M_*) diagram in Figure 3.1.

This sample is a part of the well studied GOODS-N, GOODS-S, and UDS extragalactic fields, and so extensive multi-wavelength imaging is available for all of the galaxies in this sample. Galaxies in SIGMA are selected from the CANDELS

WFC3/F160W catalogs (Galametz et al., 2013; Guo et al., 2013) as follows. Selection priority was given to galaxies with spectroscopic redshifts from HST/WFC3 grism observations (Morris et al., 2015), taken as a part of the 3D-HST (Brammer et al. 2012; Momcheva et al. 2016, PI Van Dokkum) and AGHAST (PI Weiner) surveys. The majority of the TKRS-2 galaxies were selected on previous spectroscopically confirmed redshifts. Photometric redshifts were derived from the broadband SEDs with EAzy (Brammer et al., 2008; Dahlen et al., 2013) and were used to select the remaining galaxies in our sample. Star-forming galaxies were selected down to a SFR of $\sim$3 $M_\odot$ yr^{-1} at z $\sim$ 1.5 and $\sim$10 $M_\odot$ yr^{-1} at z $\sim$ 2.2. There is no selection cut on morphology. As such, both regular and irregular galaxies are included in the sample. There is a priority weight on galaxy size, half-light V-band diameters of $> 0.5''$, in order to select galaxies with emission extents that are larger than the typical seeing.

The full SIGMA sample for which we have significant detections (S/N > 3) in Hα and/or [O III]λ5007 contains 97 galaxies. A portion of these were observed at multiple slit position angles (PA): 23 with 2 PAs and 11 with 3+ PAs. We select galaxies with at least one kinematic measurement coincident with the photometric major axis (within 45°), removing 35 of the 97 galaxies. We make a further cut on emission line extent for each spectrum of each galaxy, as described in §3.3 and the Appendix, such that the effective radius of the emission extent is at least 0.8 times the size of the seeing FWHM. This selection is shown in Figure 3.2 and removes an additional 9 galaxies from the sample. An additional 4 galaxies are removed due to

the presence of a strong overlapping skyline.

The final sample used in this chapter contains 49 galaxies, 28 in the redshift range $1.3 < z < 1.8$ and 21 at $2.0 < z < 2.5$. The properties of the full sample are presented in Table 3.1 of the Appendix.

3.2.1 NIR Spectra

The strong optical nebular emission lines (e.g., Hα, [O III]λ5007) from which we measure kinematics shift into the near infrared (NIR) at $z > 1.3$. The multi-object spectrograph, MOSFIRE (McLean et al., 2012) on Keck-I, is one of the premiere instruments to study spectral features in the NIR. The spectra in this sample were taken in the H-band (1.46-1.81 μm) and K-band (1.93-2.45 μm). Hα can be detected in the H-band from $1.3 < z < 1.8$ and in the K-band from $2.1 < z < 2.8$. Additionally, [O III]λ5007 falls in the H-band from $2.0 < z < 2.8$.

The MOSFIRE slit width was set to $0.7''$ and the instrumental spectral resolution is $R \sim 3630$ in both bands ($\sigma_{inst,HK} = 35$ km s^{-1}). The masks were dithered along the slit between symmetric sky positions around the initial pointing to facilitate sky and instrument noise subtraction. The on-source exposure times were between 90 and 120 minutes with individual exposure times of 120 seconds. The 2D spectra were sky-subtracted, wavelength-calibrated and rectified using the MOSFIREDRP reduction pipeline[1]. Spectroscopic redshifts were determined via Specpro (Masters & Capak,

[1]http://www2.keck.hawaii.edu/inst/mosfire/drp.html

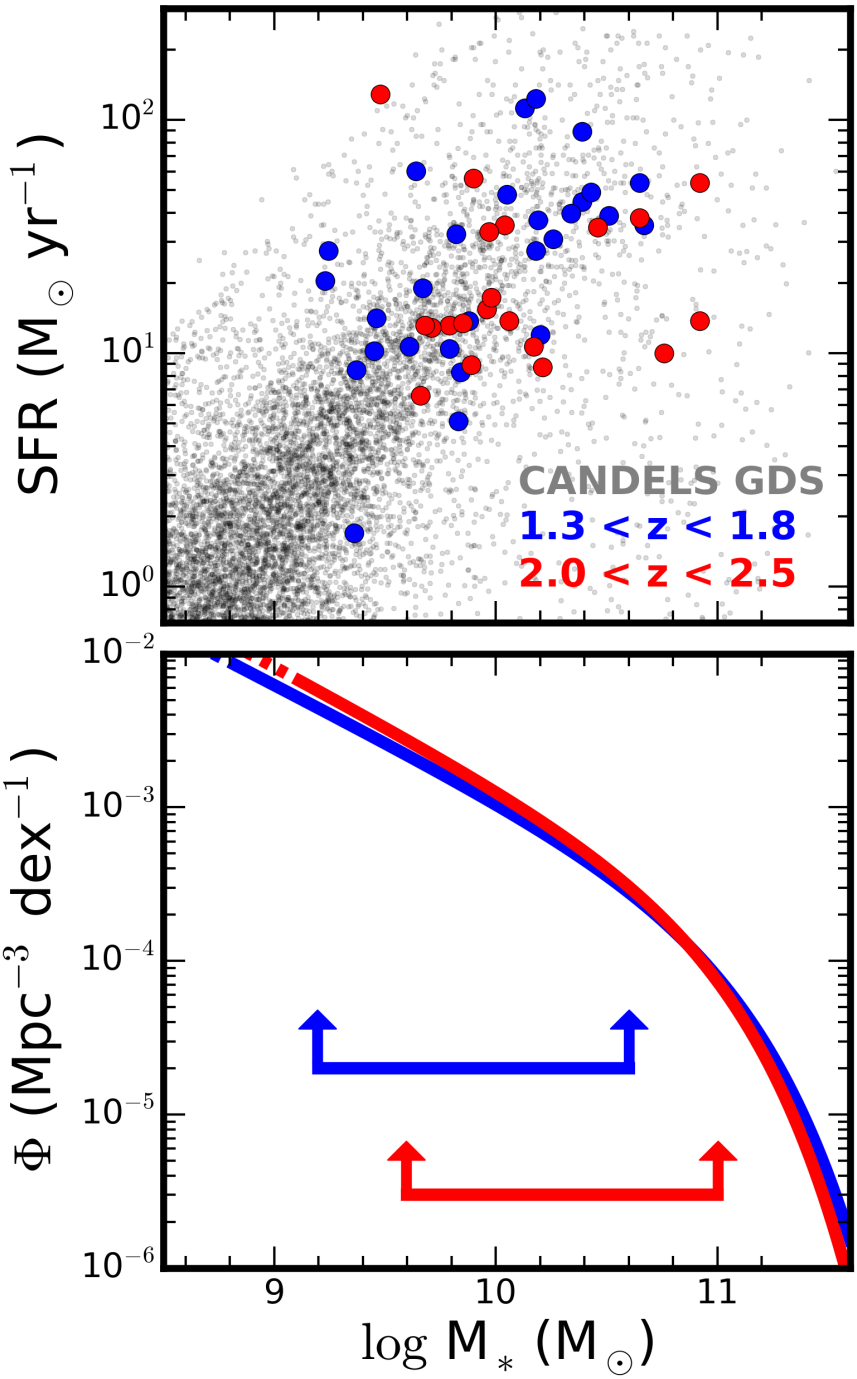

Figure 3.1: Caption on next page.

Figure 3.1: Galaxies in SIGMA (large filled points) lie along the star-formation main sequence down to a stellar mass of $\log M_*/M_\odot = 9.2$ at z $\sim$ 1.5 and $\log M_*/M_\odot = 9.6$ at z $\sim$ 2.3. The grey dots represent galaxies drawn from the H-band selected GOODS-S CANDELS catalog in the same redshift range. A small amount of noise (0.05 dex) was added to the grey points to remove striations due to the discreet grid structure searched by the model fits to M_* and star-formation rate (SFR). In the bottom panel, we compare the mass range of our sample, indicated by the red and blue arrows, with the blue galaxy stellar mass functions at the same redshifts, taken from Mortlock et al. (2015).

2011).

Observations were taken in natural seeing conditions and the size of the seeing is estimated from unresolved calibration stars, where available, and marginally resolved compact "blue nugget" galaxies (Barro et al., 2014) that were observed on the same mask as the galaxies in our sample. The NIR seeing ranged between 0.45 and 0.85″. Example cutouts of the 2D spectra around the Hα emission line are shown in Figure 3.3.

3.3 Quantities Measured from Imaging

3.3.1 Structural Parameters

Throughout this chapter we use two structural parameters measured from the HST/WFC3 images, namely the photometric position angle (PA, i.e., the direction of

the photometric major axis) and the photometric axis ratio (b/a). For a well-behaved disk galaxy, the photometric PA will align with the kinematic PA (the direction of the largest velocity gradient) and the axis ratio can be used to correct the derived rotation velocity for the inclination of the galaxy to the line of sight. The photometric PA and axis ratio were measured with `GALFIT` (Peng et al., 2010) by van der Wel et al. (2012) on the H-band (F160W), J-band (F125W) and Y-band (F105W) for all of the H-Band selected CANDELS galaxies in our fields. We refer to these papers for measurement details. For this chapter, we adopt the H-band measurements (rest I at $z \sim 1.5$, rest V at $z \sim 2.5$).

3.3.2 Stellar Masses and Star-Formation Rates

The available broadband measurements span from the UV to the NIR with ancillary Spitzer/MIPS 24/70μm photometry and Herschel far-IR photometry from the GOODS-Herschel (Elbaz et al., 2011) and PACS Evolutionary Probe (Magnelli et al., 2013) surveys.

As described in Barro et al. (2014), integrated stellar masses (M_*) were derived from the broadband SED of each galaxy using the FAST fitting code (Kriek et al., 2009) assuming a Chabrier (2003) initial mass function, Bruzual & Charlot (2003) stellar population synthesis models and a Calzetti et al. (2000) extinction law. The errors on the stellar masses are $\sim$0.3 dex (Mobasher et al., 2015). Dust-corrected star-formation rates were derived following the SFR-ladder (Wuyts et al., 2011). For

galaxies with Spitzer and Herschel far-IR detections, the SFR is calculated from both the obscured (IR) and unobscured (UV) components (following Kennicutt 1998a). For non-detections in the mid-far IR, the star-formation rates are derived from the UV and are extinction-corrected following the best fit attenuation from the SED modeling. In Figure 3.1 we show the star-formation rate vs stellar mass diagrams for our sample, the "star-formation main sequence" (e.g. Noeske et al. 2007). Galaxies drawn from the full CANDELS catalog in GOODS-S are shown by black dots in the background. Our sample is generally representative of the SF main sequence down to a stellar mass log $M_*/M_\odot = 9.2$ in the $1.3 < z < 1.8$ redshift bin and 9.6 in the $1.8 < z < 2.8$ bin. We make a comparison with the blue galaxy stellar mass functions at $1.5 < z < 2.0$ and $2.0 < z < 2.5$ (Mortlock et al., 2015) and note that our sample spans close to the knee of the Schechter function, $M^* \sim 10^{11}\, M_\odot$, in both redshift intervals.

3.3.3 Continuum and Emission Sizes

One of the main challenges to measuring rotation with ground based data comes from the effects of beam smearing (Begeman, 1987). Seeing smooths out velocity gradients and artificially boosts the velocity dispersion in the central parts of rotating galaxies. This effect can generally be modeled, except in the cases where the emission extent is comparable to or smaller than the seeing. Galaxies with small emission extents can appear dispersion-dominated in seeing-limited data but reveal rotation

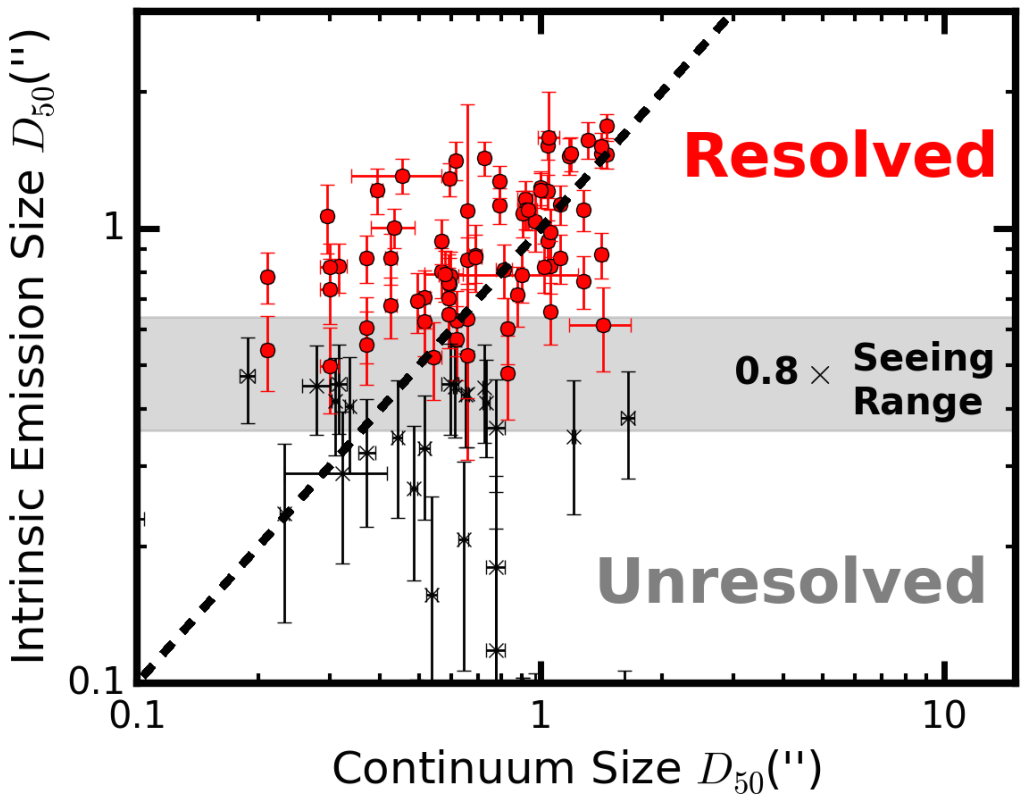

Figure 3.2: Spatially resolved observations are identified from the intrinsic extents of their emission lines. We plot the intrinsic half-light diameter (D_{50}) of the emission versus the continuum for each slit on every galaxy used in this chapter. Resolved observations are marked with red filled circles and the discarded unresolved observations are marked as black x's. The range of seeing conditions during the observations is shown as a grey shaded swath. Emission line sizes are seeing corrected from the MOSFIRE 1D emission profile. Continuum sizes are measured from Sersic fits to the H-band Hubble images. As shown in the Appendix, kinematic structure can be resolved down to a limiting resolution of $D_{50} = 0.8\times$ Seeing$_{FWHM}$, where D_{50} is the 1D seeing-corrected emission line size.

at higher resolution (Newman et al., 2013b).

In order to examine the effects of beam-smearing on our data, we produce a suite of simulated MOSFIRE/SIGMA spectra in the Appendix. We conclude that, for the typical signal to noise of the spectra in our sample, we can reliably recover intrinsic kinematics (V_{rot}, σ_g) down to $D_{50} \approx 0.8 \times \mathrm{Seeing}_{FWHM}$, where D_{50} is the 1D half-light diameter measured from the emission lines and Seeing_{FWHM} is the full width at half maximum of the seeing.

We make size selections using the emission rather than the continuum for a couple of reasons. First, the 2D half-light radii of the emission typically extend beyond the continua (Nelson et al., 2016). Secondly, seeing tends to blur emission that is not coincident with the slit placement into the slit (Weiner et al., 2006a). As such, an emission size determined from a projection of the slit onto the HST image may underestimate the extent of the emission measured with the slit. By measuring sizes directly from the seeing-corrected emission lines, we bypass both of these uncertainties.

In Figure 3.2 we show the half-light diameter sizes, in both emission and continuum, for the galaxies in our sample. For each slit, the emission line size is measured directly from the spectrally-collapsed emission line. Due to the convolution of the intrinsic profile with the seeing, the spatial profiles of the spectrally-collapsed emission lines are generally well described by a 1D Gaussian. The seeing is subtracted from the observed profile in quadrature ($\sigma_{em,intrinsic} = \sqrt{\sigma^2_{em,observed} - \sigma^2_{seeing}}$) and the half-light size is measured from the recovered intrinsic profile.

Continuum radii are measured from the HST/WFC3 H-Band image using the `GALFIT` software package in van der Wel et al. (2012). For the galaxies in our sample, the half-light radii of the intrinsic emission profiles tend to be slightly larger than the continuum sizes. This could be the case for two reasons. First, the half-light radius that is measured by `GALFIT` is a 2D quantity measured on concentric ellipses while the emission size is being measured directly from the 1D emission lines, an along-the-slit measurement. Since the 1D measurement essentially integrates the light across the slit, these two sizes will not directly scale to one another in general. The difference may also be physical, in the sense that the emission profile can extend beyond that of the continuum (Nelson et al. 2016).

3.4 Kinematics measured from emission lines

Kinematics are measured from strong nebular emission lines (Hα, [O III]λ5007]) in the spectra. These lines generally trace the hot (T $\sim 10^4$ K) ionized gas in HII regions surrounding ongoing star-formation. The kinematics are measured using the code `ROTCURVE` (Weiner et al., 2006a). The instrumental resolution of our spectra (R $\sim$ 3630) allow us to measure the velocity dispersion down to $\sim$ 20 km s^{-1} and the rotation velocity uncorrected for inclination ($V_{rot} \times \sin i$) to $\sim$ 15 km s^{-1}.

The kinematic modeling performed by `ROTCURVE` has been described in detail in

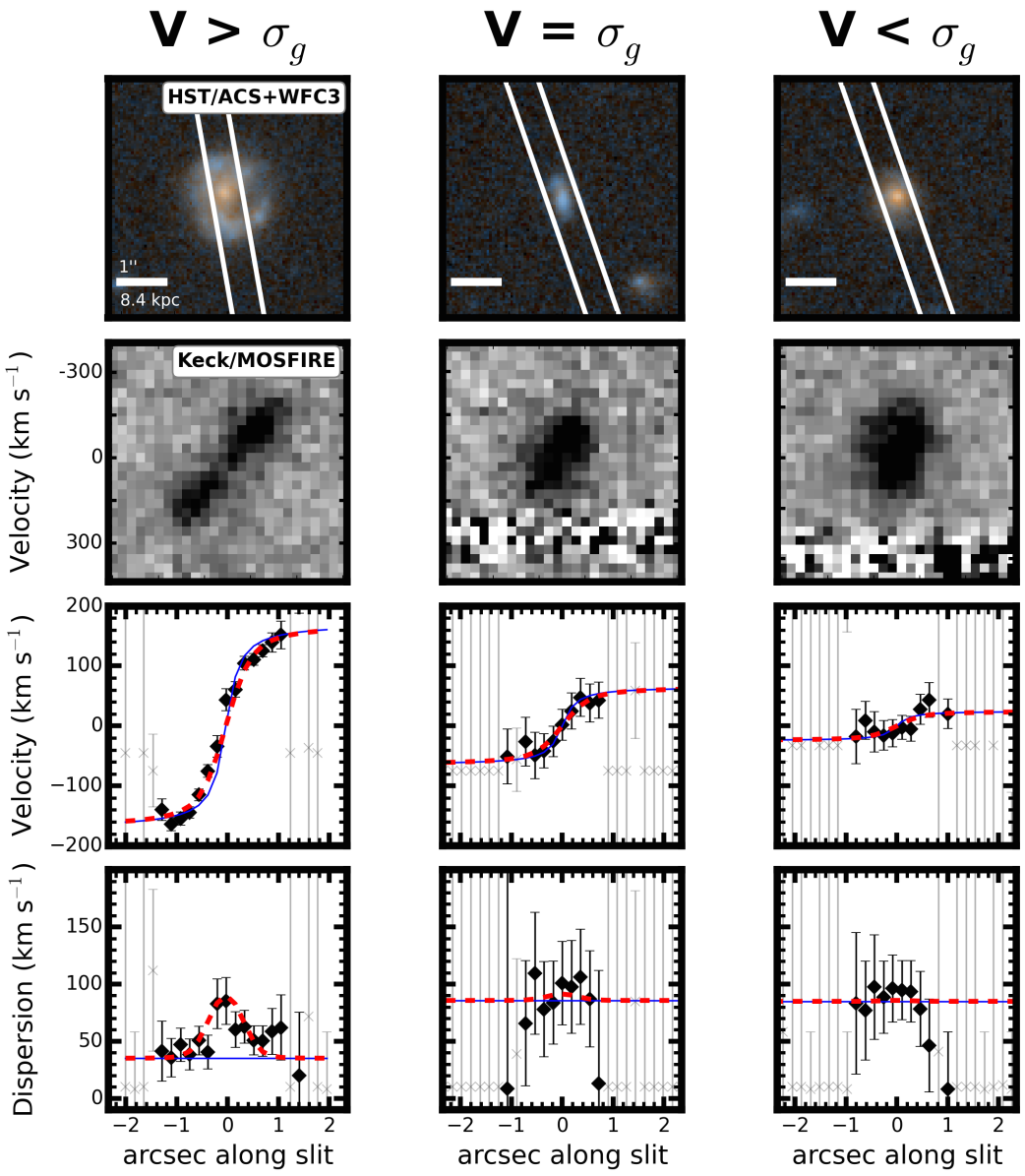

Figure 3.3: Caption on next page.

Figure 3.3: Example single slit observations are presented for three SIGMA galaxies (ID: 16600, 16209, 14602). These galaxies span the kinematic types in our sample: a rotation dominated galaxy (left column), a galaxy with equal contributions of rotation and dispersion (middle column), and a dispersion dominated galaxy (right column). In the top two rows we show the I+H-band HST/ACS-WFC3 color images with the MOSFIRE slit placement and the 2-D spectra centered around the Hα line. Strong NIR atmospheric lines are present in the middle and right columns. In the bottom two rows we show the kinematic model fits to the emission lines. The black filled diamonds represent the gaussian fits to the velocity and velocity dispersion in each row of each spectrum. The grey points are poor fits and are discarded. The best-fit models are shown as red solid lines and the intrinsic (pre-seeing blurred) models are shown as blue dashed lines. All of the rows are spatially aligned and each panel is 4.5″ on a side. Kinematic fits for all of the SIGMA galaxies are available in the Appendix.

previous papers, so we will briefly outline it here and refer to Weiner et al. (2006a) for further details. `ROTCURVE` models the spatial profile of the emission line as a 1D Gaussian. In each row along the slit, we recover a velocity and velocity dispersion using an uncertainty-weighted least squares fit to a 1D Gaussian. Nearby, but not overlapping, skylines are manually masked to prevent noise peaks from driving the fit. The velocity structure of the line is modeled with two components: a rotation curve and a dispersion term. Due to our limited spatial resolution, the velocity dispersion is kept constant with radius in the model. The rotation velocity is modeled with an arctan function:

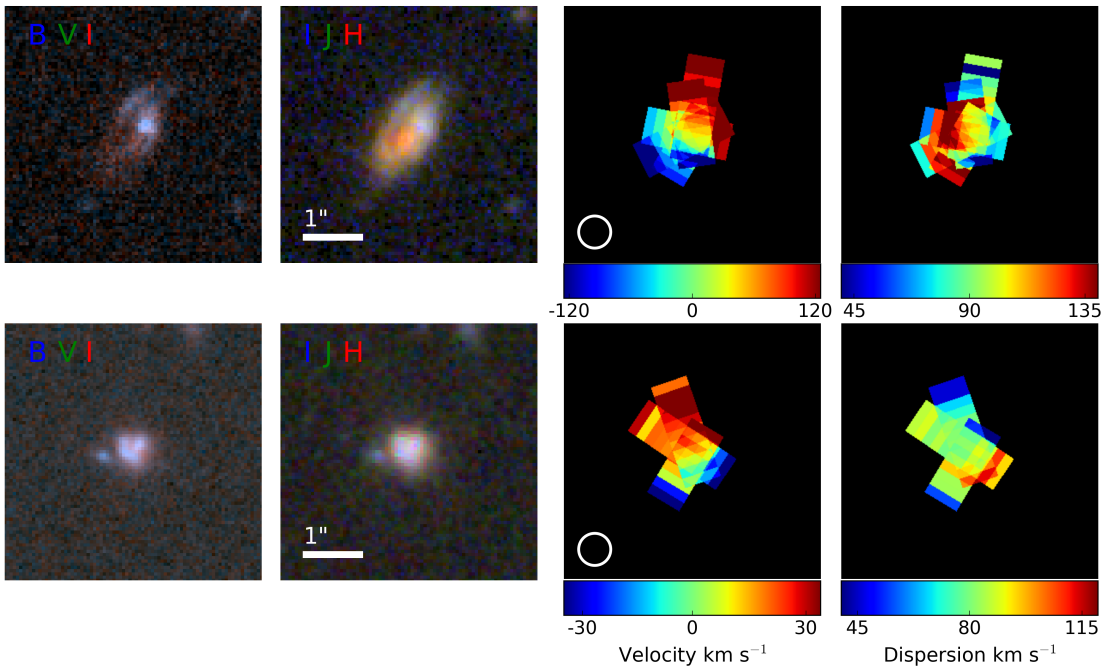

Figure 3.4: Hubble images and reconstructions of 2D kinematic fields from multi-slit observations are shown for two SIGMA galaxies (ID: 26736, 21162). In the first two columns we show the the HST/ACS optical (rest UV) and the HST/WFC3 near-IR (rest optical) color images, respectively. In the third and fourth columns, we show the co-added velocity ($V \times \sin i$) and velocity dispersion maps, respectively. The top row shows a regularly rotating disk galaxy: the velocity field has a smooth rotation gradient with a centrally peaked velocity dispersion, both kinematic signatures of a rotating disk. The bottom row shows a dispersion dominated galaxy with complex morphology and kinematics: it exhibits velocity gradients in orthogonal slits. Each slit pixel is $0.18''$ and the slits are $0.7''$ wide. The typical seeing in the H-band is $0.6''$, as shown by the white circles on the velocity maps.

$$V_x = V\frac{2}{\pi}\arctan(x/r_v) \tag{3.1}$$

where r_v is the knee radius for the turnover of the rotation curve and V is the velocity of the flat part of the rotation curve. We note that the flat part of the rotation curve is not reached in a fraction of our galaxy sample (see Appendix) and in these cases V is driven by the scale of the velocity difference reached by the data and the modeled turnover radius. Due to the seeing blur, r_v is not well constrained and so we fix the turnover radius in the model at a fiducial value of $0.2''$ (1.7 kpc at $z \sim 2$) and adjust to $0.3''$ or $0.4''$ for galaxies that are not well fit initially. The turnover radius and the rotation velocity are moderately covariant with a $\pm 0.1''$change in r_v resulting in a ± 0.1 dex change in V. The model parameters of V and σ_g are explored on a grid of 5 km s^{-1}. The modeled emission line is then spatially convolved with a fixed seeing kernel ($0.6''$ FWHM), which is the typical seeing of our observations in the NIR. The best fit model is determined through a χ^2 minimization with the data over this grid.

The velocity dispersion term that we measure (σ_g) is unlike a pressure supported stellar velocity dispersion. The hot gas which σ_g is tracing can collisionally radiate and so a high dispersion system cannot remain in equilibrium after a crossing time. Due to the seeing blur, the velocity dispersion is a measure of the small scale velocity gradients below the seeing limit. The velocity dispersion measured from nebular emission lines will be a combination of: (i.) thermal broadening of the gas ($\sim$10 km s^{-1} for H at 10^4 K), (ii.) internal turbulence in HII regions ($\sim$ 20 km s^{-1} for local

HII regions; Shields 1990), (iii.) relative motions between HII regions.

The inclination is measured as $\cos^2 i = ((a/b)^2 - \alpha^2)/(1 - \alpha^2)$, where α is the correction for the thickness of the disk ($\alpha = 0.2$) and b/a is the axis ratio of the galaxy, measured from the HST H-band image. The rotation velocity is then corrected as $V_{rot} = V/\sin i$.

As indicated by Hung et al. (2015, 2016), distinguishing late-stage mergers and rotating disks is difficult in low resolution kinematics observations. At high redshift, where galaxy mergers are expected to be common (Rodriguez-Gomez et al., 2015), disk classifications made from kinematic signatures alone may be biased high. In 2 galaxies in our sample (ID: 21897 and 4476) we identify an interacting neighbor in both the HST image ($< 1''$) and the MOSFIRE spectrum ($< 100\,\mathrm{km\ s^{-1}}$). We mask the emission line of the neighboring source in both of these cases. We note that late-stage interactions, for which two galaxies are identified as a single source, may be included in this sample. A joint analysis of the HST imaging and the kinematic data is necessary to disentangle disks from late-stage mergers in our sample. For all subsequent analyses, we interpret the measured velocity gradient of each galaxy as rotation.

In Figure 3.3, we show example kinematic fits for three galaxies in our sample: a strongly rotating galaxy, a galaxy with comparable velocity and velocity dispersion, and a dispersion dominated galaxy. Even in the dispersion dominated case, we note the presence of a velocity gradient, although it is small compared to the observed

dispersion. The rotationally supported system is a well-ordered disk galaxy, similar to disk galaxies today, with the presence of spiral structure and a bar in the HST image. In its spectrum, we find a strong rotation signature ($\sim$ 175 km s^{-1}) and a mild velocity dispersion ($\sim$ 35 km s^{-1}).

Beam smearing tends to blur together spatially separate regions of emission, leading to a flattening of nearby velocity gradients and an elevation in the local velocity dispersion. In the observed line, this effect leads to a classic peak in the velocity dispersion at the center of the galaxy, where the velocity gradient is the steepest. This can be seen in the example kinematic fits in Figure 3.3, particularly for the strongly rotating galaxy. `ROTCURVE` models the seeing and accounts for this artificial beam smearing when constructing its model.

The best-fit kinematic parameters of the full sample are presented in Table 3.2 of the Appendix.

3.4.1 Multiple Position Angle Observations

Single-slit spectroscopy is a reliable method for recovering rotation velocity and velocity dispersion in observations where the position angle of the slit is aligned with the kinematic major axis of the galaxy. In ordered disk galaxies, the kinematic and photometric major axes are aligned and so the HST/WFC3 image can be used to determine the kinematic major axis. However, the morphologies of high redshift star-forming galaxies can be more severely disturbed than local or low redshift samples

(e.g., Mortlock et al. 2013), implying that the photometric and kinematic major axes might be misaligned. In a sample that combines galaxies at both $z \sim 1$ and $z \sim 2$, Wisnioski et al. (2015) report that kinematic and photometric axes are at least moderately misaligned ($> 15°$) in ∼40% of galaxies and are largely misaligned ($> 30°$) in ∼20%. This fraction declines to $< 10\%$ in local galaxies (Barrera-Ballesteros et al., 2015).

For seeing-limited observations of high redshift galaxies, slit placement is much less stringent than for local galaxies or for higher resolution observations. To recover rotation, the alignment between the slit and the kinematic major axis should be within 45° (see Figure 13 of Weiner et al. 2006a).

A total of 26 galaxies in SIGMA have observations at multiple position angles (PA_{slit}, see Figure 3.4). Due to the non-uniform coverage of our maps, we do not simultaneously model all of the observed slits on a galaxy. Instead we examine the kinematic measurements along each slit separately and adopt measurements for the slit with the highest rotational signature. We require that every galaxy in SIGMA have at least one slit that is aligned within 45° of the photometric major axis (PA_{phot}). This requirement ensures that rotation will be recovered in disk galaxies, where the photometric and kinematic axes are aligned. Of the 26 galaxies with kinematic measurements at more than one PA, 17 have at least one slit aligned and one slit misaligned with PA_{phot}. Of these systems, we find the largest velocity gradient in a misaligned slit in 23% of the cases (4 galaxies) and in an aligned slit in 77% of the

cases (13 galaxies). This result is consistent with Wisnioski et al. (2015). The 4 galaxies in our sample for which the strongest velocity shear is found in a misaligned slit all display complex morphology in both the HST/ACS V-band and HST/WFC3 H-band images.

For these 4 galaxies, we adopt the line of sight velocity shear ($\Delta V/2$) for our analysis and do not correct the velocity for inclination. These galaxies are marked in all of the figures. As shown in an example in Figure 3.4, these systems tend to have complex velocity profiles. In some of these cases, velocity shear is found in the aligned slit as well, implying that the velocity gradient (either tracing global rotation or more complex motions) may lie between both slits.

3.5 The Tully-Fisher Relation

3.5.1 Background

The Tully-Fisher relation (TF; Tully & Fisher 1977) is an empirical scaling relating the dynamics and the luminosity, or more recently, stellar mass of galaxies. In the local universe, the relation is relatively tight for massive disk galaxies (e.g., Verheijen 2001; Bell & de Jong 2001; Pizagno et al. 2005; Kassin et al. 2006; Courteau et al. 2007; Masters et al. 2008; Reyes et al. 2011) but begins to show small residuals to low mass for gas-rich galaxies (McGaugh, 2005; Bradford et al., 2016) and large residuals to low rotation velocity for irregular low mass galaxies ($\log M_*/M_\odot \lesssim 9.5$)(Simons

et al., 2015).

Numerous studies have extended the analysis of the TF relation to both intermediate, $0.1 < z < 1.3$ (e.g., Conselice et al. 2005; Flores et al. 2006; Weiner et al. 2006b; Kassin et al. 2007; Puech et al. 2008; Miller et al. 2011; Torres-Flores et al. 2011; Miller et al. 2011; Kassin et al. 2012; Vergani et al. 2012; Miller et al. 2014; Contini et al. 2016), and high redshift, $1.3 < z < 3.0$ (e.g., Cresci et al. 2009; Miller et al. 2012; Swinbank et al. 2012; Livermore et al. 2015).

Flores et al. (2006) and Weiner et al. (2006a) were the first to note that intermediate redshift galaxies with perturbed/complex kinematics and irregular morphologies tend to exhibit large scatter from the TF relation, with subsequent studies confirming such findings (e.g., Kassin et al. 2007; Torres-Flores et al. 2011; Vergani et al. 2012). Recent lensing work at high redshift has also found evidence for scatter to low rotation velocity from the TF relation for a handful of low mass galaxies (Jones et al., 2010; Livermore et al., 2015). However, due to a combination of sensitivity limitations and survey selection, the low mass regime of the high-redshift TF relation has not been explored with large numbers of galaxies. We will now explore the low mass TF relation at $z \sim 2$ with SIGMA galaxies.

3.5.2 TF Relation for SIGMA

In the top panel of Figure 3.5 we plot the stellar mass Tully-Fisher relation for the galaxies in SIGMA. The points are color coded to indicate the ratio of ordered (V_{rot})

to disordered (σ_g) motions in each galaxy, which we will refer to as "kinematic order". Only one PA, the PA with the strongest velocity gradient, is shown for each galaxy. As described in §4.1, we do not apply an inclination correction for the 4 galaxies whose largest velocity gradients are measured at a Δ PA $> 45°$. A few galaxies have a best-fit rotation velocity which is below the nominal resolution limit of our spectra, shown by the dashed line. We set these galaxies at an upper limit of $V_{rot} \times \sin i <$ 15 km s^{-1} in subsequent figures.

The most massive galaxies in SIGMA ($\log M_*/M_\odot \gtrsim 10.2$) lie on or above the TF ridge line, which we define using the local relation from Reyes et al. 2011. These galaxies exhibit values of $V_{rot}/\sigma_g \sim 2-8$, factors of a few lower than local galaxies at the same mass. We perform a simple linear regression to the stellar mass TF relation for these 12 massive ($\log M_*/M_\odot \gtrsim 10.2$) rotationally-supported galaxies ($V_{rot}/\sigma_g >$ 1). We fix the slope to the value from local relation and report an offset to lower M_* of 0.44 ± 0.16 *dex*. If these systems are gas-rich, then the baryonic (M_*+M_{gas}) TF relation is the more applicable scaling relation. Although measurements of gas mass are unavailable for the galaxies in our sample, we note that an offset in mass of 0.44 *dex* implies that we may be missing $\sim$ 60% of the baryonic mass. This is consistent with estimates of the molecular gas reservoirs in massive galaxies at high redshift (e.g., Tacconi et al. 2013). As SIGMA includes both rotationally-supported and dispersion-dominated galaxies, we make no further attempt to characterize an evolution in the slope, scatter or intercept of the stellar mass TF relation for disks, which would

require morphological pruning. At low stellar stellar mass ($\log M_*/M_\odot < 10.2$) we find significant scatter from the ridge line to low rotation velocity. A large fraction of these galaxies show marginal rotation support, with values of $V_{rot}/\sigma_g \lesssim 1$.

In the middle panel of Figure 3.5 we show the velocity dispersion as a function of stellar mass. As discussed in §3, the velocity dispersion that we measure is corrected for seeing and modeled as a constant term across the galaxy. Due to the finite width of the slit ($0.7''$) and the effects of seeing ($\sim 0.6''$), σ_g is an integration of small scale velocity gradients, thermal broadening and internal turbulence. The velocity dispersion is only mildly correlated with stellar mass, with more massive galaxies displaying marginally higher velocity dispersions. The mean and rms scatter of σ_g for the low mass ($9 < \log M_*/M_\odot < 10$) and high mass ($10 < \log M_*/M_\odot < 11$) samples are 57 ± 19 km s^{-1} and 64 ± 29 km s^{-1}, respectively. The galaxies which fall from the TF ridgeline to low V_{rot} display characteristically higher σ_g at fixed stellar mass. In other words, the lower V_{rot}/σ_g in these galaxies is due to both lower rotation velocity and higher velocity dispersion.

Star-forming galaxies at z $\sim$ 2 tend to have much stronger kinematic contributions from σ_g than their local counterparts. For the bulk of our sample there appears to be a floor in velocity dispersion of $\sigma_g = 30$ km s^{-1}. This floor is slightly higher than the typical gas velocity dispersion in local disk galaxies, $\sim$ 25 km s^{-1} (Epinat et al., 2010), and higher than the spectral resolution limit of our observations, ~ 20 km s^{-1}.

To combine the quantities V_{rot} and σ_g into a more fundamental quantity, many

authors (e.g., Weiner et al. 2006b; Kassin et al. 2007; Vergani et al. 2012) adopt a joint kinematic parameter, $S_K = \sqrt{K\,V_{rot}^2 + \sigma_g^2}$ (Weiner et al., 2006b). A common choice is made for $K = 0.5$, motivated by virial arguments for a spherically symmetric tracer distribution (see Weiner et al. 2006a). The $S_{0.5}$ quantity more reliably traces the overall potential of a galaxy system, independent of morphology, recent disturbance or kinematic state (Kassin et al., 2007; Covington et al., 2010). In the bottom panel of Figure 3.5 we show the $M_* - S_{0.5}$ relation for our sample, which re-establishes the TF relation for all galaxies. This has been found previously at $z \sim 2$ (Cresci et al., 2009; Price et al., 2016). We note that our low mass galaxies are relatively consistent with the $z \sim 0.2$ relation found by Kassin et al. (2007), while the high mass galaxies tend to be offset to higher $S_{0.5}$. Price et al. (2016) report a similar offset in the $z \sim 2$ $S_{0.5}$ relation over their full mass range ($9 \lesssim \log M_*/M_\odot \lesssim 11$). Rodríguez-Puebla et al. (2016) have argued that it is necessary for the $M_* - S_{0.5}$ to evolve to higher $S_{0.5}$ at fixed mass in order to correctly predict the cosmic stellar mass density. As discussed before, this offset might reflect a rise in M_{gas}/M_{baryon} at higher redshift.

We perform a least-squares linear fit to the $S_{0.5}$ TF relation, $\log S_{0.5}$ (km s^{-1}) $= \alpha\,(\log M_*/M_\odot - 10) + \beta$, for the full sample. We report coefficients of $\alpha = 0.25 \pm 0.06$ and $\beta = 2.00 \pm 0.03$ with an rms scatter $\sigma_{rms} = 0.19$. Even with the apparent dichotomy between the low mass and high mass regions noted above, we find that the slope, amplitude and scatter of the full sample is relatively consistent with the $z \sim 0.2$ relation ($\alpha = 0.30$, $\beta = 1.93$, $\sigma_{rms} = 0.14$) found in Kassin et al. (2007) and

the local Faber-Jackson relation ($\alpha = 0.286$, $\beta = 1.965$)(Gallazzi et al., 2006).

3.6 Kinematic Order vs star-formation rate, size and mass

As discussed in §5, the low mass galaxies in our sample show the strongest residuals from the TF ridge line and the lowest values of V_{rot}/σ_g. In the settling of disk galaxies, massive galaxies are expected to form ordered disks first, followed later by lower mass galaxies ("kinematic downsizing"; Kassin et al. 2012). To probe the drivers of kinematic disturbance at $z \sim 2$, we examine the relation between the kinematic order of SIGMA galaxies (V_{rot}/σ_g) and three of their physical properties: star-formation rate, effective radius and stellar mass. To separate out the dependance of size and SFR on stellar mass, we examine deviations from the size-mass and SFR-mass relations at $z \sim 2$. We find that, at fixed stellar mass, V_{rot}/σ_g is only weakly correlated with SFR and mildly correlated with half-light radius. The strongest correlation is found to be with stellar mass, wherein more massive galaxies tend to be the most rotationally supported. We describe these relations in more detail below.

We perform a ranked spearman correlation test to quantify the association in each relation. The spearman coefficient (r_s) measures the strength of a correlation and we use the common interpretation: $|r_s| < 0.15$ (very weak correlation), $0.15 < |r_s| < 0.30$ (weak/moderate correlation), $0.30 < |r_s| < 0.50$ (moderate/strong correlation).

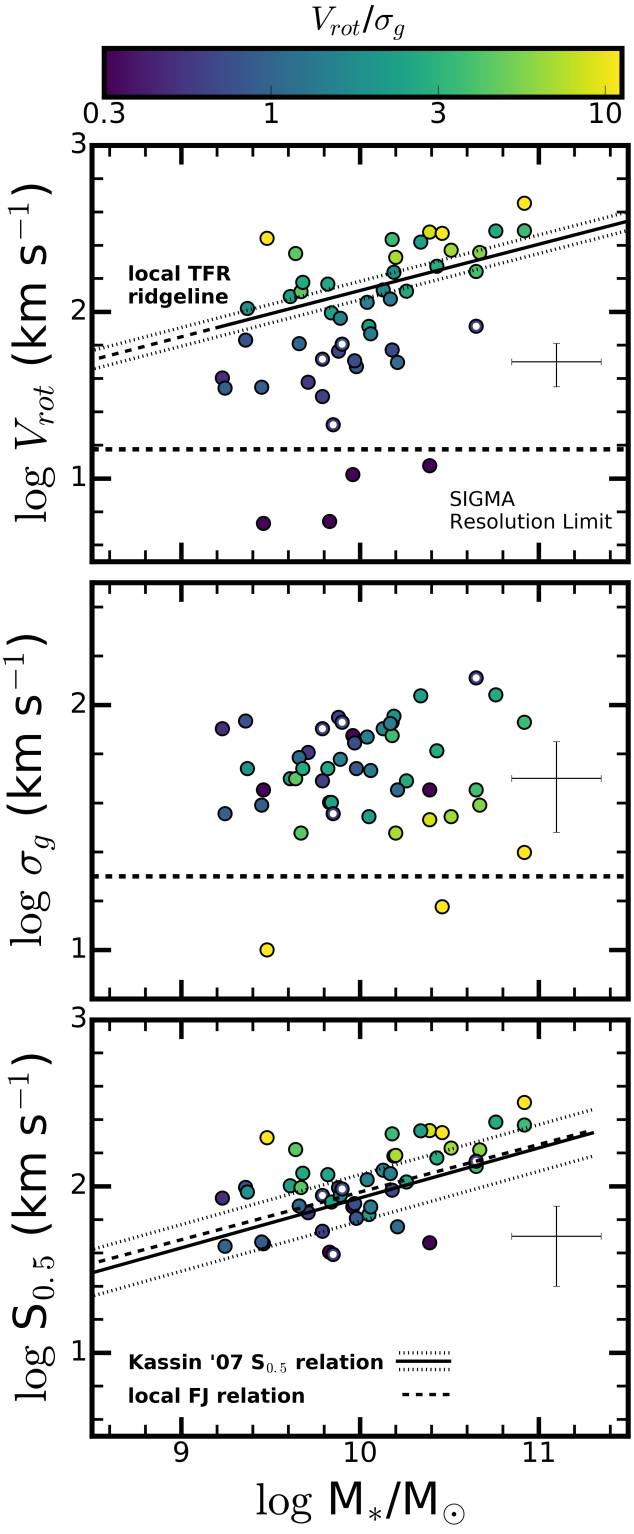

Figure 3.5: Caption on next page.

Figure 3.5: Top: The Tully-Fisher (TF) relation for SIGMA shows significant scatter to low V_{rot} from the local TF ridge line, defined by Reyes et al. 2011. The largest scatter is found at low stellar mass ($\log M_*/M_\odot \lesssim 10.2$). Middle: The relation between gas velocity dispersion (σ_g) and M_* is shown. The slowly rotating galaxies that fall from the TF relation have elevated velocity dispersions. Bottom: The $S_{0.5}$ TF relation is shown along with the fit and scatter from the $z \sim 0.2$ DEEP2 sample (Kassin et al., 2007) and the local Faber-Jackson relation, defined by Gallazzi et al. 2006. The handful of galaxies in which the largest velocity gradient was measured in an off-axis slit are not inclination corrected and are shown as open circles. The resolution limits for measuring rotation and dispersion in SIGMA is given by the horizontal dashed lines in the top and middle plots.

The p-value (p) indicates the probability of uncorrelated data producing a spearman coefficient at least as extreme as the value given.

In the left panel of Figure 3.6 we examine the correlation of V_{rot}/σ_g with stellar mass following K12 for $z < 1.2$. We note that the trend is the strongest of the three we investigate, with an increasing trend of V_{rot}/σ_g with stellar mass and a spearman coefficient, $r_s = 0.39$ ($p = 0.01$). If we only include the galaxies with detected rotation and inclination corrections (i.e., filled circles), the trend with stellar mass strengthens to $r_s = 0.48$ ($p < 10^{-2}$).

Next, we examine the departure of our galaxies from the size-mass relation at $z \sim 2$, as parameterized for late type galaxies in Table 1 of van der Wel et al. 2014a. We use the $z \sim 1.75$ and $z \sim 2.25$ size-mass relations for our low and high redshift bins, respectively. The half-light size used for these relations is calibrated to

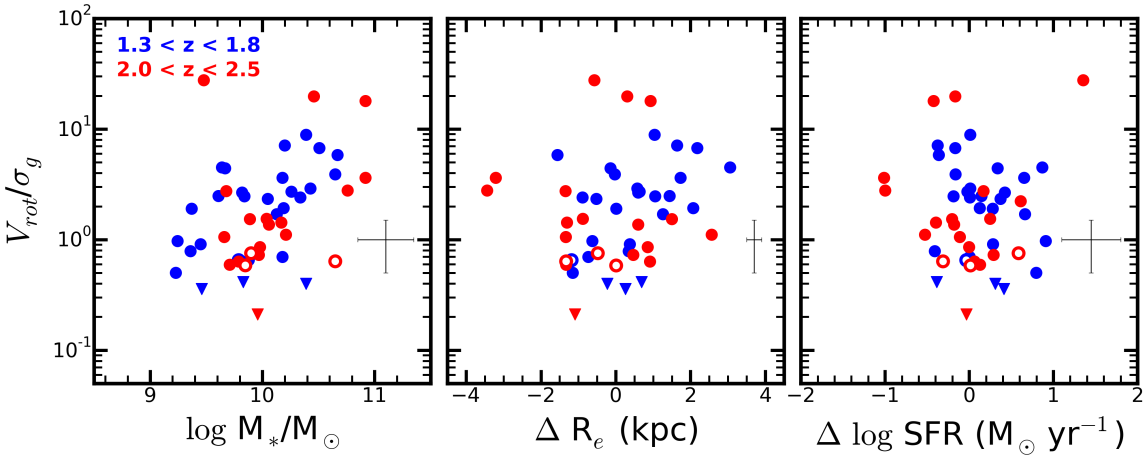

Figure 3.6: The kinematic order (V_{rot}/σ_g) of SIGMA galaxies is strongly correlated with stellar mass (M_*; left panel), moderately correlated with H-band continuum size at fixed a stellar mass ($\Delta\, R_e$; middle panel) and weakly correlated with with star-formation rate at fixed stellar mass (Δ log SFR; right panel). In the 3 panels we show V_{rot}/σ_g versus M_*, residuals from the $z \sim 2$ SFR-M_* relation and residuals from the $z \sim 1.75$ and $z \sim 2.25$ size-mass relations. The blue and red points represent our low and high redshift subsamples, respectively. Typical error bars for each quantity are shown in each plot. Galaxies with measured values of V_{rot} below the spectral resolution limit are set to the resolution limit and are shown as upper-limit symbols (upside-down triangles).

rest-frame 5000 Å (1.5 μm at z=2) and so we adopt the H-band half-light radii for comparison. In the middle panel of Figure 3.6, we present the differences between the half-light radii of our galaxies and the size-mass relation (Δ R$_e$ = R$_{e,gal}$ - R$_{e,seq}$.). The intrinsic scatter of the relation is 0.18 and 0.19 dex for both the low and high redshift bins, respectively, consistent with the rms scatter in our sample of 0.19. We note that there is a weak/mild correlation between V_{rot}/σ_g and Δ R$_e$, as quantified by the spearman coefficient $r_s = 0.23$ ($p = 0.10$).

Finally, in the right panel of Figure 3.6, we examine the correlation of kinematic order with a galaxy's departure from the $1.5 < z < 2.6$ star-formation main sequence (M_*-SFR). If the dispersion-dominated galaxies are being disrupted by internal processes associated with star-formation, we would expect a correlation between V_{rot}/σ_g and the position of a galaxy on the star-formation main sequence. We adopt the main sequence fit of Reddy et al. (2012) as parameterized in Speagle et al. (2014) and adjust to a Chabrier IMF to match with our sample. This relation is valid over $\log M_*/M_\odot = 8.7 - 11.1$, spanning our full mass interval. We find no strong trend with Δ log SFR (defined as log SFR$_{gal}$ - log SFR$_{seq}$) and V_{rot}/σ_g. In other words, at fixed stellar mass the position of a galaxy above or below the star-formation main sequence is not related to its internal gas kinematics. The spearman coefficient between these two values confirms the lack of a trend, $r_s = -0.09$ (with $p = 0.54$).

Combining kinematic measurements at $z \sim 2$ from both the KMOS-3D (Wisnioski et al., 2015) and MOSDEF surveys (Kriek et al., 2015), Price et al. 2016 investigated

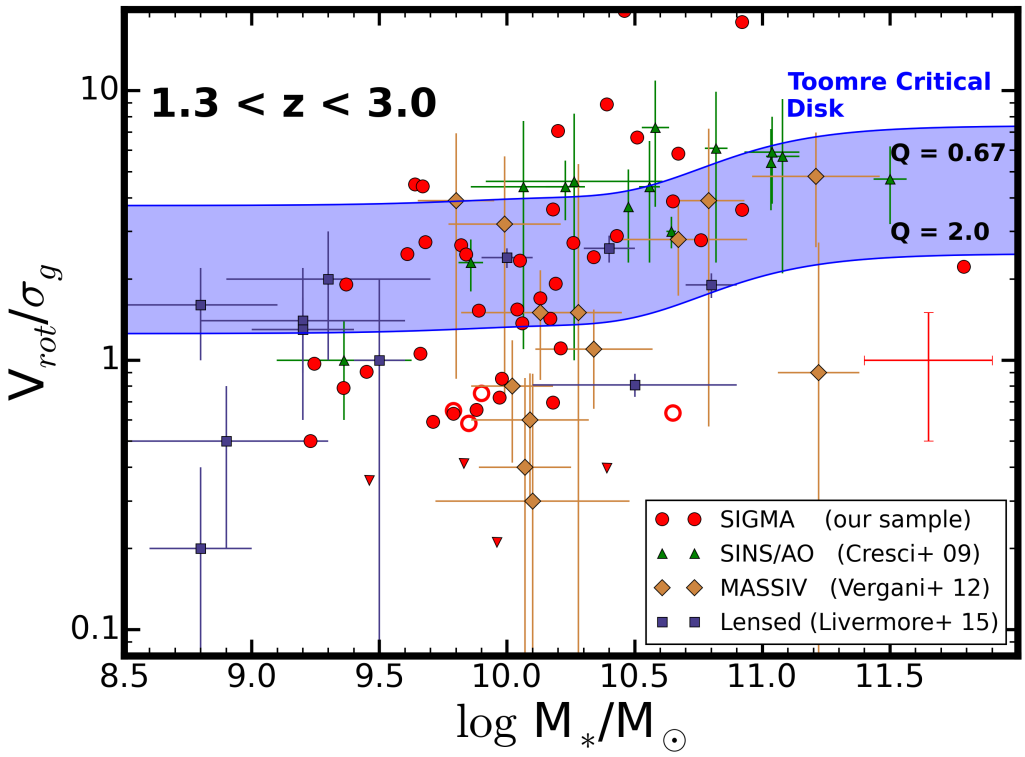

Figure 3.7: Kinematic order (V_{rot}/σ_g) versus stellar mass for galaxies in SIGMA and from the literature. A model for a marginally stable disk galaxy at $z \sim 2$ is shown as a blue shaded swath. While high mass galaxies fall within this swath, a large fraction of the low mass galaxies fall below it. High mass galaxies at $z \sim 2$ are consistent with the model, implying that they have already formed primitive disks. In contrast, a large fraction of the low mass galaxies are dispersion dominated ($V_{rot}/\sigma_g < 1$) and are still in the process of assembling their disks. We note that the high mass disks are unlike the majority of local disk galaxies at a similar stellar mass, which typically have values of V_{rot}/σ_g of around 10-15.

the trend of V/σ_g with specific star formation rate ($sSFR = SFR/M_*$) and stellar mass, finding a declining and weakly increasing trend respectively. We find that, when we fix for stellar mass, there is no dependance on SFR. Instead, the strongest correlation in the SIGMA sample is with stellar mass alone. If we consider that the gas mass scales with SFR (Kennicutt, 1998b; Daddi et al., 2010a), these results would indicate that the kinematic order of a galaxy is more strongly linked with its mass than its gas fraction.

3.7 A Test for Stable Disks

In this section we compare our measurements of V_{rot}/σ_g with a model for gas rich marginally stable disks using the refined Toomre analysis given in Genzel et al. (2011). We find that high mass galaxies in our sample are in general agreement with this model, indicating that they have already assembled primitive disks.

3.7.1 Model for a stable disk

Galaxies which have already settled to become disks by $z \sim 2$ are gas rich (e.g., Daddi et al. 2010b; Tacconi et al. 2013) and are expected to be in a marginally stable (to collapse) equilibrium (e.g., Genzel et al. 2008), regulated by ubiquitous inflows, outflows and star-formation (Bouché et al., 2010; Davé et al., 2012). This regulator model successfully describes the elevated velocity dispersions in high redshift gas-

rich disks (Wisnioski et al., 2015). Following the work of Genzel et al. (2011) and Wisnioski et al. (2015), V_{rot}/σ_g of the ionized gas in a marginally stable disk can be estimated from the Toomre criterion:

$$\frac{V_{rot}}{\sigma_g} = \left(\frac{a}{Q_{crit}}\right)\left(\frac{1}{f_{gas}}\right) \tag{3.2}$$

where a is a constant which is set to $\sqrt{2}$ for a flat rotation curve, as discussed in Dekel et al. (2009). The quantity Q_{crit} is the critical Toomre parameter which, considering the range of realistic disks, can vary between 0.67 (single-component thick disk; Genzel et al. 2011) and 2.0 (two-component thin disk; Ceverino et al. 2010). The gas fraction (f_{gas}) can be estimated from the gas depletion timescale ($t_{depl} = M_{mol,gas}/SFR$) and the specific star-formation rate ($sSFR$) as $1/f_{gas} = 1 + (t_{depl} \times sSFR)^{-1}$. The gas depletion timescale is relatively constant with stellar mass at $z \sim 2$ and we fix it to $t_{depl} = 7 \times 10^8$ yr (Tacconi et al. 2013; Genzel et al. 2015). For our analysis we adopt the sSFR - M_* relation at z = 2 from Whitaker et al. (2014) using the fit in Wisnioski et al. (2015). Equation 2 is derived assuming that the gravitational force exerted by M_{dyn} is supported by rotation, which is not generally true for our dispersion dominated systems. This stability analysis would not directly apply to these galaxies, but we can still compare V_{rot}/σ_g in these systems with our disk model.

3.7.2 Applying the model to data

In Figure 3.7 we show V_{rot}/σ_g as a function of stellar mass for the galaxies in our sample and additional publicly available measurements for the following surveys: SINS (Cresci et al., 2009), MASSIV (Vergani et al., 2012), and lensed galaxies from Livermore et al. (2015) and Jones et al. (2010). The SINS sample is the high signal-to-noise adaptive optics assisted subset and is representative of the most massive and star-forming galaxies at $z \sim 2$. The lensed sample and MASSIV sample are more generally representative of star-forming galaxies at these epochs. We use these samples to extend our mass baseline to $\log M_*/M_\odot = 8 - 11.5$ and to illustrate the consistency of our measurements with those in the literature.

The expected distribution of V_{rot}/σ_g for marginally stable disks at $z \sim 2$ is shown in Figure 3.7 and follows from the model described above. This range includes a characteristic break above $\log M_*/M_\odot \approx 10.2$, due to a kink in the $z \sim 2$ stellar mass sSFR relation.

We find that high mass galaxies ($\log M_*/M_\odot > 10.2$) are in general agreement with the marginally stable disk model, i.e., high mass galaxies have already assembled their disks by $z \sim 2$. In general these disks are expected to contain large gas reservoirs which drive violent disk instabilities and maintain elevated velocity dispersions. These galaxies are unlike local disks of the same mass, which have values of $V_{rot}/\sigma_g \sim 10-15$ as opposed to $V_{rot}/\sigma_g \sim 2-8$. As their gas reservoirs deplete, they are expected to stabilize and form well-ordered disks (Wisnioski et al., 2015).

Below a stellar mass of log $M_*/M_\odot \approx 10.2$ we find the common occurrence of systems which are dispersion dominated and/or marginally rotationally supported ($V_{rot}/\sigma_g \lesssim 1$). For comparison, the most dispersion dominated system expected from the disk model is $V_{rot}/\sigma_g = 0.7$ ($f_{gas} = 1$, $Q_{crit} = 2$ in Eq 2). Galaxies with lower V_{rot}/σ_g would be considered globally stable to gas collapse ($Q > Q_{crit}$), even as they are obviously forming stars. Although gas-rich disks with high velocity dispersion are expected at $z \sim 2$, a large fraction of our low mass sample cannot be described by this simple model for marginally stable disks.

3.8 Conclusions

We present the first results of SIGMA (Survey in the near-Infrared of Galaxies with Multiple position Angles), a kinematic survey of 49 star-forming galaxies over $1.3 < z < 3.0$ in three of the CANDELS fields. SIGMA is representative of the $z \sim 2$ star-formation main sequence to log $M_*/M_\odot = 9.2$ at $z \sim 1.6$ and log $M_*/M_\odot = 9.6$ at $z \sim 2.3$, and includes galaxies with both disk and irregular morphologies. Internal kinematics (rotation velocity V_{rot} and gas velocity dispersion σ_g) are measured from resolved rest-optical nebular emission lines (Hα, [O III]λ 5007) in Keck/MOSFIRE NIR spectra.

We find that high mass galaxies (log $M_*/M_\odot > 10.2$) at $z \sim 2$ are generally rotationally supported, fall on the TF relation, and have formed primitive disks with

high σ_g. These marginally stable disks are expected to decline in σ_g with time as they deplete their gas supply (Wisnioski et al., 2015). In contrast, a large fraction of low mass galaxies ($\log M_*/M_\odot < 10.2$) at this epoch are in the early phases of assembling their disks. They have much lower "kinematic order" ($V_{rot} \lesssim \sigma_g$) and tend to fall to low V_{rot} from the Tully-Fisher relation. For perspective, these results imply that a Milky-Way progenitor at $z \sim 2$ ($\log M_*/M_\odot \approx 9.8$; Papovich et al. 2015) is likely still in the process of forming a disk. Combining both V_{rot} and σ_g in $S_{0.5}$, all of the galaxies in SIGMA fall on the $S_{0.5}$ Tully-Fisher relation, indicating that many galaxies at low mass have strong contributions of kinematic support in the form of σ_g. Following Kassin et al. (2012) at $z < 1$, the tendency for high mass galaxies to develop disks first is referred to as "kinematic downsizing", and these results imply that it is in place at $z \sim 2$.

To gain insight into the underlying drivers of kinematic disruption, we explore the dependance of V_{rot}/σ_g on three physical parameters of galaxies: size, star-formation rate and stellar mass. We find that the strongest trend is with stellar mass, wherein high mass galaxies have the strongest rotational support (i.e., highest values of V_{rot}/σ_g). We examine the relation between V_{rot}/σ_g and residuals from the star-formation main sequence and we find no correlation, to within the uncertainties of our measurements. Given that the star-formation rate is likely tracing the available gas mass (Daddi et al., 2010a), our results imply that mass may be more fundamental than gas fraction in determining kinematic order. Finally, we find a moderate correla-

tion between V_{rot}/σ_g and size, likely associated with the increased angular momentum of the rotationally supported systems. The strong trend between V_{rot}/σ_g and mass and the lack of a correlation with SFR at fixed mass implies that the processes that maintain σ_g in galaxies should be most efficient at low stellar mass and should be independent on gas fraction.

Several processes which disrupt disk galaxies are active at $z \sim 2$, associated with elevated star-formation (Madau & Dickinson, 2014) and rising merger rates (Rodriguez-Gomez et al., 2015). Several of these mechanisms may play a role in preferentially stalling disk formation in low mass galaxies. Feedback through stellar winds and supernovae can effectively blow out gas and dynamically heat stars in low mass dwarf galaxies ($\lesssim 10^{9.5}\,M_{\odot}$; e.g, Wheeler et al. 2017; El-Badry et al. 2016). We note that we find no trend between V_{rot}/σ_g and SFR at fixed mass among the galaxies studied in this sample ($9.2 < \log M_*/M_{\odot} < 11$), indicating that such feedback mechanisms may only assume a secondary role in disturbing the gas kinematics in these galaxies. Mergers play a complicated role in shaping the angular momentum content of disk galaxies. Models (e.g., Governato et al. 2009; Hopkins et al. 2009) and observations (e.g., Hammer et al. 2005, 2009) indicate that gas-rich disks can survive major mergers, albeit with thick disks and perturbed kinematics. Examining mock observations from a suite of simulated galaxy mergers, Covington et al. (2010) find that merger remnants tend to scatter to low V_{rot} from the TFR, similar to the low mass galaxies in our sample. Although several channels exist for stalling (and

promoting) disk formation, it is as of yet unclear what the dominate processes are in maintaining the elevated kinematic disturbance we observe in low mass galaxies at this epoch.

In summary, we find that kinematic downsizing is active as far back in time as $z \sim 2$. While massive star-forming galaxies ($\log M_* > 10.2$) appear to have assembled primitive rotating disks by this time (consistent with e.g., Genzel et al. 2006; Förster Schreiber et al. 2006; Genzel et al. 2008; Shapiro et al. 2008; Förster Schreiber et al. 2009; Swinbank et al. 2011; Law et al. 2012; Buitrago et al. 2014; Wisnioski et al. 2015; Price et al. 2016), low mass galaxies tend to be more kinematically disordered and still in the early process of assembling their disks. The peak of cosmic star-formation is coincident with the epoch of disk assembly for low mass galaxies and the settling of primitive disks in high mass galaxies.

3.9 Appendix: Modeling the effects of size

In this Appendix, we perform mock observations of simulated SIGMA spectra in order to determine the limiting spatial scale from which we can recover rotation velocity, if present, in our observations. We find that we can recover kinematics down to a limit of $\mathrm{D}_{50}/\mathrm{Seeing}_{FWHM} = 0.8$. In §2, we apply this limit to our data set.

The spectra presented in this chapter were observed in seeing limited conditions, and as such the effects of beam smearing (Begeman, 1987) are important to un-

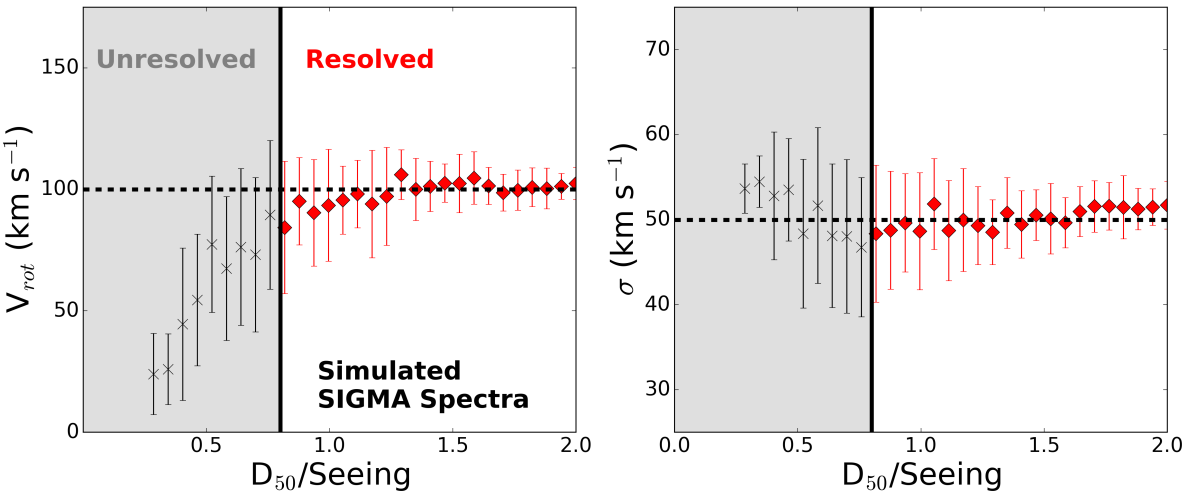

Figure 3.8: Our models demonstrate that galaxy kinematics in SIGMA can be measured down to a size of $D_{50} = 0.8 \times Seeing_{FWHM}$, where D_{50} is the intrinsic half-light diameter and $Seeing_{FWHM}$ is the full width at half maximum of the seeing during the observations. These plots show mock observations of a model galaxy at varying intrinsic sizes, the points show the mean and rms scatter from 100 realizations at each size interval. The model is a rotation dominated galaxy with $V_{rot} = 100$ km s^{-1} and $\sigma_g = 50$ km s^{-1}, marked by the dashed line, and the emission line profile is a Sersic with an index of $n = 2$. The correct values of V_{rot} (left panel) and σ_g (right panel) are recovered (red circles) for mock observations with intrinsic sizes $D_{50} > 0.8 \times Seeing_{FWHM}$. We find a systematic drop in V_{rot} for models that have sizes smaller than this value and are unresolved (black x's).

derstand. Seeing tends to blur together spatially distinct velocities, leading to a decreased rotation signature and an elevated velocity dispersion. To explore the effective resolution set by beam smearing in SIGMA, we create a set of model spectra with various sizes and fixed kinematic parameters. As described below, we perform mock observations of the kinematics for these spectra and explore how the results vary with size. Our model for a single mock SIGMA/MOSFIRE spectrum consists of first creating a 1D emission line with a Sersic intensity profile:

$$\Sigma(r) = \Sigma_e e^{-k[(r/R_e)^{1/n}-1]} \tag{3.3}$$

where R_e is the half-light radius, Σ_e is the intensity at the half-light radius, n is the sersic index and k is a numerical constant that depends on n ($k = 2n - 0.3271$). We set $n = 1.8$, characteristic of the emission line intensity profile for galaxies at this redshift (Nelson et al., 2016). We then draw from an appropriate error spectrum to set the central signal-to-noise per pixel to 15, typical of SIGMA spectra. The final integrated S/N of these simulated spectra are well-matched to our sample. Next, we apply an arctan velocity profile (see Eq 1) and a constant velocity dispersion to the emission line. We fix the rotation velocity to 100 km s^{-1} and the velocity dispersion to 50 km s^{-1}, characteristic of $z \sim 2$ disk galaxies. We then apply a seeing kernel of 0.7" in the spatial direction and MOSFIRE instrumental broadening ($\sigma_{inst} = 40$ km s^{-1}) in the spectral direction. Following the seeing convolution, the emission profile is well described by a gaussian ($n = 0.5$). We repeat this process 100 times, redrawing

from the error spectrum each time to create independent realizations with the same fixed parameters. We then vary the effective radius of the emission line from 0.1 - 0.7 $''$ in 30 even steps of 0.02$''$/step. At each step we again simulate 100 realizations with the same fixed properties. The final dataset contains 3000 simulated SIGMA spectra.

To measure the kinematics from the mock spectra, we run the same fitting technique used for our observations (`ROTCURVE`). For each spatial scale modeled, we measure 100 values of V_{rot} and σ_g and examine their mean and variance. The results of this study are shown in Figure 3.8. The rotation velocity is well recovered with an intrinsic error of $\sim$ 15 km s^{-1}. For simulated spectra with effective diameter at or greater than the seeing, we accurately recover the input rotation and dispersion. Below a value of $D_{50}/\mathrm{Seeing}_{FWHM} = 0.8$, the limiting spatial resolution drastically affects the recovered values of V_{rot} and σ_g. There is both a larger uncertainty in the measurements and a systematic decline in the measured rotation velocity. Based on the results of these models, we determine that the spatial scale for recovering kinematics in our observations is diameter $D_{50} > 0.8 \times \mathrm{Seeing}_{FWHM}$. Above this value we can reliably recover rotational motion, if present.

Table 3.1: SIGMA - Observational and Physical Properties

Observational measurements and derived physical properties for the SIGMA galaxy sample. The galaxy ID, RA (J2000) and DEC (J2000) are matched with the publicly available CANDELS catalogs in Galametz et al. (2013); Guo et al. (2013). The H-band magnitude (m_H) and axis ratio (b/a) are adopted from the GALFIT measurements on the HST/WFC3 F160W CANDELS image in van der Wel et al. (2012). The stellar mass (M_*) and star-formation rate (SFR) are derived from the full galaxy SED, as described in §3.2.

ID	RA (J2000)	DEC (J2000)	z_{spec}	m_H (AB)	$\log M_* (M_\odot)$	$\log SFR\,(M_\odot\, yr^{-1})$	$(b/a)_H$
5492	03 32 41.78	−27 51 35.28	1.67	22.51	10.39	1.95	0.57
14602	03 32 14.66	−27 47 02.70	1.73	22.37	10.18	1.44	0.91
16209	03 32 15.82	−27 46 22.36	1.33	23.47	9.36	0.23	0.34
16600	03 32 30.71	−27 46 17.17	1.31	21.20	10.51	1.59	0.70
16905	03 32 15.75	−27 46 04.32	1.54	22.15	10.13	2.05	0.32
17488	03 32 20.18	−27 45 49.31	1.61	23.16	9.46	1.15	0.41
17673	03 32 33.86	−27 45 42.65	1.62	22.69	10.05	1.68	0.85
18177	03 32 12.48	−27 45 30.42	1.38	22.03	10.19	1.57	0.41
19818	03 32 18.07	−27 44 33.44	1.38	22.43	9.23	1.31	0.81
20495	03 32 11.86	−27 44 13.38	1.33	21.30	10.43	1.69	0.78
20569	03 32 29.19	−27 44 13.21	1.47	23.89	9.24	1.44	0.49
20593	03 32 12.77	−27 44 07.77	1.61	23.13	10.26	1.49	0.29
20883	03 32 26.77	−27 43 58.22	1.61	23.43	9.88	1.14	0.51
21007	03 32 31.83	−27 43 56.26	1.55	21.80	10.67	1.55	0.81
21162	03 32 23.95	−27 43 49.09	1.31	22.16	9.79	1.02	0.87
21258	03 32 30.75	−27 43 45.34	1.43	23.17	9.37	0.93	0.33
21737	03 32 30.14	−27 43 35.44	1.60	22.55	10.20	1.08	0.69
21897	03 32 34.08	−27 43 28.43	1.60	22.44	9.82	1.51	0.42
22236	03 32 26.19	−27 43 17.38	1.61	23.09	9.61	1.03	0.49
22354	03 32 13.66	−27 43 13.08	1.47	22.45	9.67	1.28	0.91
22783	03 32 26.30	−27 43 01.89	1.55	23.11	9.83	0.71	0.46
23095	03 32 38.50	−27 42 27.89	1.61	21.93	10.39	1.65	0.76

23632	03 32 28.13	−27 42 48.27	1.61	23.35	9.45	1.01	0.33
25715	03 32 22.72	−27 41 40.74	1.61	22.12	10.34	1.60	0.96
25973	03 32 26.08	−27 41 38.49	1.54	22.74	9.84	0.92	0.62
26050	03 32 13.89	−27 41 58.29	1.32	22.57	9.64	1.78	0.24
26177	03 32 27.28	−27 42 05.20	1.61	21.11	10.65	1.73	0.91
26736	03 32 26.41	−27 42 28.30	1.61	22.21	10.18	2.09	0.49
1826	12 36 18.78	+62 08 39.70	2.30	23.03	9.79	1.12	0.32
2815	12 36 35.56	+62 09 20.33	2.36	23.26	9.71	1.11	0.66
4106	12 36 39.37	+62 10 06.60	2.35	22.40	10.65	1.58	0.31
4476	12 36 13.13	+62 10 21.11	2.24	23.50	9.89	0.95	0.27
4714	12 36 36.08	+62 10 29.90	2.31	23.01	10.17	1.03	0.83
4925	12 36 11.51	+62 10 33.72	2.25	22.52	10.92	1.73	0.72
4962	12 36 18.77	+62 10 37.28	2.27	23.56	9.68	1.12	0.59
9157	12 36 13.56	+62 12 21.58	2.44	23.13	9.90	1.75	0.48
9190	12 36 18.27	+62 12 22.18	2.44	23.38	9.85	1.13	0.89
10230	12 37 06.71	+62 12 44.61	2.21	23.23	10.21	0.94	0.17
11525	12 36 26.94	+62 13 17.86	2.40	23.91	9.48	2.11	0.42
13230	12 36 09.05	+62 13 59.03	2.05	24.83	9.96	1.19	0.37
13678	12 36 44.08	+62 14 10.10	2.27	26.53	9.66	0.82	0.41
14428	12 36 35.59	+62 14 24.01	2.02	25.47	11.79	3.61	0.86
15497	12 36 21.74	+62 14 52.85	2.21	26.28	10.06	1.14	0.76
16028	12 36 51.82	+62 15 04.72	2.19	26.38	10.76	1.00	0.76
16260	12 37 00.46	+62 15 08.86	2.33	24.82	10.92	1.14	0.77
10404	02 17 35.93	−05 13 05.20	2.31	22.92	10.04	1.55	0.51
12138	02 17 48.89	−05 12 30.38	2.25	23.26	9.98	1.24	0.28
14004	02 17 30.72	−05 11 56.22	2.39	23.25	10.46	1.54	0.57
14042	02 17 32.78	−05 11 55.93	2.15	22.65	9.97	1.52	0.27

Table 3.2: SIGMA - Observational and Kinematic Properties

The observational parameters and best-fit kinematic properties for the SIGMA galaxy sample. N_{slits} is the number of spectra in the full SIGMA sample. ΔPA is the difference in position angle between the H-band continuum (PA_{phot}) and the Keck/MOSFIRE slit selected for this chapter (i.e., the slit with the maximum rotation signature; PA_{slit}). r_v is the fixed turnover radius of the rotation curve model. $V \times \sin i$ is measured from the flat part of the best-fit rotation curve and V_{rot} is the inclination corrected rotation velocity. σ_g is the best-fit gas velocity dispersion and is assumed constant across the face of the galaxy.

ID	N_{slits}	$PA_{phot}(^\circ)$	$PA_{slit}(^\circ)$	ΔPA	$r_v(''')$	$V \times \sin i$	V_{rot} (km s^{-1})	σ_g (km s^{-1})
5492	1	65.0 ± 0.7	34.5	30.5	0.2	10 ± 30	11 ± 35	45 ± 14
14602	1	−11.7 ± 0.7	19.0	30.7	0.2	25 ± 37	59 ± 87	85 ± 23
16209	2	9.4 ± 1.3	19.0	9.6	0.2	65 ± 28	67 ± 29	86 ± 22
16600	2	7.0 ± 0.2	10.0	3.0	0.2	171 ± 23	234 ± 31	35 ± 35
16905	3	−87.0 ± 0.3	-56.0	31.0	0.4	131 ± 63	135 ± 65	80 ± 24
17488	2	17.4 ± 1.8	19.0	1.6	0.2	5 ± 14	5 ± 15	45 ± 5
17673	1	−2.8 ± 0.6	8.0	10.8	0.2	44 ± 20	81 ± 37	35 ± 15
18177	2	83.1 ± 0.4	56.0	27.1	0.4	161 ± 50	172 ± 53	90 ± 26
19818	2	−86.6 ± 1.4	56.0	37.4	0.3	24 ± 21	40 ± 35	80 ± 13
20495	3	74.1 ± 0.3	56.0	18.1	0.4	120 ± 27	187 ± 42	65 ± 22
20569	1	22.5 ± 1.8	8.0	14.5	0.2	31 ± 27	34 ± 30	36 ± 15
20593	2	34.1 ± 0.9	19.0	15.1	0.4	130 ± 44	133 ± 45	49 ± 26
20883	1	29.8 ± 2.1	8.0	21.8	0.2	51 ± 36	58 ± 41	89 ± 14
21007	5	−59.5 ± 0.4	117.0	3.5	0.2	136 ± 24	227 ± 40	39 ± 40
21162	3	−82.7 ± 0.7	19.0	78.3	0.2	52 ± 19	—	80 ± 6
21258	3	−52.7 ± 1.4	117.0	10.3	0.4	101 ± 78	104 ± 80	55 ± 38
21737	1	−19.6 ± 0.6	8.0	27.6	0.2	157 ± 29	212 ± 39	30 ± 31
21897	2	−24.5 ± 0.7	120.5	35.0	0.2	136 ± 20	146 ± 21	55 ± 17
22236	2	−15.7 ± 1.5	19.0	34.7	0.2	110 ± 32	123 ± 35	50 ± 23
22354	2	36.0 ± 0.7	19.0	17.0	0.2	56 ± 20	132 ± 47	30 ± 20
22783	1	32.1 ± 1.5	10.0	22.1	0.2	5 ± 38	5 ± 41	40 ± 16

23095	2	-70.9 ± 0.5	120.5	11.4	0.2	200 ± 42	301 ± 63	34 ± 36
23632	2	88.3 ± 1.2	78.5	9.8	0.2	34 ± 18	35 ± 18	39 ± 8
25715	1	-39.7 ± 0.9	120.5	19.8	0.2	75 ± 43	262 ± 150	109 ± 23
25973	3	33.0 ± 0.8	19.0	14.0	0.2	79 ± 21	98 ± 26	40 ± 15
26050	1	-53.0 ± 0.6	117.0	10.0	0.3	222 ± 33	224 ± 33	50 ± 24
26177	2	-20.1 ± 0.2	120.5	39.4	0.2	74 ± 18	174 ± 42	45 ± 13
26736	2	-35.2 ± 0.5	-10.0	25.2	0.2	242 ± 35	272 ± 39	75 ± 42
1826	1	-11.7 ± 1.2	32.0	43.7	0.3	30 ± 30	31 ± 31	49 ± 12
2815	2	-12.8 ± 3.4	32.0	44.8	0.3	29 ± 40	37 ± 52	64 ± 12
4106	2	-29.5 ± 0.4	32.0	61.5	0.3	82 ± 64	—	129 ± 25
4476	1	68.0 ± 2.4	106.9	38.9	0.3	90 ± 37	91 ± 37	60 ± 25
4714	1	-47.9 ± 1.2	106.9	25.2	0.3	68 ± 38	119 ± 66	84 ± 30
4925	3	-29.0 ± 1.2	-21.5	7.5	0.2	318 ± 35	448 ± 49	25 ± 61
4962	3	24.9 ± 3.9	32.0	7.1	0.2	124 ± 25	150 ± 30	55 ± 20
9157	3	14.6 ± 0.8	106.9	87.7	0.3	64 ± 22	—	85 ± 15
9190	3	-84.2 ± 1.6	32.0	63.8	0.2	21 ± 28	—	36 ± 18
10230	1	-8.3 ± 7.7	-53.0	44.7	0.3	50 ± 26	50 ± 26	45 ± 20
11525	2	44.7 ± 2.7	32.0	12.7	0.2	256 ± 32	276 ± 34	10 ± 52
13230	1	22.1 ± 18.5	-21.5	43.6	0.3	10 ± 22	10 ± 23	75 ± 7
13678	1	-34.9 ± 0.2	-53.0	18.1	0.3	60 ± 25	64 ± 26	61 ± 8
14428	1	-68.3 ± 5.6	-53.0	15.3	0.2	82 ± 24	157 ± 46	71 ± 14
15497	1	7.9 ± 21.9	32.0	24.1	0.2	49 ± 31	73 ± 46	54 ± 20
16028	1	-71.4 ± 5.8	-53.0	18.4	0.2	203 ± 36	306 ± 54	110 ± 36
16260	1	-63.0 ± 10.3	-53.0	10.0	0.2	200 ± 48	307 ± 73	85 ± 51
10404	1	52.2 ± 1.8	-297.0	10.8	0.2	100 ± 33	114 ± 37	74 ± 14
12138	1	67.3 ± 1.9	-297.0	4.3	0.1	46 ± 17	46 ± 17	55 ± 10
14004	1	40.6 ± 1.3	-297.0	22.4	0.2	248 ± 68	296 ± 81	15 ± 83
14042	1	34.9 ± 0.9	-297.0	28.1	0.3	50 ± 26	50 ± 26	70 ± 8

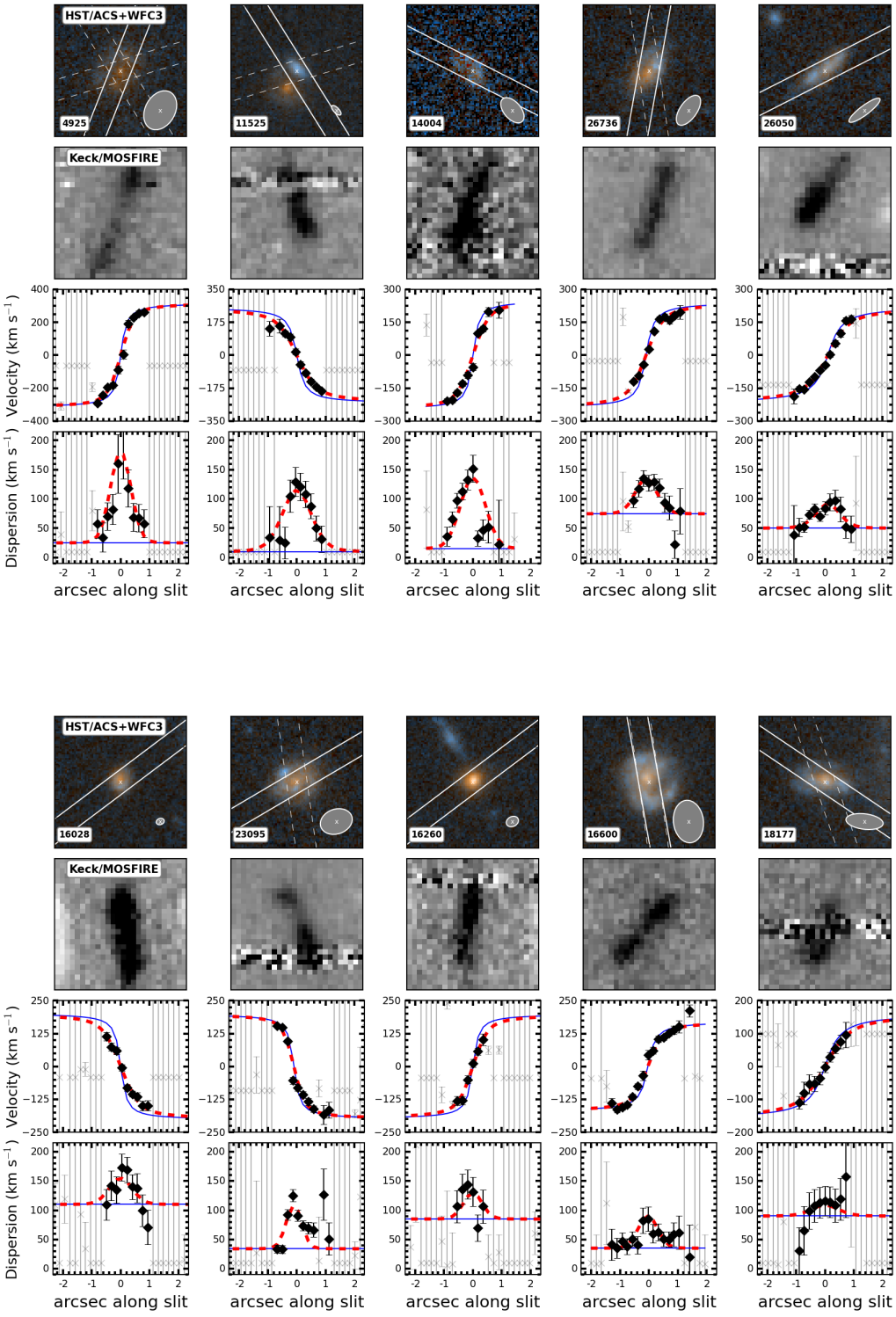

Figure 3.9: Caption on next page.

Figure 3.9: Kinematic fits are presented for the full sample in this chapter. Galaxies are ordered from largest to smallest rotation signature. In the top row, we show the CANDELS I+H-Band HST/ACS-WFC3 color image with the placements of the MOSFIRE slits and the `GALFIT` best-fit half-light ellipse from the H-band image. The solid slit has been adopted for this chapter. The Keck/MOSFIRE spectrum of the solid slit, centered around [O III]λ5007 or Hα, is shown in the second row. The typical seeing FWHM for these observations is $0.6''$. The best-fit velocity and velocity dispersion models are shown as red solid lines and the intrinsic models are shown as blue dashed lines. The black filled diamonds represent the gaussian fits to the velocity and velocity dispersion in each row and the grey points are discarded fits. All of the rows are spatially aligned and each panel is $4.5''$ on a side.

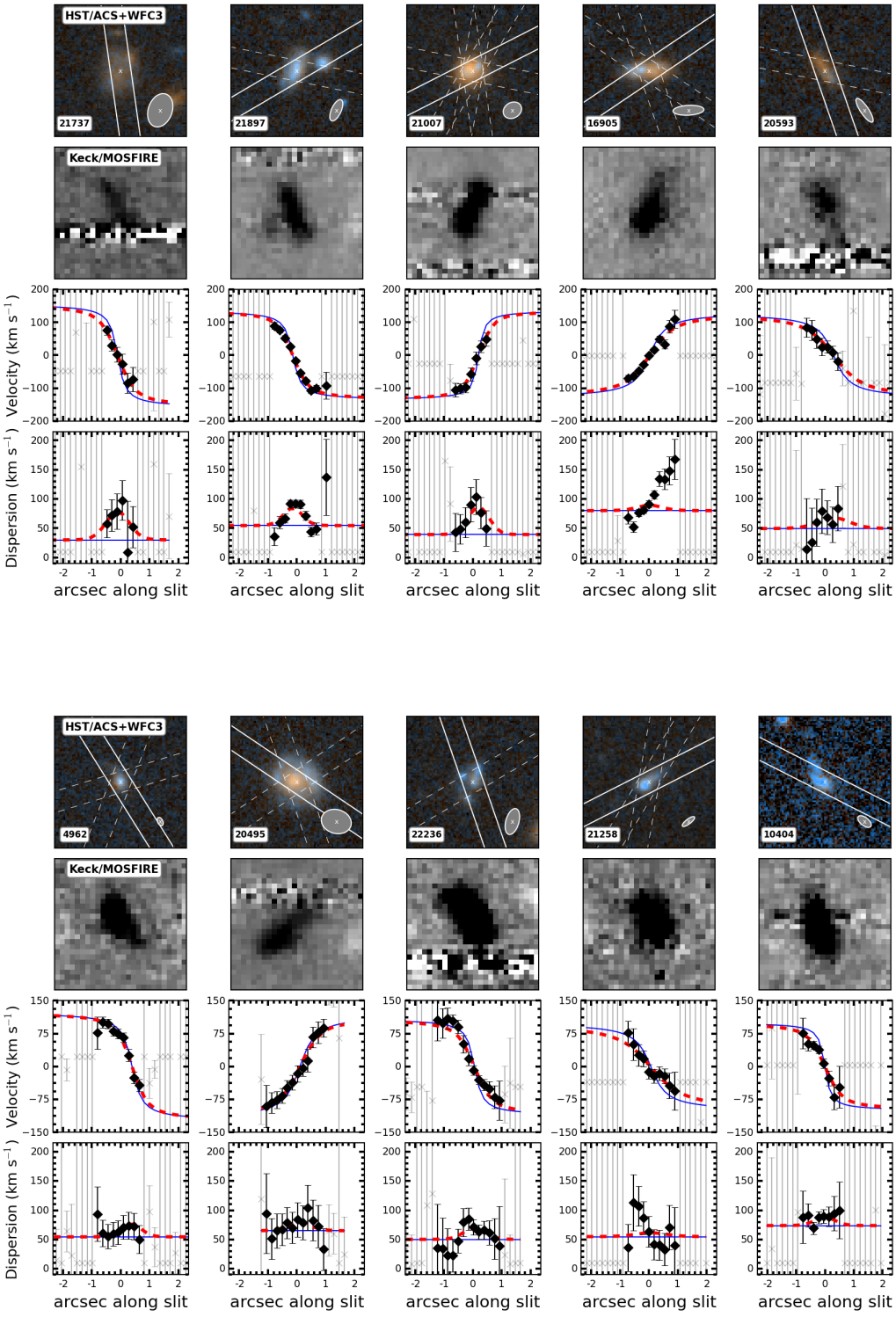

Figure 3.9: Continuation of Figure 3.9.

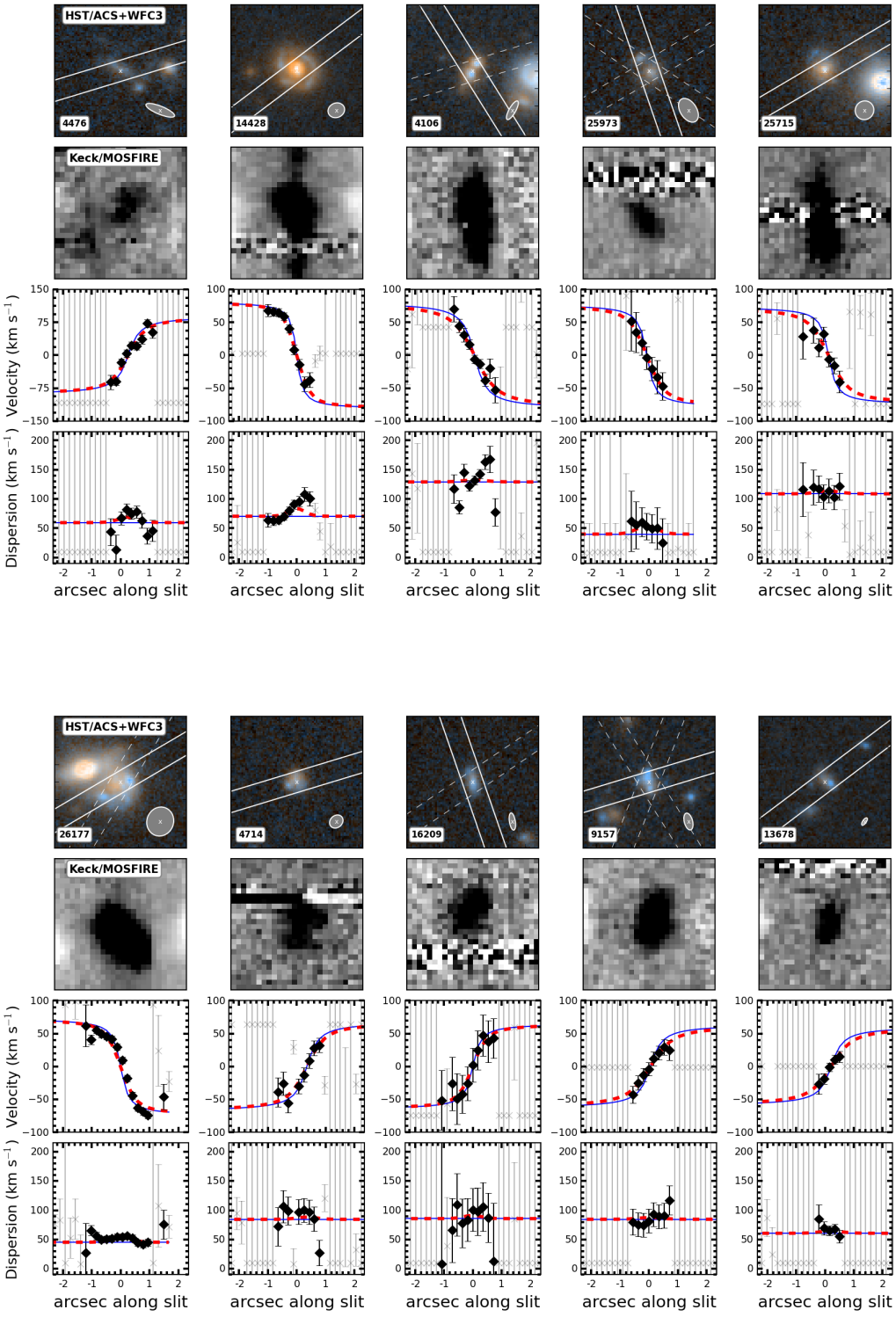

Figure 3.9: Continuation of Figure 3.9.

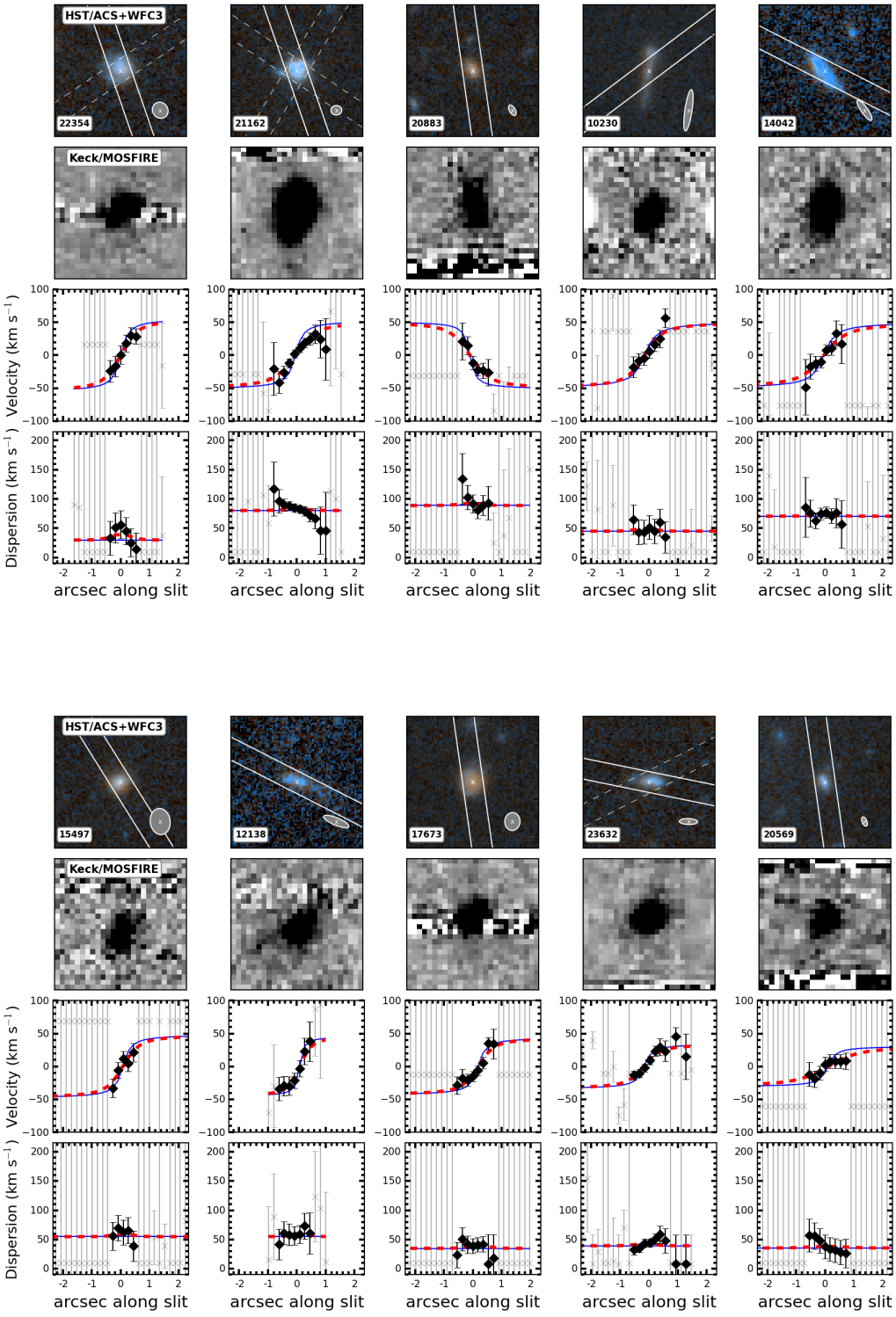

Figure 3.9: Continuation of Figure 3.9.

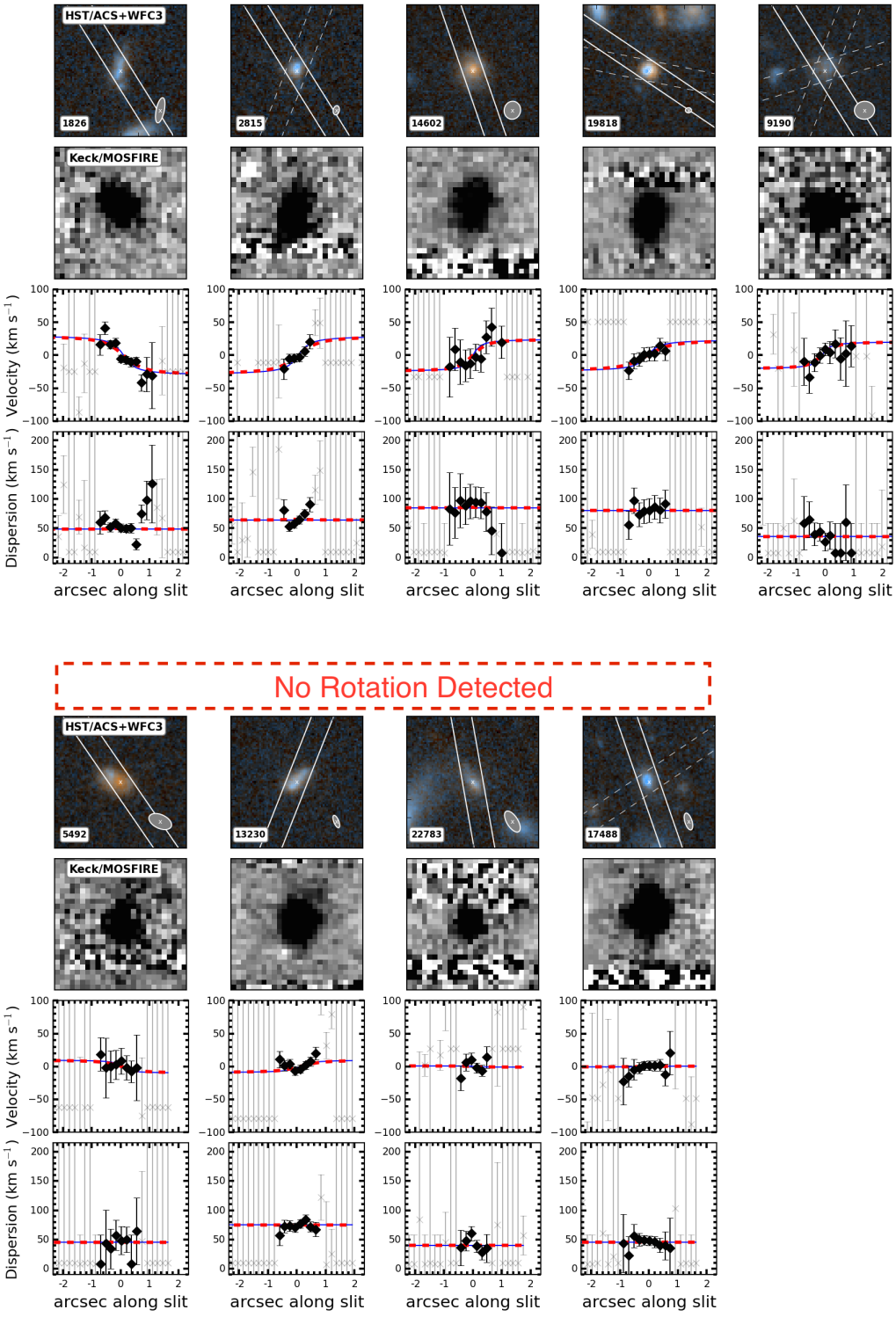

Figure 3.9: Continuation of Figure 3.9.

Chapter 4

$z \sim 2$: An Epoch of Disk Assembly

In this chapter, we explore the evolution of the internal gas kinematics of star-forming galaxies from the peak of cosmic star-formation at $z \sim 2$ to today. Measurements of galaxy rotation velocity V_{rot}, which quantify ordered motions, and gas velocity dispersion σ_g, which quantify disordered motions, are adopted from the DEEP2 and SIGMA surveys. This sample covers a continuous baseline in redshift over $0.1 < z < 2.5$, spanning 10 Gyrs. At low redshift, nearly all sufficiently massive star-forming galaxies are rotationally supported ($V_{rot} > \sigma_g$). By $z = 2$, 50% and 70% of galaxies are rotationally supported at low ($10^9 - 10^{10}\,M_\odot$) and high ($10^{10} - 10^{11} M_\odot$) stellar mass, respectively. For $V_{rot} > 3\,\sigma_g$, the percentage drops below 35% for all masses. From $z = 2$ to now, galaxies exhibit remarkably smooth kinematic evolution on average. All galaxies tend toward rotational support with time, and higher mass systems reach it earlier. This is largely due to a mass-independent decline in σ_g by a

factor of 3 since $z = 2$. Over the same time period, V_{rot} increases by a factor of 1.5 in low mass systems, but does not evolve at high mass. These trends in V_{rot} and σ_g are at a fixed stellar mass and therefore should not be interpreted as evolutionary tracks for galaxy populations. When populations are linked in time via abundance matching, σ_g declines as before and V_{rot} strongly increases with time for all galaxy populations, enhancing the evolution in V_{rot}/σ_g. These results indicate that $z = 2$ is a period of disk assembly, during which strong rotational support is only just beginning to emerge.

4.1 Introduction

The peak of cosmic star-formation at $z \sim 2$ is expected to be a violent period for galaxies. Several active processes, including minor and major mergers, smooth accretion, feedback from star-formation, and violent disk instabilities, can disrupt or stall disk formation. Indeed, observations indicate that the internal kinematics of star-forming galaxies at this time have large amounts of disordered motions (as measured by the velocity dispersion of the gas σ_g) in addition to ordered rotation (V_{rot}) (e.g., Genzel et al. 2006; Förster Schreiber et al. 2006; Law et al. 2007; Wright et al. 2007; Genzel et al. 2008; Shapiro et al. 2008; Law et al. 2009; Förster Schreiber et al. 2009; Jones et al. 2010; Swinbank et al. 2011; Law et al. 2012; Newman et al. 2013b; Glazebrook 2013; Wisnioski et al. 2015; Price et al. 2016; Simons et al. 2016; Mason

et al. 2017; Straatman et al. 2017). Even still, the majority of massive star-forming galaxies, $\log M_*/M_\odot > 10$, at this redshift are rotation-dominated ($V_{rot} > \sigma_g$), with at least 70% showing disk-like kinematic signatures (Wisnioski et al., 2015).

However, these galaxies are unlike local disks. Locally, massive star-forming galaxies have much stronger rotational support ($V_{rot}/\sigma_g \sim 10$) and low values of σ_g (~ 20 km s^{-1}). At a redshift of 2, the quantity V_{rot}/σ_g rarely exceeds a few, indicating that these galaxies mature significantly in the 10 Gyrs between $z = 2$ and now.

The evolution of V_{rot} and σ_g from $z = 1.2$ to now was studied by Kassin et al. (2012) using the DEEP2 survey (Newman et al., 2013a). Over this period, they found that galaxy disks settle with time, increasing in V_{rot}/σ_g by increasing in V_{rot} and declining in σ_g. This evolution is a function of mass, with massive galaxies developing strong rotational support first (i.e., "kinematic downsizing"; Kassin et al. 2012).

Although significant progress has been made in understanding the kinematic state of star-forming galaxies at even higher redshifts, it is unclear how these lower redshift trends from Kassin et al. (2012) relate to the large amounts of disordered motions found in galaxies at $z = 2$. One might not expect a smooth extension to $z = 2$, where the processes governing galaxy assembly are violent and inhospitable to disk formation.

To examine this, or any kinematic evolution, it is important to have a large and homogenous sample. In addition, the sample must have minimal biases, cover the

same galaxy mass range at all redshifts, and ideally have kinematics measured using the same technique. To address these factors, we combine the kinematics samples from the DEEP2 survey (Kassin et al. 2012), which spans $0.1 < z < 1.2$, and the SIGMA survey (Simons et al., 2016), which spans $1.3 < z < 2.5$. These samples have similar selections. They are both morphologically unbiased (i.e., they do not select only disk-like systems) and they trace the star-formation main sequence. Both samples contain enough galaxies to overcome the large intrinsic scatter in galaxy kinematics. Furthermore, measurements were made using the same fitting routine in both surveys. The combined sample covers a large redshift range, $0.1 < z < 2.5$, and spans a significant portion of the age of universe, from 2.6 to 12.4 Gyr. In this chapter, we quantify the evolution of the following properties: V_{rot}, σ_g and their contributions to the total dynamical support. Moreover, we examine how these properties depend on stellar mass.

The format of this chapter is as follows. First, in §2, we summarize the data sets used and discuss the measurements of kinematics and stellar masses. In §3 and 4 we examine the evolution of galaxy kinematics and the fraction of rotationally supported systems in our sample, respectively, at a fixed stellar mass. Next, in §5, we link galaxy populations in time and examine their kinematic evolution. Finally, we summarize our conclusions in §6. We adopt a flat ΛCDM cosmology defined with (h, Ω_m, Ω_Λ) = (0.704, 0.272, 0.728).

4.2 Data

Measurements of the internal kinematics of star-forming galaxies are adopted from Kassin et al. (2012) (from the DEEP2 survey) and Simons et al. (2016) (from the SIGMA survey). Both samples are morphologically unbiased (i.e., not only disk-like systems are selected) and kinematics are measured from rest-optical emissions lines which trace the hot ionized $T \sim 10^4$ K gas in galaxies. The galaxies used in this chapter are shown in a stellar mass vs. star formation rate ($M_* - SFR$) diagram in Figure 4.1. We compare with the star-formation main sequence at their respective redshifts (from Speagle et al. 2014) and show that our sample is representative of typical star-forming galaxies over $0.1 < z < 2.5$. We note that the galaxies over the redshift range $0.3 < z < 0.7$ tend to lie slightly above the main sequence. However, the majority of the sample is within the 1σ scatter of the relation at all redshifts.

Below we describe the DEEP2 and SIGMA samples (§2.1 and 2.2, respectively), as well as the measurements of kinematics (§2.3), stellar masses and star-formation rates (§2.4).

4.2.1 DEEP2 sample

The intermediate redshift sample ($0.1 < z < 1.2$) used in this chapter is from Kassin et al. (2007) and Kassin et al. (2012) (hereafter K12). The sample is briefly discussed here and the reader is referred to K12 for further details. The galaxies

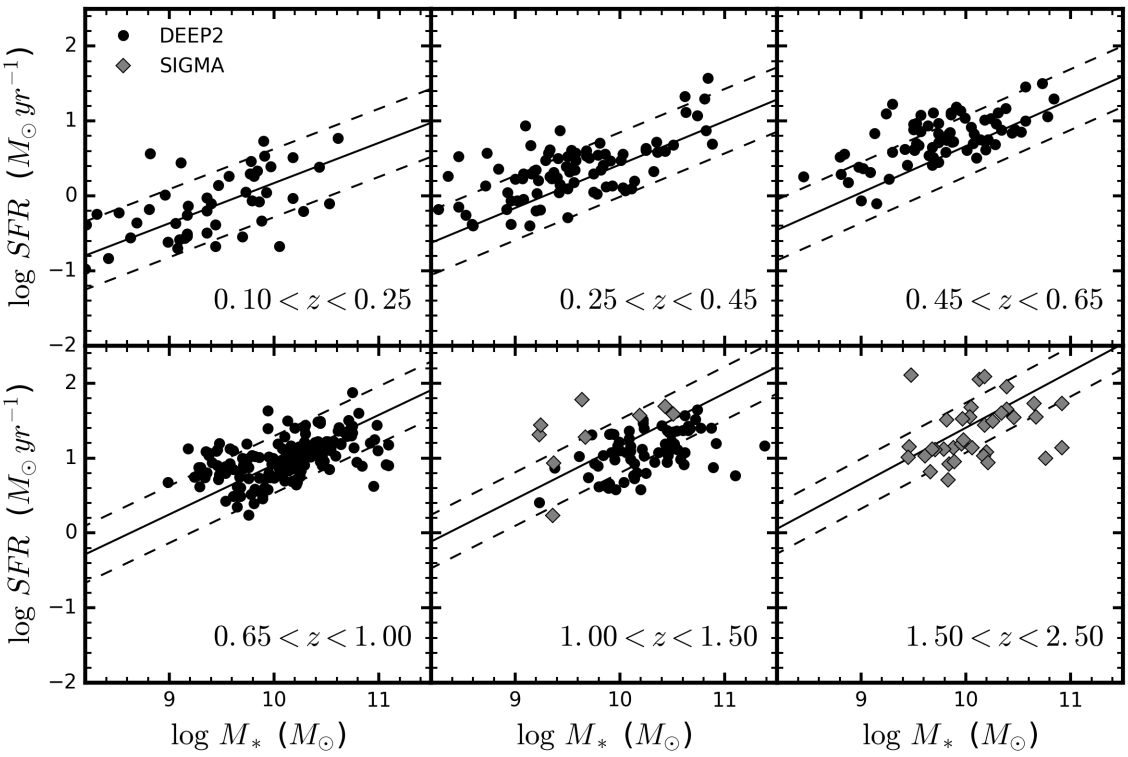

Figure 4.1: Galaxies in the DEEP2 (black circles) and SIGMA (grey diamonds) kinematics samples lie along the star-formation main sequence at their respective redshifts. The panels show redshift bins in equal intervals of lookback time. The solid and dashed lines are the main sequence fit and rms scatter for each redshift bin, respectively, from Speagle et al. 2014 and renormalized to a Chabrier IMF.

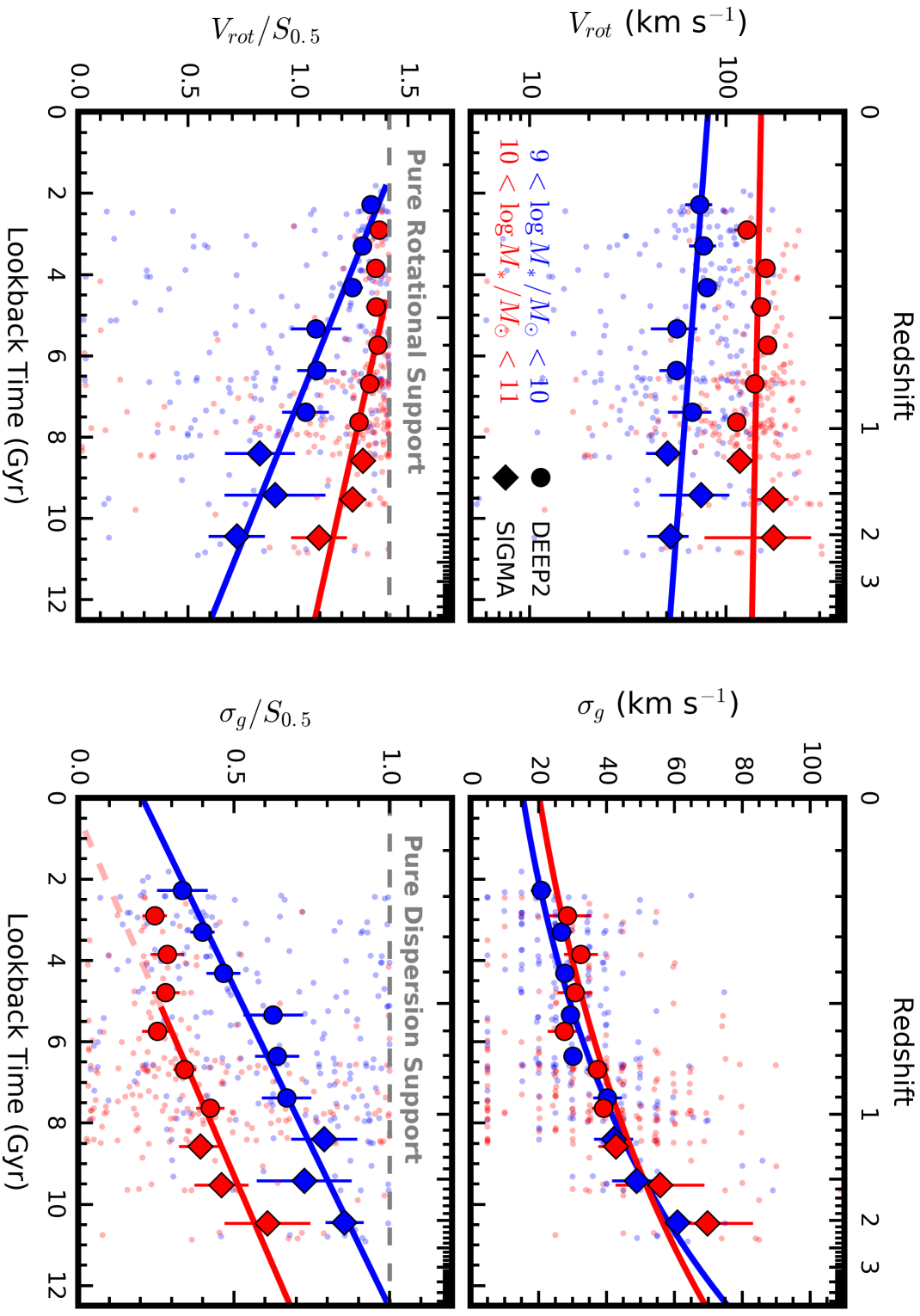

Figure 4.2: Caption on next page.

Figure 4.2: Star-forming galaxies evolve in V_{rot} and σ_g with time. The small faint background points are measurements for individual galaxies. The large points and associated error bars show medians of the individual points in bins of lookback time and their standard error. Solid lines are the best-fit relations to the median points. Low mass and high mass galaxies are shown in blue and red, respectively. Top left: The average rotation velocity, V_{rot}, increases with time since $z = 2.5$ for low mass galaxies, but shows no evolution for high mass galaxies. Top right: The gas velocity dispersion σ_g, which traces disordered motions, decreases precipitously from $z = 2.5$ to today for both low and high mass galaxies. In the bottom panels, V_{rot} and σ_g are normalized by $S_{0.5}$, which traces the total dynamical support of galaxies. This allows us to examine the fraction of total dynamical support that V_{rot} and σ_g provide to galaxies. At $z \sim 2$, low mass galaxies have a significant fraction of their total support in disordered motions. With time, all galaxies on average increase in rotational support (i.e., increase in $V_{rot}/S_{0.5}$) and decrease in dispersion support (i.e., decrease in $\sigma_g/S_{0.5}$). This happens earlier for higher mass galaxies.

in the K12 sample are located in the Extended Groth Strip. Spectra, from which the internal kinematics are measured, are from the DEEP2 survey (Newman et al., 2013a) and were taken with the DEIMOS instrument (Faber et al., 2003) on the Keck-II telescope. The slits used were $1''$ wide and the spectral resolution is $R \sim 5000$ ($\sigma_{instr} = 26$ km s^{-1}). The nominal on-source exposure times were 1 hour. The spectra were observed in natural optical seeing conditions, which varied between $0.5''$ and $1.2''$. Galaxies are selected to have bright enough emission lines to measure

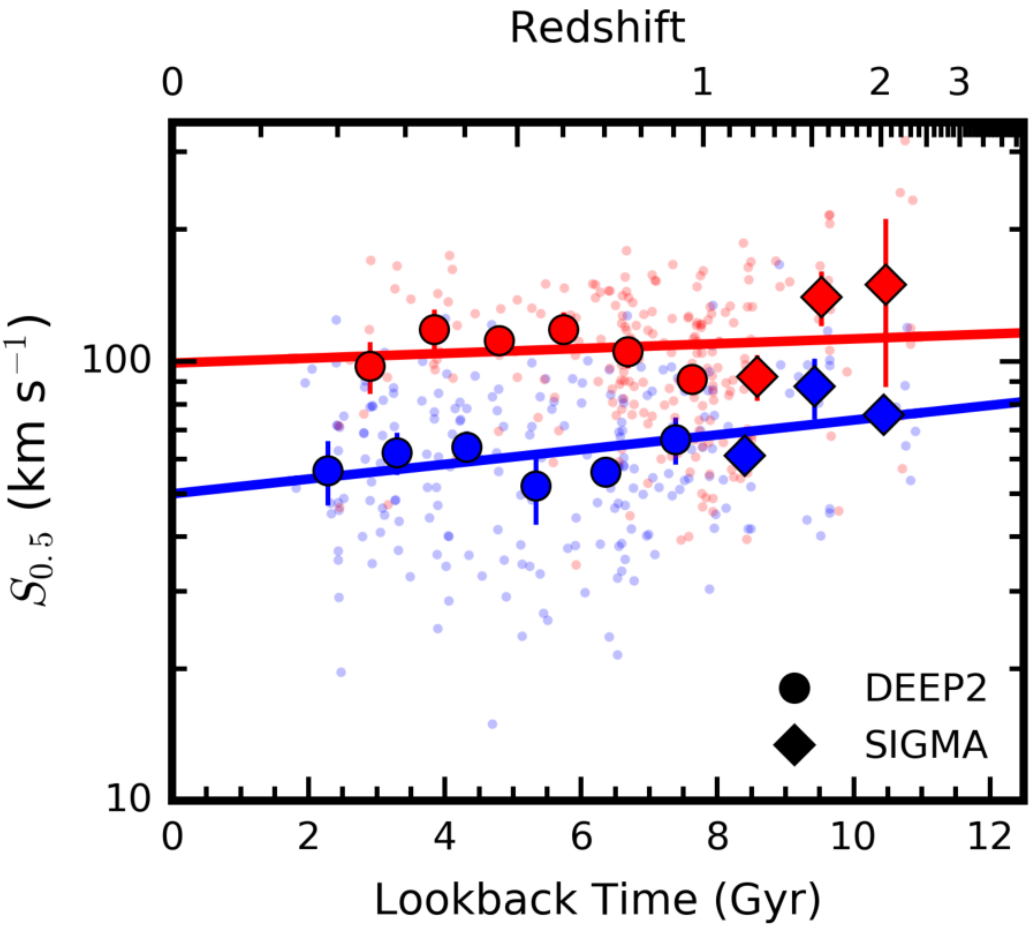

Figure 4.3: The evolution of $S_{0.5}$, a tracer of the galaxy potential well depth, is shown. This quantity mildly declines since $z = 2.5$ in galaxies with low stellar mass (blue), which is largely driven by the offset of the two highest redshift points. $S_{0.5}$ has not changed significantly in high mass galaxies (red). The points and lines are the same as in Figure 4.2.

kinematics ($\gtrsim 10^{-17}$ erg s^{-1} cm^{-2}). Additionally, galaxies are required to have V- and I-band imaging from the Hubble Space Telescope/Advanced Camera for Surveys (HST/ACS) instrument. Inclinations were measured from the Hubble imaging using the `SExtractor` program (Bertin & Arnouts, 1996) in Lotz et al. (2008). Galaxies are selected to have inclinations between $30° < i < 70°$, avoiding dust effects in edge-on systems and highly uncertain inclination corrections in face-on systems. Furthermore, galaxies are required to have slits aligned within 40° of the photometric major axes (Weiner et al., 2006a; Covington et al., 2010). Following Simons et al. (2015), we apply a conservative selection on the rest-optical HST half-light diameter ($D_{50} > 0.8$ times the FWHM of the seeing). This size selection removes 50 galaxies. The sample used in this chapter contains 462 galaxies.

4.2.2 SIGMA sample

The high redshift ($1.3 < z < 2.5$) sample used in this chapter is from the SIGMA kinematics survey (Simons et al. 2016; hereafter S16). The sample is briefly discussed here and we refer to S16 for further details. The galaxies in SIGMA are located in the UDS, GOODS-S and GOODS-N fields. Spectra were taken with the MOSFIRE spectrograph (McLean et al., 2010, 2012) on the Keck-I telescope as a part of the TKRS-2 survey (Wirth et al., 2015) and were also published in Trump et al. (2013) and Barro et al. (2014). The slits were $0.7''$ wide and the spectral resolution is $R \sim 3630$ ($\sigma_{inst} = 35\,\mathrm{km\ s^{-1}}$). The on-source exposure times ranged between 1.5

- 2 hours and the near-infrared seeing varied between 0.45 - 0.85″. HST/Wide Field Camera 3 (WFC3) imaging is available for all of the galaxies in SIGMA through the CANDELS survey (Grogin et al., 2011; Koekemoer et al., 2011). Axis ratios were measured from the HST/WFC3 H-band image using the `GALFIT` software (Peng et al., 2010) by van der Wel et al. (2012) and are used to derive inclinations. As in the K12 sample, all galaxies are required to have at least one slit aligned with the photometric position angle and intrinsic emission sizes which are large enough to resolve kinematics ($D_{50} > 0.8$ times the FWHM of the seeing; Simons et al. 2016). We remove four galaxies from the original sample for which inclinations corrections were not applied. The sample used in this chapter contains 45 galaxies and a catalog of their physical properties and kinematic measurements is available in S16.

4.2.3 Kinematic Measurements

Kinematics (rotation velocity V_{rot}, and gas velocity dispersion σ_g) were measured from strong nebular emission lines (Hα and [O III]λ5007) with the `ROTCURVE` program (Weiner et al., 2006a) in Kassin et al. (2007) and S16 for the DEEP2 and SIGMA surveys, respectively. The measurement technique is briefly discussed here and the reader is referred to Weiner et al. (2006a) for details.

Seeing blurs rotation and artificially elevates the velocity dispersion in the center of the galaxy (due to the rise in the rotation curve) and needs be taken into account in the kinematic modeling. `ROTCURVE` models the velocity profile of the emission

line, taking into account seeing, with two components: an arctangent rotation curve and a constant dispersion term. The rotation velocity uncorrected for inclination ($V_{rot} \times \sin i$) is measured at the flat portion of the rotation curve. Recent evidence has suggested that the rotation curves of high redshift star-forming galaxies fall, instead of flatten, beyond 1.5 effective radii (Lang et al., 2017; Genzel et al., 2017). Our high redshift data do not extend far enough to distinguish between these two cases. However, there is only a small difference in the maximum velocity derived from a fit to either model. While the flat part of the rotation curve is measured as the asymptote of the arctan model, the change in velocity beyond a few effective radii is negligible ($< 10\%$). If we adopt a value of V_{rot} which is measured at 1.5 R_e, the rotation velocities are lowered by ~ 0.1 dex. For consistency across redshift, we adopt V_{rot} as measured at the flat part of the modeled rotation curve in all of our galaxies.

Typical uncertainties on measurements of $V_{rot} \times \sin i$ are approximately 10 km s^{-1} for DEEP2 and 30 km s^{-1} for SIGMA. Uncertainties on σ_g are approximately 15 km s^{-1} for DEEP2 and 25 km s^{-1} for SIGMA. Inclination corrections are applied to the `ROTCURVE` values using the rest $\sim V$-band axis ratio measured from the Hubble images (ACS V- and I-bands in K12 for $0.1 < z < 0.6$ and $0.6 < z < 1.2$, respectively, and WFC3 H-band in S16 for $1.3 < z < 2.5$).

The gas velocity dispersion σ_g integrates small scale velocity gradients below the seeing limit (Covington et al., 2010; Kassin et al., 2014). It is mostly due to non-ordered motions among HII regions, but also includes smaller contributions from

thermal broadening ($\sim$10 km s^{-1} for H gas at 10^4 K) and the internal turbulence in HII regions ($\sim$20 km s^{-1} in local HII regions, Shields 1990). As in K12, we refer to σ_g as tracing "disordered motions".

The quantity V_{rot} measures the ordered motions of a galaxy while the quantity σ_g measures its disordered motions. We follow Weiner et al. (2006a) and Kassin et al. (2007) by combining both forms of dynamical support into the quantity $S_{0.5} = \sqrt{0.5\,V_{rot}^2 + \sigma_g^2}$. This term serves as a kinematic tracer of the total mass in an isothermal potential (Weiner et al., 2006a).

4.2.4 Stellar Mass and SFR Measurements

Stellar masses (M_*) were measured for the galaxies in the K12 sample using absolute B-band magnitudes and rest B$-$V colors (Bell & de Jong, 2001; Bell et al., 2005) with empirical corrections from spectral energy distribution (SED) fitting (Bundy et al., 2006), as in Lin et al. (2007). A Chabrier (2003) initial mass function was adopted and the uncertainties in stellar mass are approximately 0.2 dex. Star-formation rates (SFR) were derived in Noeske et al. (2007). For galaxies with 24μm detection, the obscured SFR was measured from the IR luminosity using the SED templates of Chary & Elbaz (2001) and is added to the unobscured component of the SFR, derived from the DEEP2 emission line luminosities (Weiner et al., 2007). Otherwise, the SFR was measured from the extinction corrected emission line luminosities following the calibration in Kennicutt (1998a).

Stellar masses for the galaxies in SIGMA were measured from SED fitting to the UV-optical-NIR data available in the CANDELS fields, as described in Barro et al. (2014). The fit was performed with `FAST` (Kriek et al., 2009) assuming a Chabrier (2003) initial mass function, Bruzual & Charlot (2003) stellar population synthesis models and a Calzetti extinction law (Calzetti et al., 2000). The uncertainties in stellar mass are approximately 0.3 dex (Mobasher et al., 2015). For galaxies with detections in the mid-to-far IR, the SFR was calculated using both the obscured (IR) and unobscured (UV) components (Kennicutt 1998a). Otherwise, SFRs are derived from the extinction corrected UV using the dust parameters of the best fit SED model.

4.3 Kinematic Evolution At Fixed Stellar Mass

We use measurements of V_{rot}, σ_g, and $S_{0.5}$ from the K12 and S16 samples to explore the kinematic evolution of star-forming galaxies from $z \sim 2.5$ to $z \sim 0.1$. Bins in equal intervals of lookback time (t_L) are adopted, each spanning 1 Gyr. Our conclusions are insensitive to the size of these intervals. We first examine evolution at fixed stellar mass for two stellar mass ranges: $9 < \log M_*/M_\odot < 10$ (hereafter referred to as "low mass") and $10 < \log M_*/M_\odot < 11$ (hereafter referred to as "high mass"). The $z \sim 2.2$ ($t_L \approx 10$ Gyr) bin in S16 does not include galaxies below $\log M_*/M_\odot = 9.4$ and instead encompasses $9.4 < \log M_*/M_\odot < 10$. The high stellar mass bin at

$z \sim 0.3$ is not included as it contains fewer than five galaxies. The removal or inclusion of these bins does not affect our results. We briefly summarize the results of this section below and refer to the subsections for details.

We find a large amount of scatter in the individual measurements of V_{rot}, σ_g and $S_{0.5}$ at a given mass but smooth *average* trends with mass and time, highlighting the need for a large sample. On average, the rotation velocities of low mass galaxies rise by a factor of 1.5 from $z \sim 2.5$ to the present day. High mass galaxies show little to no evolution in V_{rot} over the same period. The gas velocity dispersion smoothly declines from $z \sim 2.5$ to today at a remarkably similar rate in both mass bins. We consider contributions from V_{rot} and σ_g to the total dynamical support, as quantified by $S_{0.5}$. While all galaxies tend towards rotational support with time, it is obtained earlier for galaxies with higher stellar masses. This phenomenon, dubbed "kinematic downsizing", was first shown by K12 to $z = 1.2$ and we extend it to $z = 2.5$. This result follows from the facts that σ_g does not depend significantly on mass and low mass galaxies sit in shallower potential wells than high mass galaxies.

Low mass galaxies are delayed in their kinematic development, taking an additional 4 - 5 Gyr to reach the same level of rotational support as high mass galaxies. From $z = 2$ to $z = 1$, low mass galaxies are strongly supported by dispersion ($\sigma_g/S_{0.5} > 0.7$). By $z = 0.7$, high mass galaxies have developed strong rotational support ($\sigma_g/S_{0.5} < 0.3$), while low mass galaxies are only reaching a similar level of rotational support today.

It is important to note that galaxies grow in mass over time and so these trends at fixed stellar mass should not be interpreted as tracks for individual galaxy populations.

4.3.1 Increase in V_{rot} With Time for Low Mass Galaxies

The evolution of the rotation velocity, V_{rot}, is shown in the top left panel of Figure 4.2. The galaxies in our sample span a large range in V_{rot} at fixed epoch. This scatter is mostly intrinsic but is due in part to our relatively wide bins in stellar mass (1 dex) and to a lesser extent from measurements uncertainties.

At all times, the average rotation velocity is higher for galaxies with higher stellar mass. We find a mild increase of the average V_{rot} with time in galaxies with low stellar mass, rising from 50 km s^{-1} at $z = 2$ to 70 km s $^{-1}$ at $z = 0.2$. High mass galaxies show little evolution in V_{rot} over the same time period. We estimate the standard error on the median V_{rot} in each bin through bootstrap resampling and perform an uncertainty weighted least squares fit to the median points with a line:

$$\log\left(\frac{V_{rot}}{\text{km s}^{-1}}\right) = a\left(\frac{t_L}{\text{Gyr}}\right) + b \tag{4.1}$$

The best-fit values of the slope and intercept are $a = -0.02 \pm 0.01$ (i.e., slow rise) and $b = 1.91 \pm 0.07$ for our low stellar mass bin, and $a = -0.004 \pm 0.014$ (i.e., no

evolution) and $b = 2.18 \pm 0.09$ for our high stellar mass bin. The intercept value of each mass bin, i.e., V_{rot} at $z = 0$, is consistent with the local stellar mass Tully-Fisher relation (90 and 175 km s^{-1} at $\log M_*/M_\odot = 9.5$ and 10.5, respectively; Reyes et al. 2011).

4.3.2 Smooth Decay of σ_g With Time for All Galaxies

The evolution of the gas velocity dispersion, σ_g, is shown in the top right panel of Figure 4.2. As with V_{rot}, galaxies in our sample span a wide range in σ_g at all epochs, largely due to measurement uncertainties.

The galaxies at the highest redshifts have values of σ_g which are roughly 3 times larger than the galaxies at the lowest redshifts (see also Wisnioski et al. 2015). The quantity σ_g decreases from 70 km s^{-1} to 20 km s^{-1} over $0.2 < z < 2.0$. As first shown in K12, σ_g roughly doubles over $0.1 < z < 1.2$, which spans approximately 8 Gyrs. Although the time from $z = 1$ to $z = 2$ is much shorter, only 3 Gyrs, we find significant evolution in σ_g during this period, with the median increasing from 40 km s^{-1} to 70 km s^{-1}. We perform a fit to the median $t_L - \sigma_g$ relation for our two mass bins with:

$$\log\left(\frac{\sigma_g}{\text{km s}^{-1}}\right) = a\left(\frac{t_L}{\text{Gyr}}\right) + b \tag{4.2}$$

The best fit values are $a = 0.055 \pm 0.010$ and $b = 1.19 \pm 0.04$ for the low mass bin and $a = 0.043 \pm 0.010$ and $b = 1.31 \pm 0.07$ for the high mass bin. There is no significant difference between the evolution of σ_g in the low mass and high mass bins. *This result implies a mass-independent half-life timescale for σ_g, the time over which it declines by a factor of 2, of approximately 6 Gyrs.* The intercept values, i.e., σ_g at $z = 0$, are consistent with measurements of the ionized gas velocity dispersion in local star-forming disk galaxies ($\sim 15 - 25$ km s^{-1}, e.g., Epinat et al. 2008).

4.3.3 Evolution of Dynamical Support, $S_{0.5}$, With Time

In Figure 4.3, we examine the evolution of $S_{0.5}$, which traces the total dynamical support of galaxies. We fit a line to the median $S_{0.5}$ vs. lookback time:

$$\log\left(\frac{S_{0.5}}{\text{km s}^{-1}}\right) = a\left(\frac{t_L}{\text{Gyr}}\right) + b \tag{4.3}$$

The best-fit slope and intercept values are $a = 0.017 \pm 0.008$ and $b = 1.70 \pm 0.06$ for the low mass bin and $a = 0.01 \pm 0.01$ and $b = 2.00 \pm 0.09$ for the high mass bin. The quantity $S_{0.5}$ has marginally declined in low mass galaxies since $z = 2.5$, i.e., they now sit in shallower potential wells, but we measure no significant evolution in high mass galaxies.

While the fit to the low mass galaxies indicates a smooth evolution, we caution

that the trend is largely driven by the high redshift measurements. The median points below $z = 1.5$ are consistent with a flat slope. The points above $z = 1.5$ are all above this flat line, consistent with a zero-point shift in the modified Tully-Fisher relation at high redshift (Cresci et al. 2009; Price et al. 2016; Straatman et al. 2017; Übler et al. 2017).

4.3.4 Fraction of Total Dynamical Support Given By V_{rot} and σ_g Over Time

We normalize V_{rot} and σ_g by $S_{0.5}$ and measure the relative contributions of ordered and disordered motions, respectively, to the total dynamical support. A thin disk which is supported by rotation will tend toward $V_{rot}/S_{0.5} = \sqrt{2}$, and a system which is supported by dispersion will tend toward $\sigma_g/S_{0.5} = 1$.

The evolution of $V_{rot}/S_{0.5}$ is shown in the bottom left panel of Figure 4.2. K12 showed that $V_{rot}/S_{0.5}$ rises from $z = 1.2$ to now and is a strong function of mass. We find a smooth extension of these results to $z = 2.5$.

At all redshifts, high mass galaxies have higher values of $V_{rot}/S_{0.5}$, i.e., they are more rotationally-supported, than low mass galaxies. This phenomenon, dubbed "kinematic downsizing" (K12, S16), is present out to $z = 2.5$. High mass galaxies reach a strong level of rotational support ($V_{rot}/S_{0.5} > 1.3$) by a lookback time of $5-6$ Gyr, or $z \sim 0.7$. Low mass galaxies reach the same degree of rotational support

a few Gyrs later, by $z \sim 0.2$. We fit a line to the median $V_{rot}/S_{0.5}$ using only the rising part of this relation, which covers $0.5 < z < 2.5$ in the high mass bin and $0.1 < z < 2.5$ in the low mass bin:

$$\frac{V_{rot}}{S_{0.5}} = a\left(\frac{t_L}{\mathrm{Gyr}}\right) + b \tag{4.4}$$

The best fit slope and intercept are $a = -0.074 \pm 0.010$ and $b = 1.53 \pm 0.04$ for low mass galaxies and $a = -0.042 \pm 0.020$ and $b = 1.59 \pm 0.08$ for high mass galaxies. The values for the best-fit slopes are similar and suggest that low mass and high mass galaxies develop rotational support at similar rates. We refit the high mass galaxies with a slope fixed to the best-fit slope of the low mass galaxies. At fixed slope, the high mass and low mass trends are offset by 4.3 Gyr. In other words, the assembly of rotational support in the high mass galaxies is, on average, followed $4-5$ Gyrs later by similar kinematic assembly in low mass galaxies.

As expected, we find inverted trends in the evolution of $\sigma_g/S_{0.5}$ (Figure 4.2, bottom right). On average, $\sigma_g/S_{0.5}$ declines with time for all galaxies and is always larger for low mass galaxies. Given that σ_g itself does not depend on stellar mass (top right panel), its relative contribution to the total dynamical support will always be larger in galaxies with lower stellar mass. Beyond $z = 1.0$, or a lookback time of ~ 9 Gyr, low mass galaxies have large contributions from dispersion ($\sigma_g/S_{0.5} \gtrsim 0.8$). They progressively decline in dispersion support with time up to the present day. At $z = 0$, both low mass and high mass galaxies have low levels of dispersion support

($\sigma_g/S_{0.5} \leq 0.4$) and high levels of rotational support ($V_{rot}/S_{0.5} \geq 1.3$). We fit a line to the median $\sigma_g/S_{0.5}$ over the declining part of the relation, covering $0.5 < z < 2.5$ for high mass galaxies and $0.1 < z < 2.5$ for low mass galaxies:

$$\frac{\sigma_g}{S_{0.5}} = a\left(\frac{t_L}{\mathrm{Gyr}}\right) + b \tag{4.5}$$

The best fit slope and intercept values are $a = 0.063 \pm 0.01$ and $b = 0.20 \pm 0.04$ for low mass galaxies and $a = 0.056 \pm 0.02$ and $b = -0.02 \pm 0.11$ for high mass galaxies. As before, the slopes are statistically identical and suggest that the dispersion support declines at similar rates in both mass bins. We refit to the high mass galaxies with a slope fixed to low mass fit and measure an offset between the mass bins of 4.6 Gyrs. These results mirror our earlier conclusions and once again suggest that kinematic assembly in low mass galaxies is delayed from that in high mass galaxies by $\sim 4-5$ Gyrs.

4.4 The Fraction of Galaxies With Rotational Support

We now investigate the fraction of star-forming galaxies with $V_{rot}/\sigma_g > 1$ and $V_{rot}/\sigma_g > 3$ as a function of time. These two values are arbitrary, but serve as relatively lenient benchmarks of rotational support. For perspective, sufficiently mas-

sive ($\log M_*/M_\odot > 10$) star-forming disk galaxies in the local universe tend to have values of $V_{rot}/\sigma_g > 5$ when measured through a hot ionized gas tracer such as Hα (Epinat et al., 2008) and $V_{rot}/\sigma_g > 10$ when measured through a cold neutral gas tracer such as Hslowromancapi@ (Walter et al., 2008; de Blok et al., 2008).

We divide our sample into 3 overlapping bins in fixed stellar mass: $9 < \log M_*/M_\odot < 10$ ("low mass"), $9.5 < \log M_*/M_\odot < 10.5$ ("intermediate mass") and $10 < \log M_*/M_\odot < 11$ ("high mass").

Figure 4.4 (left) shows the evolution of the fraction of galaxies with $V_{rot}/\sigma_g > 1$. As first reported by K12 to $z = 1.2$, this fraction increases with time for all galaxies and is always higher at higher stellar masses. The SIGMA sample extends these trends to $z = 2$. The fraction of galaxies in SIGMA with $V_{rot}/\sigma_g > 1$ for the low, intermediate and high mass bins is 49($\pm$15)%, 51($\pm$12)%, and 70($\pm$13)%, respectively, at $z = 2$. That is, about half of the star-forming galaxies in the low and intermediate mass bins have dominant contributions from σ_g. The standard error on the reported fractions are calculated via bootstrap resampling. Measurement uncertainties will push individual galaxies above or below the threshold in V_{rot}/σ_g and we account for this by perturbing the values of V_{rot} and σ_g by their associated errors on each draw.

In Figure 4.4 (right), the fraction of galaxies which have $V_{rot}/\sigma_g > 3$ is shown. The fraction of galaxies in SIGMA at $z = 2$ that meet this benchmark for the low, intermediate and high mass bins are only 15($\pm$10)%, 11($\pm$8)%, and 30($\pm$13)%, respectively.

We fit the evolution of both of these fractions, F, with:

$$F\left(\frac{V_{rot}}{\sigma_g} > x\right) = a\left(\frac{t_L}{\mathrm{Gyr}}\right) + b \tag{4.6}$$

The best-fit slope and intercept for $F(V_{rot}/\sigma_g > 1)$ are $a = -0.057 \pm 0.006$ and $b = 1.08 \pm 0.04$ for low mass galaxies, $a = -0.056 \pm 0.009$ and $b = 1.19 \pm 0.066$ for intermediate mass galaxies and $a = -0.045 \pm 0.009$ and $b = 1.21 \pm 0.071$ for high mass galaxies. Similarly, the best-fit values for $F(V_{rot}/\sigma_g > 3)$ are $a = -0.069 \pm 0.009$ and $b = 0.84 \pm 0.07$ for low mass galaxies, $a = -0.085 \pm 0.007$ and $b = 1.09 \pm 0.05$ for intermediate mass galaxies and $a = -0.08 \pm 0.01$ and $b = 1.20 \pm 0.09$ for high mass galaxies.

By $z = 0.2$, more than 70% of star-forming galaxies with $\log M_*/M_\odot > 9$ have reached $V_{rot}/\sigma_g > 3$ and more than 90% have reached $V_{rot}/\sigma_g > 1$. Even at $z = 2$, most of the sample shows some degree of rotation. More than half of galaxies at this redshift have $V_{rot}/\sigma_g > 1$. However, these galaxies are unlike local rotating galaxies, whose V_{rot}/σ_g often exceeds 5. The redshift at which 35% of galaxies have $V_{rot}/\sigma_g > 3$ is $z = 1$, 1.5 and 2.6 for the low, intermediate and high mass bins, respectively. Kinematic analogs of local well-ordered disk galaxies are rare at $z = 2$. At this redshift, only 7 (16%) and 2 (4%) of the galaxies in our sample reach $V_{rot}/\sigma_g > 5$ and > 10, respectively.

4.4.1 Comparison With the Literature

In Figure 4.4 (left), we compare our measurements with those in the literature. Any comparison between surveys is complicated due in large part to differences in sample selection and measurement techniques. We refrain from performing detailed corrections between the samples and only report here a straightforward comparison. We include measurements from the following surveys: KROSS at $z \sim 1$ (Stott et al., 2016), KMOS-3D at $z \sim 1$ and $z \sim 2$ (Wisnioski et al., 2015), MASSIV at $z \sim 1.3$ (Contini et al., 2012), AMAZE/LSD at $z \sim 3$ (Gnerucci et al., 2011), and the KDS survey at $z \sim 3.5$ (Turner et al., 2017b). The adopted measurements are briefly described below. To account for differences in the stellar mass of galaxies in each sample, we color-code each by its approximate mass coverage. Our sample and the literature measurements are in good agreement once we account for stellar mass.

The KROSS sample covers the redshift range $0.6 < z < 1.0$ and a stellar mass range of $9.0 \lesssim \log M_*/M_\odot \lesssim 11.0$. A catalog of kinematic measurements for 586 typical star-forming galaxies was released in Harrison et al. (2017). We use this catalog to calculate the fraction of resolved galaxies in KROSS which have rotation velocities that exceed their intrinsic velocity dispersions. We adopt mass bins which overlap our sample and these are shown as separate points in Figure 4.4. The first-year sample from the KMOS-3D survey contains 191 star-forming galaxies in two redshift intervals: $0.7 < z < 1.1$ and $1.9 < z < 2.7$. These galaxies cover a stellar mass range of $9.6 \lesssim \log M_*/M_\odot \lesssim 11.1$ at $z \sim 1$ and $10 \lesssim \log M_*/M_\odot \lesssim 11.2$ at

$z \sim 2$. Wisnioski et al. (2015) report the fraction of galaxies in their sample with rotationally-supported kinematics as 93% and 74% at $z \sim 1$ and $z \sim 2$, respectively. We include the sample of 48 MASSIV galaxies from Vergani et al. (2012), covering $1 < z < 1.6$ and a stellar mass range of $9.5 \lesssim \log M_*/M_\odot \lesssim 11$. We adopt the V/σ measurements in their Table 2 and calculate a rotation-dominated fraction of 65%. We include the high redshift sample from the AMAZE/LSD survey of 33 galaxies over $2.6 < z < 4.9$ and a stellar mass range of $9.0 \lesssim \log M_*/M_\odot \lesssim 11.0$. Gnerucci et al. (2011) report that 33% of the AMAZE galaxies can be classified as rotationally-supported. Finally, we include results from the KMOS Deep survey (KDS) at $z \sim 3.5$ (Turner et al., 2017b) which covers a mass range of $8 < \log M_*/M_\odot < 11$. Turner et al. 2017b report that 13/32 of the isolated field galaxies in this sample are rotation-dominated. We remove the 4 galaxies with $\log M_*/M_\odot < 9$, 3 of which are dispersion-dominated, and compute a rotation-dominated fraction of 43% over our mass range.

4.5 Tracing Galaxy Populations with Abundance Matching

In previous sections of this chapter, galaxies trends are reported for a fixed stellar mass. However, as a natural consequence of ongoing star formation and mass accretion, the galaxies in our sample will grow in stellar mass with time and migrate between mass bins. As such, the trends discussed so far should not be interpreted as

tracks for individual galaxy populations. In order to trace the evolution of a galaxy population from $z = 2.5$ to $z = 0$, we adopt a model linking high redshift galaxies with their more massive low redshift descendants.

Galaxy populations are tracked in time using the multi-epoch abundance matching (MEAM) model (Moster et al., 2013), following Papovich et al. (2015). The conclusions of this section are similar if we adopt other abundance matching models from the literature (e.g., Rodríguez-Puebla et al. 2017). The abundance matching technique assumes that there is a monotonic relation between the stellar mass of a galaxy and its halo mass, with the most massive galaxies residing in the most massive halos. Observed stellar mass functions are then rank assigned to simulated halo mass functions at all redshifts and galaxy populations are tracked in time.

Moster et al. (2013) adopt halo and subhalo evolution from the Millenium simulation and stellar mass functions up to $z \sim 4$ from several surveys in the literature (Pérez-González et al., 2008; Li & White, 2009; Santini et al., 2012). Fitting functions are provided for the mass accretion history, star-formation history and stellar mass loss rates of galaxies as a function of mass. We integrate these prescriptions in time to track the average stellar mass evolution of galaxy populations. We divide our observational sample into 3 populations of $z = 0$ halo masses of $11 < M_h/M_\odot < 11.5$, $11.5 < M_h/M_\odot < 12.3$ and $12.3 < M_h/M_\odot < 14.5$. These correspond to typical $z = 0$ stellar masses of $\log M_*/M_\odot \sim 9.4$, 10.3, and 11.1, respectively.

The average stellar mass evolution for these three populations is shown in Figure

4.5. The SIGMA survey does not cover $\log M_*/M_\odot < 9$ and so the lowest mass bin does not have coverage beyond $z \sim 1$. Similarly, the intermediate mass bin only extends to $z \sim 1.5$. We use these tracks to link galaxies in our sample with their appropriate descendants.

4.5.1 Increasing V_{rot}, Decreasing σ_g, and Increasing $S_{0.5}$ With Time

Using the abundance matching technique to link galaxy populations in time, we now revisit the evolution of V_{rot}, σ_g and $S_{0.5}$ in Figures 4.6 and 4.7.

The most striking difference is in the evolution of V_{rot}. At fixed stellar mass we measured mild to no evolution in V_{rot}. However, in Figure 4.6 (top left) we show that V_{rot} strongly evolves for the evolving galaxy population: *star-forming galaxies spin-up with time on average*. We use Eq. 4.1 and fit to the median evolution of V_{rot} in each mass bin. The best-fit slope and intercept values are $a = -0.047 \pm 0.012$ and $b = 0.90 \pm 0.054$ for low mass galaxies, $a = -0.053 \pm 0.010$ and $b = 1.11 \pm 0.04$ for intermediate mass galaxies, and $a = -0.058 \pm 0.090$ and $b = 1.27 \pm 0.070$ for high mass galaxies. The best-fit slopes are similar and indicate that star-forming galaxies in this mass range have a typical V_{rot} doubling timescale of $\sim$6 Gyrs, similar to the half-life timescale of σ_g at fixed stellar mass (§3.2).

At fixed galaxy population, we again find that σ_g dramatically declines with time

(Figure 4.6, top right). Intermediate mass and high mass galaxies trace each other back to $z = 1.5$, rising from 30 km s^{-1} at $z = 0.2$ to 45 km s^{-1} at $z = 1.5$. The high mass galaxies, for which we have measurements out to high redshift, reach typical values of $\sigma_g = 60$ km s^{-1} at $z = 2$.

The evolution of $S_{0.5}$ for the abundance matched populations is shown in Figure 4.7. At fixed stellar mass, we found a mild decline in $S_{0.5}$ with time. At fixed galaxy population, we find that $S_{0.5}$ increases with time for all galaxies. This result suggests that, perhaps unsurprisingly, galaxy potential wells steepen as they acquire mass. The quantity σ_g declines with time on average and so the additional dynamical support comes from the increase in V_{rot}.

As before, we use Eq. 4.3 and fit to the median $S_{0.5}$ evolution for each mass bin. The best-fit slope and intercept values are $a = -0.015 \pm 0.019$ and $b = 1.73 \pm 0.08$ for the fixed population at low mass, $a = -0.01 \pm 0.01$ and $b = 2.0 \pm 0.05$ at intermediate mass, and $a = -0.03 \pm 0.04$ and $b = 2.24 \pm 0.28$ at high mass.

We normalize V_{rot} and σ_g by $S_{0.5}$ (Figure 4.6, bottom panels) and find the same general behavior as before: while all galaxy populations increase in rotational support with time (rising in $V_{rot}/S_{0.5}$ and declining in $\sigma_g/S_{0.5}$), massive galaxies are the most rotationally supported at all times on average. The high mass population reaches a strong level of rotational support ($V_{rot}/S_{0.5} > 1.3$) as far back as $z = 1.5$, while the intermediate mass and low mass populations reach the same degree of rotational support at $z = 0.5$ and $z = 0.2$, respectively.

4.5.2 Fraction of galaxies with $V_{rot}/\sigma_g > 1$ and 3 with time

In Figure 4.8, we use the linked galaxy populations to revisit how the fraction of galaxies with $V_{rot}/\sigma_g > 1$ and 3 evolves with time and galaxy mass.

As before, at a fixed stellar mass, we find trends that are smooth in both mass and redshift. These results are consistent with kinematic downsizing: more galaxies tend to become rotation-dominated with time and, at all times, galaxies are more likely to be rotation-dominated at higher mass. As before, this result is due in part to the large decline in σ_g with time and its weak dependance on mass. Additionally, unlike the case at fixed stellar mass, there is a contribution from the steep rise in V_{rot} with time in all galaxy populations and its strong dependance on mass.

We use Eq. 4.6 to fit to the evolution in each mass bin. The best-fit slope and intercept for $F(V_{rot}/\sigma_g > 1)$ are $a = -0.047 \pm 0.012$ and $b = 0.90 \pm 0.05$ at low mass, $a = -0.053 \pm 0.007$ and $b = 1.11 \pm 0.04$ at intermediate mass and $a = -0.06 \pm 0.009$ and $b = 1.27 \pm 0.07$ at high mass. For $F(V_{rot}/\sigma_g > 3)$ the best-fit values are $a = -0.07 \pm 0.013$ and $b = 0.59 \pm 0.06$ at low mass, $a = -0.052 \pm 0.01$ and $b = 0.78 \pm 0.06$ at intermediate mass and $a = -0.10 \pm 0.01$ and $b = 1.32 \pm 0.09$ at high mass.

The majority of galaxies in these populations have some degree of rotational support (Figure 4.8, left). More than half of the galaxies in the low mass bin have

$V_{rot}/\sigma_g > 1$ at $z = 1$ and the intermediate and high mass bins reach similar values at $z = 2$.

However, it is much less common for galaxies to reach $V_{rot}/\sigma_g > 3$ at high redshifts (Figure 4.8, right). Less than 30% of galaxies in the low mass population have $V_{rot}/\sigma_g > 3$ beyond $z \sim 0.4$ (Figure 4.8, right), indicating that it would have been exceedingly rare for today's LMC-mass galaxies to have had strong rotational support at redshifts greater than 1. The intermediate and high mass populations drop below 30% around $z \sim 1.5$. The most massive star-forming disks in the local universe ($\log M_{*,z=0}/M_\odot > 10.0$; i.e., Milky-Way and M31-mass galaxies) were likely weakly rotationally-supported, $V_{rot}/\sigma_g < 3$, at the peak of cosmic star-formation.

4.6 Discussion and Conclusions

To explore the evolution of internal galaxy kinematics over a continuous period of time from $z = 2.5$ to today, measurements from the DEEP2 survey ($0.1 < z < 1.2$; Kassin et al. 2007, 2012) are combined with those from the SIGMA survey ($1.3 < z < 2.5$; Simons et al. 2016). The full sample contains 507 star-forming galaxies and covers a mass range of $9 < \log M_*/M_\odot < 11$. Our sample is homogenous and representative of galaxies on the star-formation main sequence. There is no selection on morphology. Kinematics were measured using the same software in both surveys. This data set is the largest contiguous and morphologically unbiased sample

of kinematics in the literature and it extends the work of Kassin et al. (2012) from $z = 1.2$ into the peak of cosmic star-formation at $z = 2$.

Kinematics are measured from rest-optical emission lines (Hα, [O III]λ 5007) in slit spectra, which trace hot ionized 10^4 K gas. Two kinematic quantities are measured: the rotation velocity V_{rot}, which traces ordered motions, and the gas velocity dispersion σ_g, which traces disordered motions. Both of these quantities provide dynamical support, and when combined into the quantity $S_{0.5} = \sqrt{0.5V_{rot}^2 + \sigma_g^2}$, trace the depth of galaxy potential wells (Weiner et al., 2006a; Kassin et al., 2007; Covington et al., 2010).

Average trends in σ_g and V_{rot} with time are presented for galaxies at fixed stellar mass. We find a smooth and dramatic decline in σ_g since z = 2.5. The time for σ_g to decline by a factor of two, or the half-life time, is $\sim$ 6 Gyrs. Remarkably, this evolution is similar for all masses. Over the same time period, V_{rot} increases in galaxies with low stellar mass ($9 < \log M_*/M_\odot < 10$), but does not evolve in galaxies with high stellar mass ($10 < \log M_*/M_\odot < 11$).

The fractions of dynamical support provided by rotation and dispersion are measured by taking the ratios of V_{rot} and σ_g to $S_{0.5}$. At a fixed stellar mass, all galaxies on average rise in $V_{rot}/S_{0.5}$ with time, i.e. they become increasingly supported by rotation. In the same vein, all galaxies on average decline in $\sigma_g/S_{0.5}$ with time, i.e., they become decreasingly supported by dispersion. While the slopes of these trends ($V_{rot}/S_{0.5}$ and $\sigma_g/S_{0.5}$ with time) are similar for all masses, high mass galaxies have

higher $V_{rot}/S_{0.5}$ and lower $\sigma_g/S_{0.5}$ at all times. This indicates a time delay in the development of rotational support between low mass and high mass galaxies, with low mass trailing high mass by a few Gyrs (i.e., "kinematic downsizing"; Kassin et al. 2012; Simons et al. 2016). This result arises from the independence of σ_g on mass: a given value of σ_g assumes a more dominant role in the shallower potential wells that host low mass galaxies.

These results are complementary to studies which track morphological regularity, tracing the distribution of stars in galaxies, as a function of mass and redshift. Morphologically regular stellar disks are increasingly common at low redshift ($z \leq 1.5$) and high mass (e.g., Mortlock et al. 2013; van der Wel et al. 2014b; Huertas-Company et al. 2016). For example, Huertas-Company et al. (2016) find that as much as 80% of the stellar mass density at $z = 2$ resides in galaxies with disturbed/irregular morphologies.

Galaxies grow in stellar mass with time and so these trends, which are at fixed stellar mass, should not be interpreted as tracks for individual galaxy populations. To link galaxy populations in time, we adopt an abundance matching model. Doing so, we find that V_{rot} increases, σ_g decreases, and the potential well depth $S_{0.5}$ increases with time for all galaxies. The simultaneous rise in $S_{0.5}$ and V_{rot} indicates that galaxies spin-up as they assemble their mass. On average, a star-forming galaxy of Milky-Way mass which is today strongly supported by rotation ($\sigma_g/S_{0.5} < 0.3$) was likely strongly supported by dispersion at $z = 2$ ($\sigma_g/S_{0.5} = 0.7$), at a time when

it was also much less massive. These results suggest that the assembly of stellar mass and the assembly of rotational support were contemporaneous and that the processes which govern stellar mass assembly at late times should also promote disk formation. These processes likely include, but are not limited to, the accretion of mass and (re-)formation of disks in gas-rich interactions (e.g., Robertson et al. 2006; Governato et al. 2009; Snyder et al. 2015; Rodriguez-Gomez et al. 2017), the cessation of misaligned or destructive mergers (e.g., Aumer et al. 2013), and a transition in the mode of star-formation from one which is bursty and violent at high redshift to one which is relatively calm and stable at low redshift (e.g., Ceverino et al. 2017; Ma et al. 2017).

At $z = 0.2$, the vast majority (90%) of star-forming galaxies are rotation-dominated ($V_{rot} > \sigma_g$). By $z = 2$, the percentage of galaxies with $V_{rot} > \sigma_g$ has declined to 50% for low mass systems ($10^9 - 10^{10}\,M_\odot$) and 70% for high mass systems ($10^{10} - 10^{11} M_\odot$). These measurements are consistent those in the literature once stellar mass is taken into account. We consider a stronger criterion for rotational support, $V_{rot} > 3\,\sigma_g$, and find that the fractions of galaxies meeting this threshold drop below 35% for all masses. For perspective, most sufficiently massive galaxies in the local universe ($\log M_*/M_\odot > 10$) have $V_{rot}/\sigma_g > 5$ while the most massive disks regularly have $V_{rot}/\sigma_g > 10$.

In conclusion, strong rotational support was exceedingly rare at $z = 2$ and the kinematic characteristics of local disks, i.e., low σ_g and high V_{rot}/σ_g, were only just

beginning to emerge. This epoch is one of disk assembly, as star-forming galaxies are rapidly assembling stellar mass and beginning to develop the first well-ordered disks.

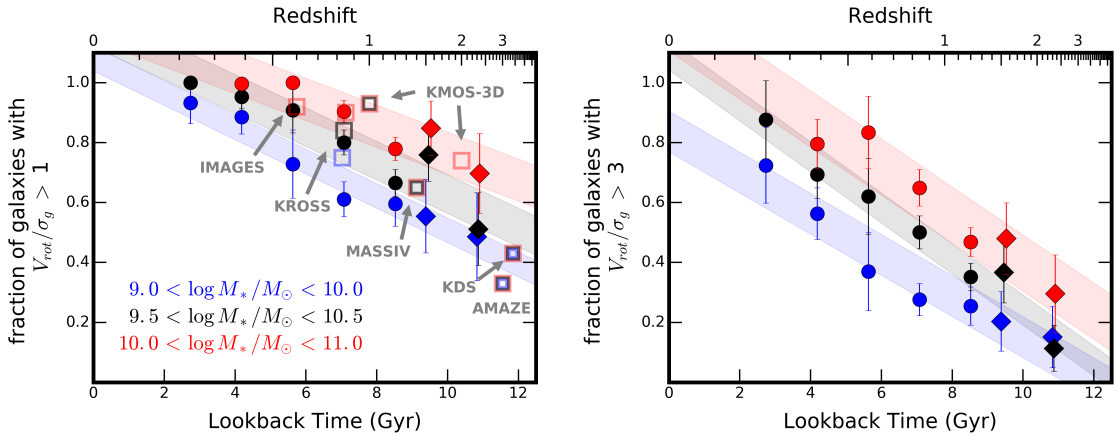

Figure 4.4: The fraction of star-forming galaxies with disk-like kinematics declines with increasing redshift and decreasing mass. In the left panel, the fractions of galaxies with $V_{rot}/\sigma_g > 1$ are shown as a function of lookback time and redshift (bottom and top x-axes, respectively) and galaxy stellar mass. The solid points show measurements from DEEP2 (circles) and SIGMA (diamonds) and the error bars are measured via bootstrap resampling. The shaded swaths show the uncertainty on the intercept in a linear fit to the points. By $z = 2$, only $\sim 50 - 70\%$ of all galaxies meet the very lenient criteria of $V_{rot}/\sigma_g > 1$. In the right panel, the fractions of galaxies with $V_{rot}/\sigma_g > 3$ are shown. By $z = 2$, less than 40% of all galaxies meet this criterion. Measurements from kinematics surveys in the literature are shown as open squares and are color-coded by their mass ranges using the same stellar mass bins used for our data. Samples which span multiple bins in mass are shown with two or more colors. We find good agreement among all surveys once stellar mass is accounted for.

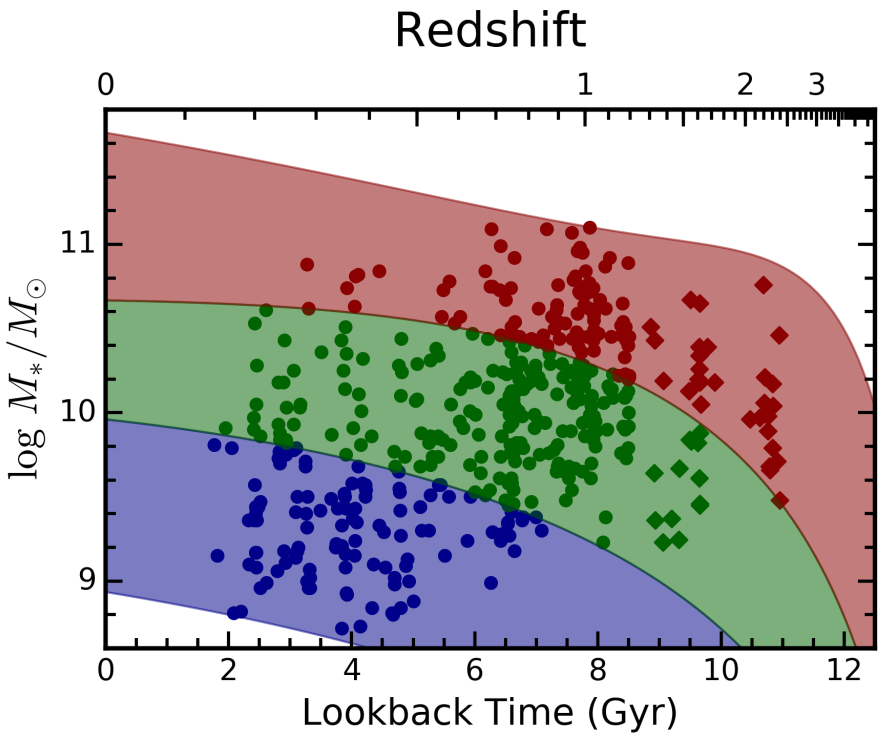

Figure 4.5: Galaxies in our sample are linked in time using an abundance matching model from Moster et al. 2013. Three galaxy populations with $z = 0$ halo masses of $11 < M_h/M_\odot < 11.5$ (dark blue), $11.5 < M_h/M_\odot < 12.3$ (dark green) and $12.3 < M_h/M_\odot < 14.5$ (dark red) are tracked in time. The average stellar mass evolution of the models is shown as a shaded swath.

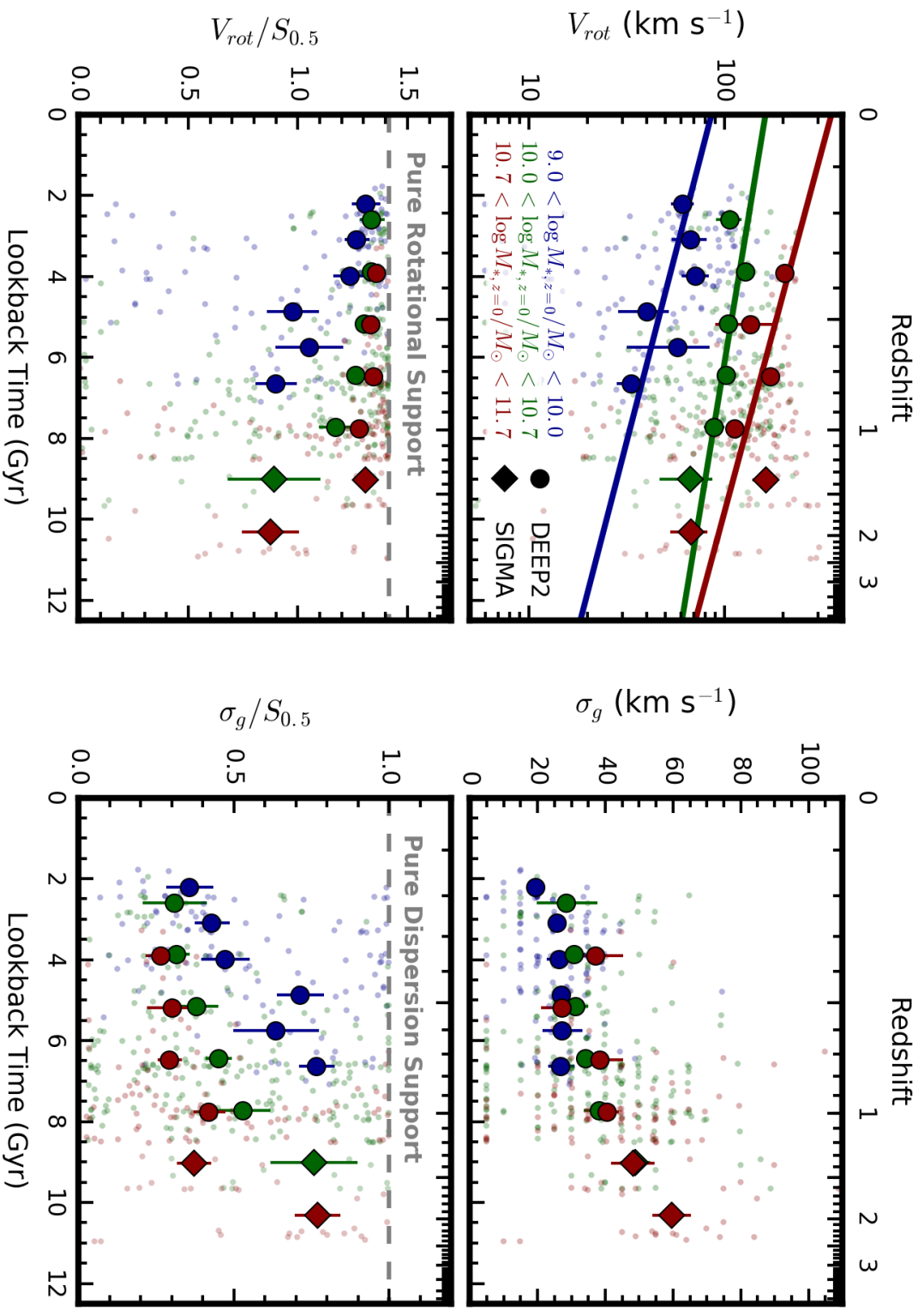

Figure 4.6: Caption on next page.

Figure 4.6: The same as Figure 4.2, but for galaxy populations linked in time via abundance matching. All galaxy populations on average spin-up and decrease in disordered motions with time, i.e., increase in V_{rot} and decline in σ_g. High mass galaxies reach a strong level of rotational support, i.e., $V_{rot}/S_{0.5} > 1.3$ and $\sigma_g/S_{0.5} < 0.4$, by $z = 1.5$ on average. Low and intermediate mass galaxies reach similar levels of rotational support several Gyrs later, at $z = 0.2$ and $z = 0.5$, respectively. The color scheme is the same as in Figure 4.5 with *dark* blue, green and red representing the low ($\log M_{*,z=0}/M_{\odot} \sim 9.4$), intermediate ($\log M_{*,z=0}/M_{\odot} \sim 10.3$) and high ($\log M_{*,z=0}/M_{\odot} \sim 11.1$) mass abundance matched populations, respectively. The small points are individual galaxies and the large points are the medians of the individual galaxies in bins of lookback time. The lines are the best-fit relations to the median points of each mass bin.

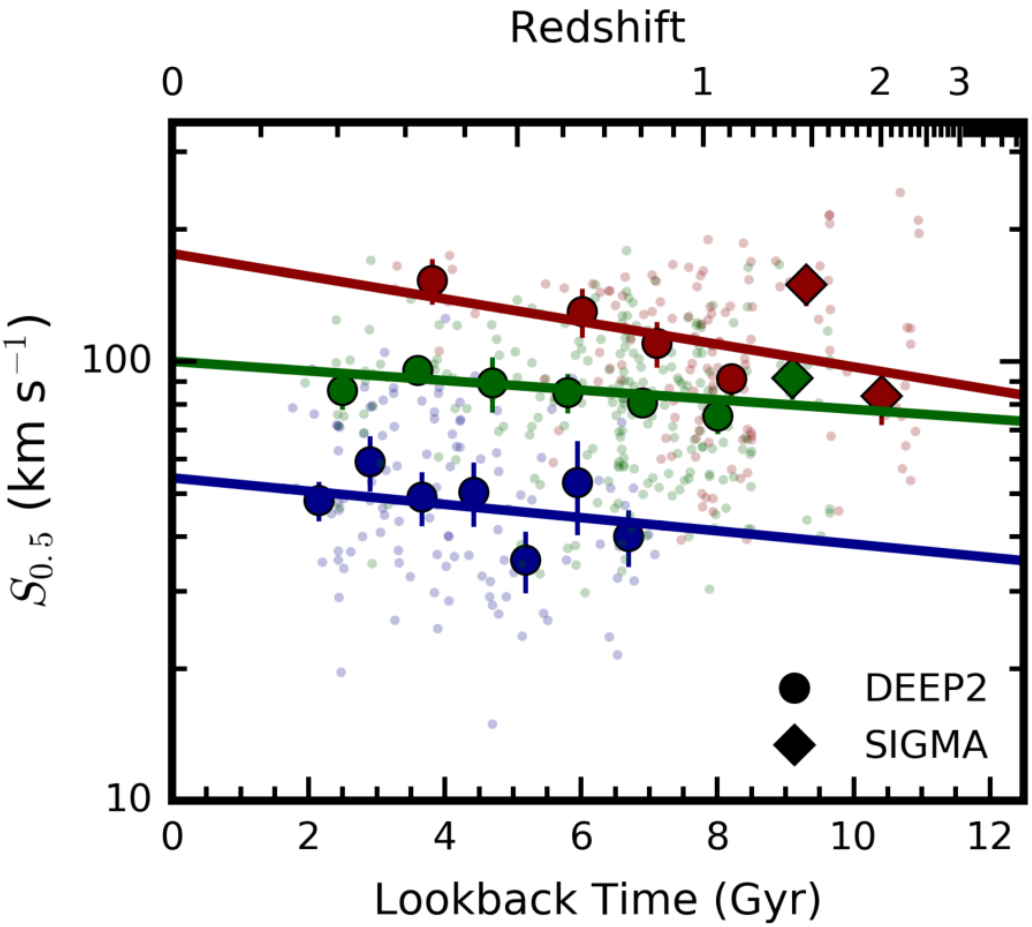

Figure 4.7: The same as Figure 4.3, but for galaxy populations linked in time via abundance matching. The quantity $S_{0.5}$ increases with time for all galaxy populations, indicating that their potential wells grow with time. The lines, points and color scheme are the same as in Figure 4.6.

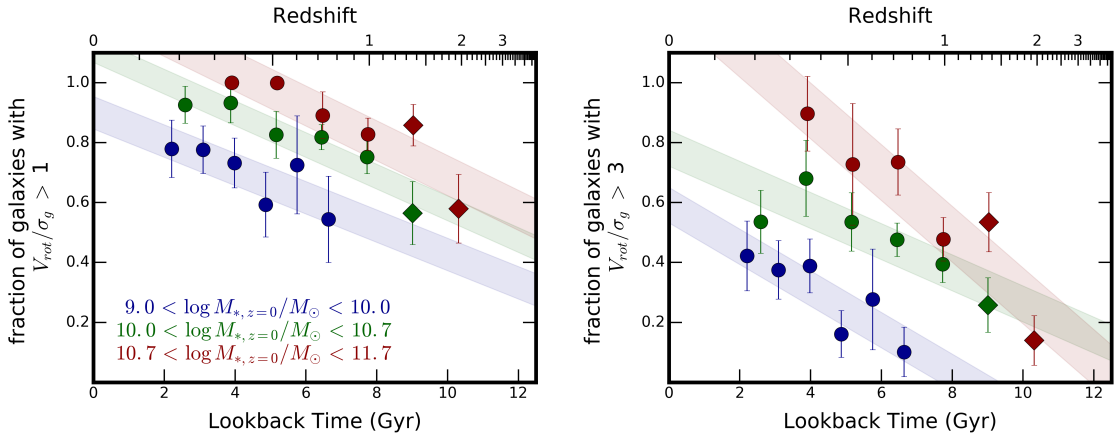

Figure 4.8: The same as Figure 4.4, but for galaxy populations linked in time via abundance matching. For all three galaxy populations (low, intermediate and high mass), the fractions of galaxies with $V_{rot}/\sigma_g > 1$ and 3 increase significantly with time. At any point in time, higher mass populations have a higher fraction of galaxies meeting these criteria. The fraction of galaxies with $V_{rot}/\sigma_g > 3$ drops below 30% at $z \sim 0.4$ for the low mass galaxy population (dark blue) and at $z \sim 1.5$ for the more massive galaxy populations (dark green and red). As in Figure 4.4, the solid points show measurements from DEEP2 (circles) and SIGMA (diamonds), and the error bars are from bootstrap resampling. The shaded swaths represent the uncertainties on the intercepts in linear fits to the points.

Chapter 5

Mergers Masquerading as Disks in High Redshift Observations of Galaxy Kinematics

The majority of massive star-forming galaxies at $z \sim 2$ are observed to have regular kinematic structure suggestive of disk-like rotation. However, the limiting spatial resolution of ground-based kinematic data presents an observational challenge — the orbital motions of merging galaxies are often indistinguishable from the regular ordered rotational motions of a disk.

In this chapter, to better understand and quantify this bias, we produce synthetic images and spectra of a suite of 34 zoom-in galaxy formation simulations. For each simulation snapshot, we determine if the synthetic data are consistent (or not) with

regular disk-like rotation and compare this result against the true state of the simulation, derived directly from the particle data. For both major and minor mergers, i.e., stellar mass ratios between 1 - 30, we find a large contamination of orbital motions to the observed rotation velocity — mergers are indistinguishable from disks in 40–80% of the observed sightlines at < 35 kpc separation. When both a disk and a merger are present, the derived rotation velocity is typically overestimated by a factor of $\sqrt{2}$ at close separation. If the intrinsic fraction of high redshift galaxies in close pairs and late-stage mergers is high, then these effects need to be accounted for when interpreting the observed disk fractions. Using theoretically-derived close pair fractions at $z = 2$, we determine that this effect is significant for low mass galaxies — up to a factor of 2 difference between observed and true disk fractions — but insignificant for high mass galaxies.

5.1 Introduction

The cosmic star-formation rate density peaks between $z = 1$ and $z = 3$ and marks a critical period for galaxy assembly (Madau & Dickinson, 2014). The processes thought to be most relevant for regulating the mass growth and structural transformation of galaxies at this time, e.g., stellar feedback, violent disk instabilities, cold mode accretion, minor/major mergers (Somerville & Davé, 2015), *may* also be dynamically disruptive, destroying ordered disk rotation on timescales comparable

to the dynamical time of the galaxy.

The fraction of high redshift galaxies harboring well-ordered disks thus provides a unique bellwether. A high value implies that early galaxy assembly is governed by dynamically calm processes, ones that are hospitable for disk formation and survival. A low value implies that early galaxy assembly is dominated by dynamically disruptive processes, those that tend to stall the formation and settling of well-ordered disks.

The internal kinematics of galaxies offer the most relevant observable for addressing this question — a disk galaxy will *at least* have higher ordered motions than random disordered motions, as quantified by rotation velocity V_{rot} and gas velocity dispersion σ_g, respectively.

Emission-line kinematics (i.e., of the ionized gas) has now been measured for several hundred star-forming galaxies at $1 \lesssim z \lesssim 3$ (e.g., Genzel et al. 2006; Förster Schreiber et al. 2006; Law et al. 2007; Kassin et al. 2007; Wright et al. 2007; Genzel et al. 2008; Shapiro et al. 2008; Law et al. 2009; Förster Schreiber et al. 2009; Lemoine-Busserolle & Lamareille 2010; Jones et al. 2010; Gnerucci et al. 2011; Swinbank et al. 2012; Law et al. 2012; Kassin et al. 2012; Contini et al. 2012; Newman et al. 2013b; Glazebrook 2013; Wisnioski et al. 2015; Mieda et al. 2016; Price et al. 2016; Olivares et al. 2016; Simons et al. 2016; Contini et al. 2016; Stott et al. 2016; Mason et al. 2017; Straatman et al. 2017; Turner et al. 2017b; Übler et al. 2017) — with samples that are large and representative enough to derive meaningful population statistics.

At $z = 2$, approximately 50% of low mass galaxies and 70% of high mass galaxies

have $V_{rot}/\sigma_g > 1$, i.e., more rotational-support than dispersion-support (Simons et al. 2017). Integral field spectroscopy (IFS), and the ability to map the velocity structure of galaxies in two dimensions, allows one to check for additional disk signatures. These include an alignment between the photometric and kinematic major axis and a spatial coincidence of a peak in the velocity dispersion with the kinematic major axis. Using the VLT/KMOS IFS, Wisnioski et al. (2015) find that ∼70% of massive galaxies at $z = 2$ have disk-like kinematic structure.

However, these observational signatures of disks — the appearance of regular rotation and rotation-dominated kinematics — are not necessarily *unique* to disks. In particular, the orbital motions from mergers and close pairs, once convolved with the typical observational seeing-limit at $z = 2$ (∼0.″7 or 6 kpc), can mimic the regular ordered rotational motions of a disk. While techniques have been developed for distinguishing these cases (e.g., `Kinemetry`, Krajnović et al. 2006), they typically require high-resolution and high-S/N data (e.g., Shapiro et al. 2008). Using a set of artificially-redshifted local mergers and synthetic observations of idealized binary merger simulations, Hung et al. (2015, 2016) demonstrate that the ability to distinguish between disks and mergers depends strongly on the interaction phase, becoming progressively more difficult during later stages. Merger rates and close pair fractions increase with increasing redshift (Lotz et al., 2011; Rodriguez-Gomez et al., 2015; Mantha et al., 2018), meaning that this observational degeneracy becomes increasingly important to the derived disk fractions at higher redshifts.

In this chapter, we seek to quantify the contamination of mergers in high redshift observations by using synthetic observations of a suite of realistic zoom-in hydrodynamic simulations. We adopt 19 camera sight lines around each simulated galaxy to quantify the stochasticity of individual sight lines.

The chapter is structured as follows. In §2 we describe the simulation suite used in this study. In §3 we use the angular momentum profiles to identify galaxy pairs and characterize the intrinsic dynamical properties of the simulated galaxies. In §4 we use the `SUNRISE` dust-radiative transfer program to generate mock observations of the simulations. In §5, we measure photometric properties from the synthetic imaging and kinematic properties from the synthetic spectra. In §6 we compare the interpretations from the synthetic data against the intrinsic dynamical state of the simulation suite. In §7 we discuss implications for the observed disk fractions at high redshift and in §8 we summarize our conclusions. We adopt a ΛCDM cosmology defined with $(h, \Omega_m, \Omega_\Lambda) = (0.7, 0.27, 0.73)$.

5.2 Simulation Suite

We analyze a set of 34 cosmological zoom-in galaxy formation simulations from the VELA simulation suite (Ceverino et al., 2014; Zolotov et al., 2015). The simulations are briefly reviewed here and Ceverino et al. (2014) is refereed to for further details.

The simulations were run with the N-body and Eulerian gas dynamics Adaptive

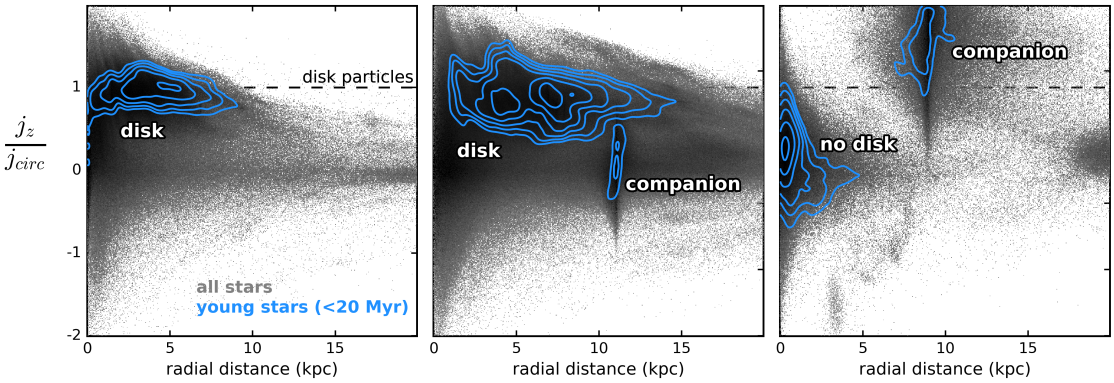

Figure 5.1: The intrinsic state of the simulated galaxies, i.e., disk, merger, disk+merger, is determined directly from the star particle data. The distribution of the total stellar mass (grey) and the young stellar mass (blue contours) in j_z/j_{circ} versus 3D radial distance is shown for three simulation snapshots. The quantity j_z/j_{circ} measures the alignment of a star particle's angular momentum to the net angular momentum of the galaxy. Particles in a disk lie at $j_z/j_{circ} = 1$ (dashed black line), i.e., on circular orbits that are co-rotational with the net angular momentum. The 3D radial distance is measured from the center of the central most massive galaxy. This diagram is used to check whether the central galaxy has a disk and to identify any nearby companions. The three examples include a disk galaxy (left panel), a disk galaxy with a companion (middle panel), and a galaxy without a disk and with a companion (right panel).

Refinement Tree code (ART, Kravtsov et al. 1997), including subgrid recipes for: gas and metal cooling, UV-background photoionization, stochastic star formation, gas recycling and metal enrichment from stellar winds, thermal feedback from supernovae and feedback from young stars through radiation pressure and radiative heating (Ceverino et al., 2010, 2012, 2014). The maximum resolution of the adaptive mesh grid is between 17 and 35 physical parsecs. The simulated galaxies have stellar masses spanning $9.3 < \log M_*/M_\odot < 10.7$ at $z = 2$. This is comparable to the typical stellar mass range of seeing-limited kinematics samples in the literature at this redshift (e.g., Wisnioski et al. 2015; Simons et al. 2016). This simulation suite has been used in previous papers to study the structural characteristics of high redshift galaxies, including their elongation (Ceverino et al., 2015; Tomassetti et al., 2016), compact stellar structure (Zolotov et al., 2015; Tacchella et al., 2016a,b), and clumpy morphologies (Mandelker et al., 2014; Moody et al., 2014; Inoue et al., 2016; Mandelker et al., 2017).

The subset of simulations analyzed in this paper span $1 < z < 3$ and are separated in equal intervals of scale factor $\Delta a = 0.01$, corresponding to a time interval of 110 Myr at $z = 3$, 125 Myr at $z = 2.0$ and 160 Myr at $z = 1.0$.

5.3 Intrinsic State of the Simulated Galaxies

The objective of this paper is to compare the *truth* of the simulations with the interpretation one would reach from mock observations of them. The intrinsic properties of the galaxies are measured directly from the simulation data. 3D positions and velocities of star particles and gas cells are recorded at each simulation snapshot. This information is used to (i) determine if the most massive galaxy in the simulation box, hereafter referred to as the 'central galaxy', has a rotationally-supported star-forming disk and (ii.) identify all galaxies that are nearby the central galaxy, hereafter referred to as 'companion galaxies'. As follows, each simulation snapshot is categorized into one of the following:

1. isolated central galaxy with a disk
2. central galaxy with a companion and no disk
3. central galaxy with a companion and a disk

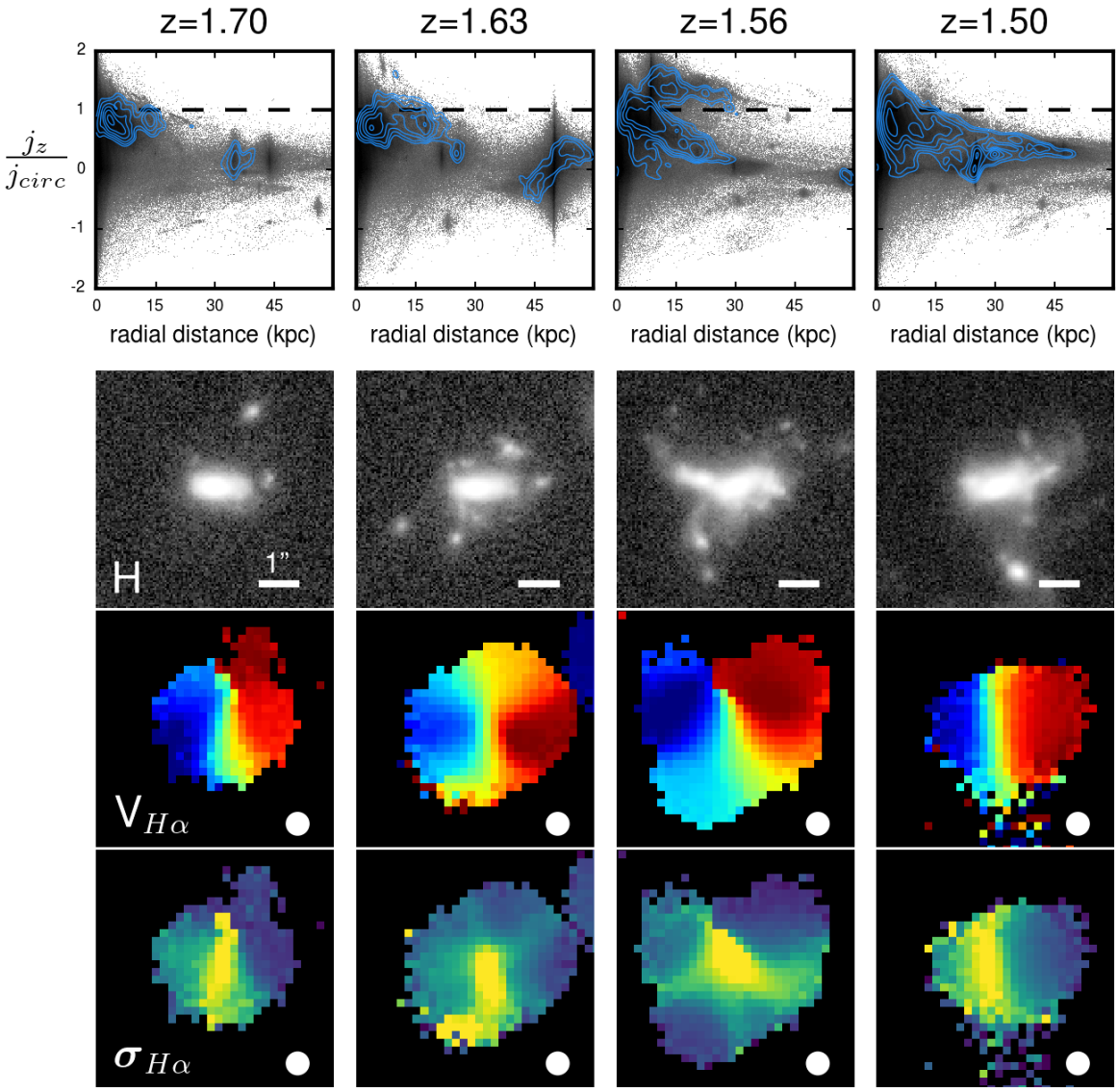

Figure 5.2: Mock observations of a simulated merger over time. The position of the camera is fixed in space from snapshot to snapshot. The mocks include the *HST*/WFC3 F160W H-band image (second row), the VLT/KMOS velocity and the VLT/KMOS velocity dispersion map (third and fourth row).

5.3.1 Checking Whether the Central Galaxy has a Disk

To determine whether the central galaxy has a star-forming disk, we examine the motions of its young star particles. In a disk galaxy, stars will tend to have orbital motions aligned with the net galaxy rotation, while in a dispersion-supported galaxy they will have no preferred orbital direction.

The direction of the net angular momentum of the central galaxy ($\hat{z} = \vec{J}_{gal}/J_{gal}$) is defined using an iterative fit of a cylindrical disk to the cold gas component ($T < 1.5 \times 10^4$ K; see appendix of Mandelker et al. 2014 for details). To assess the alignment of each star particle's orbit with the net galaxy rotation, we adopt the circularity parameter j_z/j_{circ} (e.g., Scannapieco et al. 2010; Sales et al. 2012). The quantity j_z is the component of a particle's specific angular momentum aligned with the net angular momentum of the galaxy. The quantity j_{circ} is the specific angular momentum of a theoretical circular orbit at the particle's position, irrespective of the orbital direction, and is calculated from the total mass inside of a shell at that position, $j_{circ}(r) = r\, v_{circ}(r) = \sqrt{r\, M(<r) G}$, where spherical symmetry is assumed for simplicity.

The circularity parameter is calculated for every star particle in the simulation box. Those particles associated with a disk lie near $j_z/j_{circ} = 1$, i.e., on circular orbits aligned with the net rotation of the galaxy. In a dispersion-supported system, star particles are distributed symmetrically around $j_z/j_{circ} = 0$.

Galaxy kinematics at high redshift are almost exclusively measured from emission lines, tracing the star-forming regions of galaxies. For an appropriate comparison to the observations, we search for disks in the simulated galaxies using only their young stars. For each timestep of each simulation, we calculate the mean circularity of the young star particles — those less than 20 Myr old — that are associated with the central galaxy.

Galaxies are determined to host a disk if $(j_z/j_{circ})_{young} > 0.8$, i.e., the young stars are strongly rotation-supported, and to not host a disk if $(j_z/j_{circ})_{young} < 0.3$, i.e., the young stars are strongly dispersion-supported. For simplicity, galaxies intermediate to these two cases are ignored. We emphasis that this classification applies only to their young stellar component — the older stars are typically more dispersion-supported (Figure 5.1).

5.3.2 Checking Whether the Central Galaxy has a Companion

Companion galaxies are identified using the joint distribution of stars in radial position and j_z/j_{circ} (Figure 5.1). External galaxies appear as a distinct cluster of points in this plane, i.e., their stars are close to one another in space and are traveling on similar trajectories.

For each simulation snapshot, a segmentation procedure is run on this 2D dis-

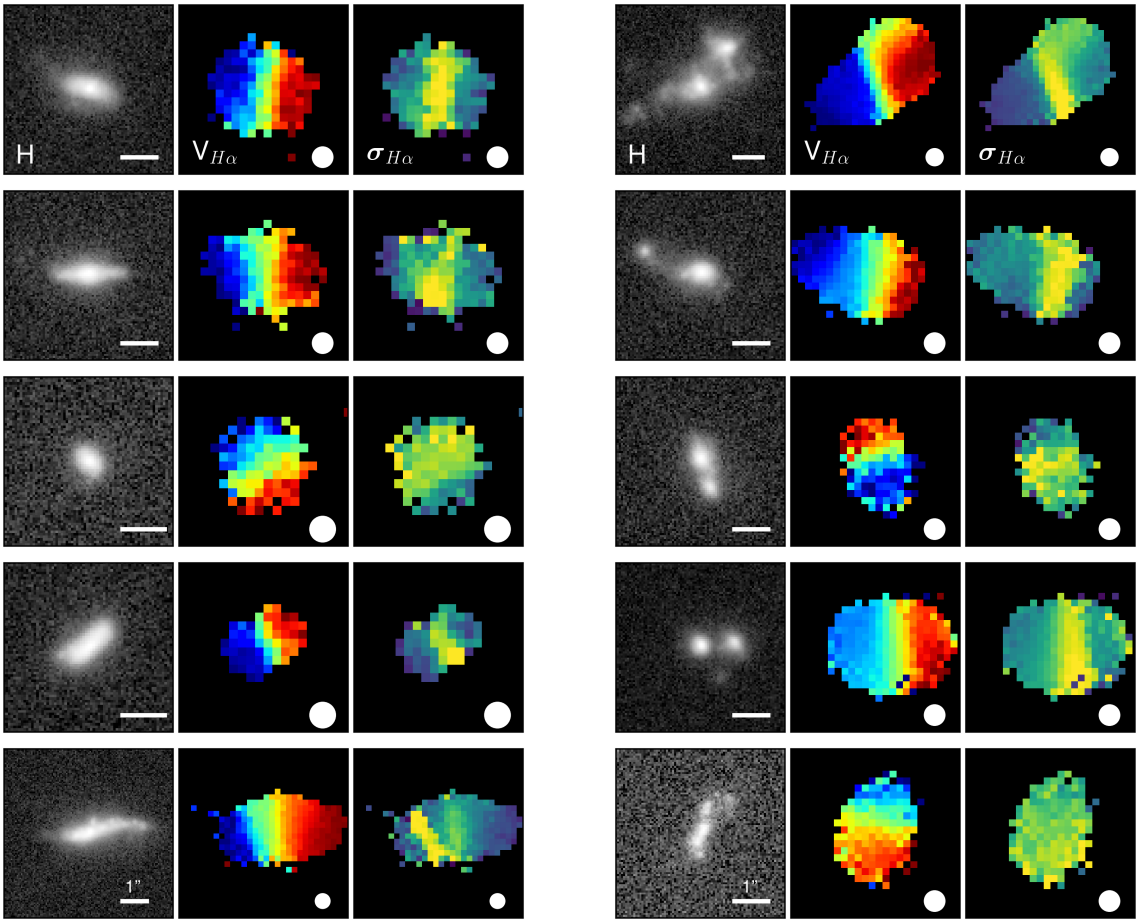

Figure 5.3: Mock *HST*/WFC3 H-band images and VLT/KMOS Hα velocity maps are shown for isolated disk galaxies (left) and merging systems without disks (right). The intrinsic states were determined directly from the young star particles, as described in Figure 5.1. The orbital motion associated with the merger is indistinguishable from the rotation signature of the disk due to seeing: the velocity gradient is smooth and monotonic, the kinematic major axis is coincident with the photometric major axis and the velocity difference across the map exceeds the average velocity dispersion. Without considering the disturbed morphology of the *HST* image, the merging systems on the right would be classified as disks. The size of the simulated ground-based seeing, used for smoothing the KMOS cube, is 0.″6 and is shown by the white circle.

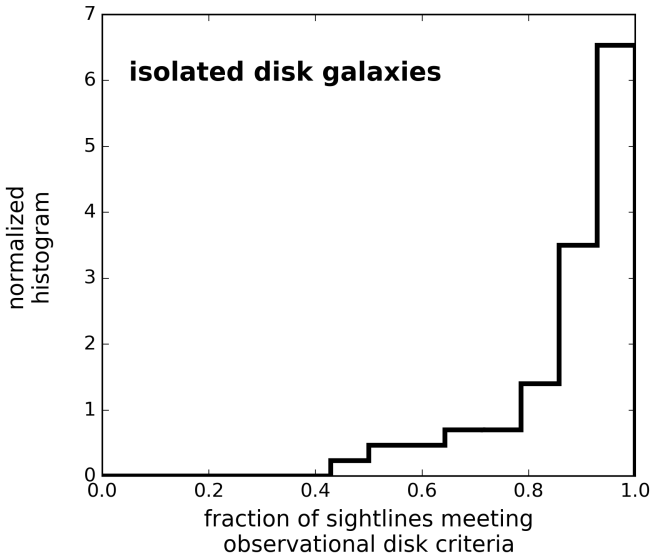

Figure 5.4: The fraction of camera sightlines meeting the observational disk criteria for simulation snapshots with a central disk and no nearby galaxy.

tribution to detect significant clusters of star particles. The segmentation procedure iterates until the number of detected objects does not change with an increasing clipping level. A detection threshold is set at a stellar mass of 10^6 $M_\odot$ to prevent spurious detections. Once this procedure is complete, each star particle in the simulation is associated with a unique galaxy.

We characterize the position and mass of all galaxies detected within 100 kpc of the central galaxy. Companion galaxies are defined to be those sufficiently close to the central galaxy (3D seperation < 35 kpc) and sufficiently massive (stellar mass ratio with the central less than 30). As such, we include both major and minor galaxy pairs.

5.4 Synthetic Observations of the Simulations: images and spectra

To generate synthetic observations, each simulation snapshot is post-processed with the dust radiative transfer software SUNRISE (Jonsson, 2006; Jonsson et al., 2010; Jonsson & Primack, 2010). Mock images and spectra are created from the SUNRISE output.

5.4.1 Dust Radiative Transfer with SUNRISE

The ART data is first loaded into the analyses software YT (Turk et al., 2011) and converted into the appropriate SUNRISE format. This is carried out using an updated version of the pipeline described in Moody et al. (2014).

SUNRISE contains two primary steps: (i.) generate a spectral energy distribution (SED) for each source of radiation in the simulation and (ii.) propagate the associated polychromatic rays through a 3D gas grid, taking into account dust absorption and scattering, towards a user-defined camera(s).

An SED is assigned to each star particle based on its age, mass, and metallicity using STARBURST99 (Leitherer et al., 1999) assuming a Kroupa (2001) initial mass function. Emission lines are generated from young star particles, less than 10 Myrs old, using a starburst model from the photoionization and shock modeling code MAPPINGS III (Dopita et al., 2005; Groves et al., 2008). This model includes a central

massive young stellar cluster, whose SED is set with `STARBURST99`, a surrounding HII region, and a photodissociation region with a covering fraction of 0.2 (Groves et al., 2008). To account for 10^4 K thermal broadening, we convolve the original `MAPPINGS III` Hα emission line with a 10 km s^{-1} 1D Gaussian kernel.

The dust density is assumed proportional to the gas metal mass using a dust-to-metals mass ratio of 0.4 (Dwek 98). Consequently, the dust geometry is resolved to the typical gas cell size $\sim$17-35 pc. We adopt the dust grain size distribution from Weingartner & Draine (2001) and Draine & Li (2007) with $R_v = 3.1$, equivalent to the value for the Milky Way (e.g., Gordon et al. 2003).

`SUNRISE` cameras are placed at 19 different positions around the galaxy. Of these, 6 are random but remain fixed over time, 8 are random but change from timestep to timestep, and the remaining 5 are fixed to the galaxy and, as such, change from timestep to timestep. Those fixed to the galaxy include one which is face-on, i.e., along the gas angular momentum axis, one which is reverse face-on, two which are edge-on, and one which is placed at a 45° angle from face-on. These 19 sightlines allow us to overcome the intrinsic randomness associated with a single viewing angle.

We run the radiative transfer step of `SUNRISE` twice, once in a mode suitable for creating broadband images and once in a mode suitable for creating high-resolution spectra. A sufficient number of polychromatic rays are used for both runs, 10^7, to overcome Monte Carlo noise.

In the first mode, `SUNRISE` is run at low spectral resolution but with coverage over

the NUV–NIR (0.02 – 5 μm). Each camera contains 800 x 800 pixels and covers a physical FOV of 100 kpc. The output spectral cube is integrated over the spectral response function of the far-UV through IR filters available with *HST*/ACS–WFC3, taking into account the redshift of the simulation and the corresponding cosmological Doppler shift and surface brightness dimming of the SED.

In the second mode, `SUNRISE` is run at high spectral resolution around the Hα emission line (0.65 – 0.66 μm). The camera contains 400 x 400 pixels and also covers a physical FOV of 100 kpc. The pixel-by-pixel surface brightness in the resulting `SUNRISE` cube is scaled with redshift to account for cosmological surface brightness dimming.

This process is repeated for each snapshot of each galaxy simulation. The final suite contains thousands of idealized UV–IR band images and idealized spectral cubes around the $H\alpha$ emission line.

5.4.2 Mock HST/WFC3 imaging

Following Snyder et al. (2015), the idealized images are degraded in noise and spatial resolution to match the observing conditions of the CANDELS–Wide *HST* multi-cycle treasury survey (Grogin et al. 2011, Koekoemer et al. 2012). The angular sizes and fluxes of the pixels are scaled with the angular size distance and luminosity distance of the simulation redshift. The images are convolved with the typical point-spread function of the instrument/filter and the pixel size is rebinned to

the instrumental pixel scale (e.g., 0.″6 pixel^{-1} for *HST*/WFC3). Finally, shot noise is added to the image to simulate the background noise of CANDELS-Wide.

In this chapter, we use the mock *HST*/WFC3 F160W image (H-band), tracing the ∼rest V-band at z = 1 and the I-band at z = 3.

5.4.3 Mock VLT/KMOS Integral Field Spectroscopy

The idealized high spectral resolution cube from `SUNRISE` is degraded to the surface brightness depth, spectral and spatial resolution of typical ground-based seeing-limited data. The majority of the large IFS kinematics surveys at $1 \lesssim z \lesssim 3$ are performed with the KMOS near-infrared spectrograph on the VLT, e.g., KMOS-3D (Wisnioski et al., 2015), KROSS (Stott et al., 2016), KDS (Turner et al., 2017b). For an apt comparison with the literature, we use the specifications of this instrument to generate the mock spectra. We emphasize, however, that our conclusions are general to all seeing-limited instruments/surveys.

The physical pixel size of the `SUNRISE` cube is 0.25 kpc px^{-1} and the corresponding angular scale is determined from the simulation redshift. Each spectral slice of the cube is blurred with a 2D Gaussian of 0.″6 FWHM to simulate the typical atmospheric seeing in the NIR. The pixels are rebinned to 0.″2, the angular pixel scale of KMOS, and the spectral dimension is convolved with a 1D Gaussian of $R = \Delta\lambda/\lambda = 3800$ to simulate the KMOS spectral resolution. Finally, shot noise is added to each pixel to reach a typical 5σ point source depth of 24 AB magnitudes, equivalent to a typical 8

hour exposure with KMOS.

Although we aim to simulate realistic ground-based observations, we do not include sky lines and ignore that the sky is opaque for Hα at $1.8 < z < 2.2$. These assumptions do not affect the conclusions of this chapter.

5.5 Measurements from the synthetic observations

5.5.1 Inclination and Photometric Position Angles

Photometric properties — inclinations and position angles — are derived from the synthetic *HST* H-band images. Unique sources in each image are identified and characterized using the `Photutils` package of Astropy (Astropy Collaboration et al., 2013), with the requirement that at least 5 connected pixels have a flux that exceeds the background rms.

Each image is centered on the central galaxy and so we select the central source as the main target. The ratio of the isophotal semi-major and semi-minor axis, a and b, respectively, is used to determine the inclination, as $\cos^2 i = ((b/a)^2 - q_0^2)/(1 - q_0^2)$. We adopt a value of $q_0 = 0.25$, the standard literature assumption for a thick disk. The photometric position angle is defined as the direction of the semi-major axis.

5.5.2 Kinematics

The line-of-sight velocity and velocity dispersion are measured for each spaxel of the synthetic KMOS cube. A 1D Gaussian profile is fit to the $H\alpha$ emission line with the width, amplitude and center as free parameters in the fit. The center of the best-fit profile is taken as the mean line-of-sight velocity. The velocity dispersion is taken from the RMS width of the best-fit after subtracting the spectral resolution of the instrument in quadrature ($\sigma(R) = \sigma_{measured} - \sigma_{instrument}$). This is repeated for all spaxels, resulting in 2D maps of velocity and velocity dispersion. Examples of these kinematic maps are shown in Figure 5.2.

The kinematic major axis is defined as the line intersecting the the centroid of the pixels with the maximal and minimal 10% velocities, V_{max} and V_{min}, respectively. A 3-spaxel wide slit is placed along the kinematic major axis. The rotation curve and velocity dispersion profile is measured along this slit by averaging the velocity and dispersion of the included spaxels.

The rotation velocity uncorrected for inclination, $V_{rot} \times \sin i$, is taken as the difference between the maximum and minimum velocities of the rotation curve. This is then inclination-corrected using the best-fit axis ratio of the *HST*/WFC3 H-band image:

$$V_{rot} = \frac{V_{max} - V_{min}}{\sin i} \tag{5.1}$$

The seeing will tend to smear unresolved velocity gradients and artificially elevate

the velocity dispersion in the centers of galaxies, where the rotation curve is steepest (see Fig. 9 of Weiner et al. 2006a). To avoid the effects of beam smearing, we assume that velocity dispersion is constant across the face of the galaxy and measure its intrinsic value using the average uncertainty-weighted mean of the velocity dispersion profile on the galaxy outskirts, i.e., those at and beyond the maximal and minimal 10% velocities (typically near $\sim$1.5 $\times$ effective radius).

5.5.3 Criteria for classifying a galaxy as a disk

Following Wisnioski et al. (2015), we classify the observations along each sightline as 'disk-like' if they exhibit the following kinematic and morphological signatures:

1. the velocity map exhibits a continuous velocity gradient along a single axis
2. $V_{rot}/\sigma_g > 1$, i.e., the inclination-corrected rotation velocity exceeds the velocity dispersion
3. the position of the steepest velocity gradient is coincident with a peak in the velocity dispersion map
4. the photometric and kinematic axes are aligned within 30 degrees
5. the steepest velocity gradient is coincident with the centroid of the continuum center

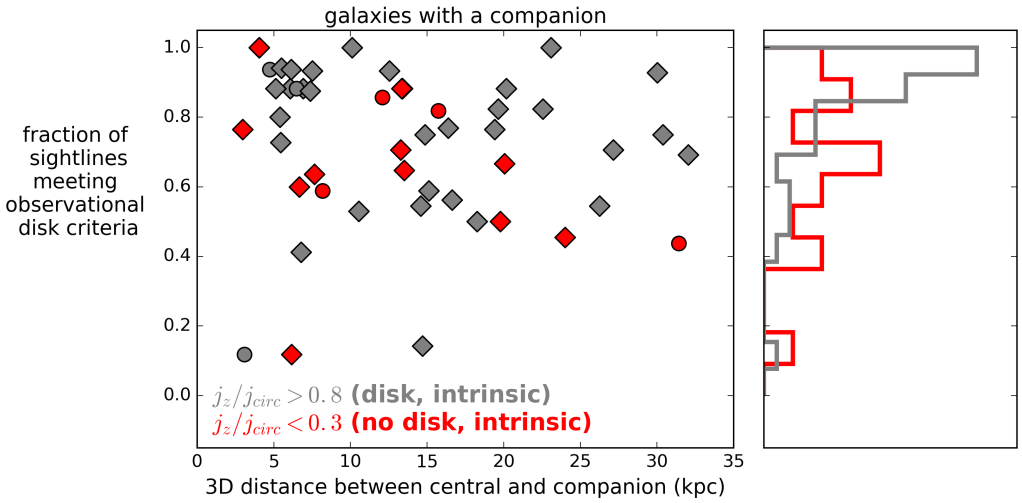

Figure 5.5: The fraction of camera sightlines meeting the observational disk criteria for simulations in which the central galaxy has a nearby companion, less than 30 kpc in 3D separation. Simulations in which the central galaxy is intrinsically rotationally-supported are shown in grey, while those that are intrinsically dispersion-supported are shown in red. More than 50% of dispersion-dominated galaxies with close companions pass the disk criteria — the orbital motions of late-stage mergers are masquerading as the rotational motions of disks.

5.6 Merger-Disk Degeneracy in Resolved Kinematic Maps

5.6.1 Synthetic Observations of a Single Simulated Merger

We first examine the synthetic observations of a single simulation, namely VELA20. The central galaxy in the simulation box merges with a slightly less massive companion galaxy at z = 1.6. Prior to their encounter, the stellar mass of the central and companion are 4.1 $\times 10^{10}$ $M_{\odot}$ and 1.2 $\times 10^{10}$ $M_{\odot}$, respectively, qualifying this as a major merger. We follow 4 timesteps before and after the first collision, each separated by 150 Myr. The angular momentum profile, synthetic *HST*/WFC3 H-band image, and synthetic VLT/KMOS velocity and velocity dispersion maps are shown for each timestep in Figure 5.2.

Over the first two snapshots, $1.6 < z < 1.7$, the central galaxy has a rotationally-supported star-forming disk (Figure 5.2; top left) — the young star particles are distributed near $j_z/j_{circ} = 1$ and extend out to 15 kpc from the galaxy center. As expected, the Hα velocity and velocity dispersion maps reflect this ordered rotation (Figure 5.2; bottom left) — the primary velocity gradient is smooth and continuous, the kinematic and photometric axes are aligned, the velocity dispersion map peaks near the center of the steepest velocity gradient, and the inclination-corrected rota-

tion velocity (345 ± 11 km s^{-1}) exceeds the typical velocity dispersion (61 ± 7 km s^{-1}). This galaxy would be classified as a disk using the observational disk criteria, illustrating the success of the criteria when applied to isolated galaxies.

The observations are significantly more challenging to interpret during the first interaction, which occurs at $z = 1.56$. Before and during the merger, the central galaxy retains its rotationally-supported disk and the orbital direction of the merger is aligned with the rotational direction of the disk (top panel). At the time of collision, the maximum velocity of the velocity map, i.e., the reddest component, traces the rotational signature of one side of the disk, while the minimum velocity of the velocity map, i.e., the bluest component, traces the orbital motion of the companion galaxy. When taken together, these two define the kinematic major axis, i.e., the direction between the maximum and minimum velocities. Instead of tracing the rotational motion of the disk — which is still present in the map — the kinematic major axis follows the velocity gradient defined by one edge of the disk and the companion galaxy. This measurement has significantly less physical meaning than either the rotation velocity of the disk or the relative velocity between the two galaxies.

Even still, the velocity map is consistent with rotational motions of a disk — the velocity gradient between the maximum and minimum velocity is smooth and continuous and velocity dispersion peaks along the steepest observed gradient.

The line-of-sight velocity difference between the edge of the disk and the merger is 546 km s^{-1}, while the line-of-sight velocity difference of the disk is 358 km s^{-1}. As

such, a measurement of $V_{rot} \times \sin i$ along the kinematic major axis overestimates the true rotation velocity of the disk by a factor of 1.5 or 0.18 dex. This is comparable to the $\sqrt{2}$ difference between the escape velocity and circular velocity and is comparable in magnitude to to the observed evolution of the Tully-Fisher relation at $z = 2$ (Turner et al., 2017a).

In this example, the galaxy is sufficiently large, 25 kpc or 3″, compared to the size of the ground-based seeing, 0.6", that the complicated kinematic signatures of the merger are apparent in the velocity maps, specifically that there are two distinct velocity gradients in the map. As follows, we examine cases where the galaxy is less resolved in the seeing-limit.

5.6.2 Contamination to the observed disk criteria, mergers masquerading as disks

We now examine the full suite of simulations. For each simulation snapshot, two classifications are considered: those where the central galaxy has a nearby companion and those where the central galaxy is isolated. For the purposes of analyzing clean and distinct samples, simulation snapshots intermediate to these cases are neglected.

For a galaxy to be considered a companion of the central galaxy it must meet the following two criteria: it is nearby, with a 3D separation less than 35 kpc, and sufficiently massive, with at least $\times 1/30$th the stellar mass of the central galaxy.

A central galaxy is considered isolated if it meets the following two criteria: there are no galaxies with a stellar mass ratio <100 within 75 kpc and it did not have a companion galaxy in the previous snapshot. The second criteria ensures that we do not include galaxies that experienced a merger within the past $\sim$ 150 Myrs.

In the left panel of Figure 5.3, we show synthetic data for example isolated disk galaxies. All of these examples exhibit regular morphological and kinematic properties — hallmark signatures of a disk. Indeed, of the galaxy snapshots with a rotationally-supported young stellar disk $(j_z/j_{circ})_{young} > 0.8$, the observational disk criteria work with high confidence (Figure 5.4). In nearly 90% of these cases, the galaxy snapshot is successfully identified as a disk in at least 80% of the sight lines.

In the right panel of Figure 5.3, synthetic data is shown for examples of dispersion-supported galaxies with nearby companions. The synthetic data exhibit the same characteristics that we would expect for disk galaxies: the velocity gradient is smooth and continuous, the velocity dispersion peaks in the center of the steepest velocity gradient (bottom panel is the exception), and the photometric axis is coincident with the kinematic axis.

5.6.3 Contamination as a Function of 3D Pair Separation

In Figure 5.5, we show the fraction of sightlines meeting the disk criteria for each snapshot of each galaxy. We consider only those galaxies with a close companion and categorize the central galaxy in one of two kinematic states: "disk" with $(j_z/j_{circ})_{young} > 0.8$ and "no disk" with $(j_z/j_{circ})_{young} < 0.3$. The fraction is shown as a function of the 3D separation between the two galaxies.

At close passage, < 20 kpc, more than 60-100% of camera sight lines with *no intrinsic disk* are classified as disks from the disk criteria. We note a slight decline in this fraction with increasing 3D separation. For galaxies with companions at larger separation ($\sim 20 - 30$ kpc), this number declines to $40 - 60\%$.

Dispersion-dominated galaxies with nearby companions are typically misclassified as disks in the kinematic data because: (i) the orbital motion of the merger draws the kinematic major axis while simultaneously satisfying $V_{rot}/\sigma_g > 1$, where V_{rot} in this case is actually the line-of-sight orbital motion of the merger, (ii) during close passage, or for sight lines where the galaxies have a small projected separation, the photometric major axis in the *Hubble* image is also drawn to the galaxy-galaxy axis and (iii) the central peak in the velocity dispersion results from the steep velocity step-function midway between the two galaxies, i.e., beam smearing of the orbital motions.

For galaxies with a disk, we find significant scatter to low f_{disk} — galaxies are being misclassified as non-disk from the disk criteria. This is largely due to the misalignment between the photometric position angle and the kinematic position angle.

5.7 Quantifying the Effect of Mergers on Measurements of Disk Fractions at High Redshift

We have demonstrated that, due to seeing, galaxies with a nearby companion and no disk can display the same kinematic signatures as that expected from disks — i.e., regular velocity field, alignment between the photometric and kinematic axis, $V_{rot}/\sigma_g > 1$, velocity dispersion peak that is coincident with the kinematic major axis. In this section, we attempt to quantify the scale of this effect on real observations.

To do this, one must know the fraction of star-forming galaxies with companions at $r \lesssim 30$ kpc. Mantha et al. (2018) find that the fraction of massive galaxies ($M_*/M_\odot > 2 \times 10^{10}$) with major nearby companions (4:1 mass ratio; 5-50 kpc projected separation) increases with redshift, to $\sim$15% at $z \sim 1$, before beginning to decline.

As an important aside — given that the kinematic maps are luminosity-weighted, the appropriate statistic is the $H\alpha$-flux pair fraction — i.e., companion galaxies that

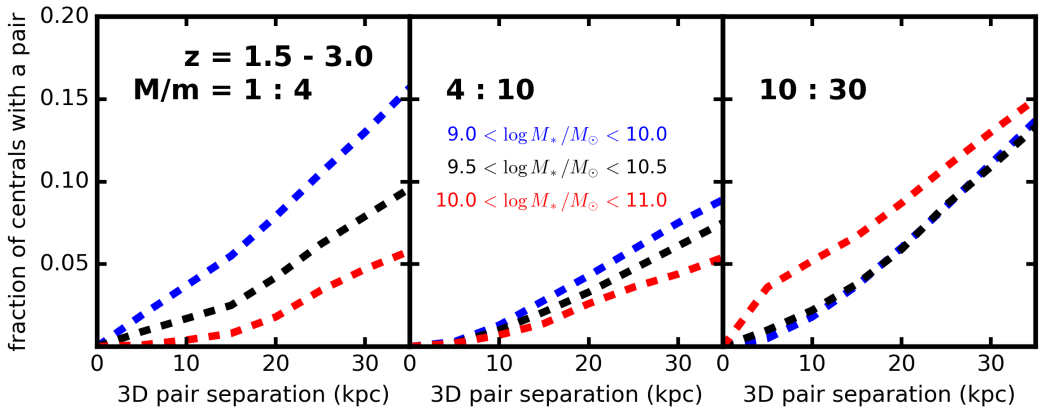

Figure 5.6: The fraction of central galaxies with a companion closer than a given 3D separation, measured from the Illustris simulations at $1.5 < z < 3.0$. Three overlapping bins in central stellar mass are shown — 10^{9-10}M$_\odot$ (blue), $10^{9.5-10.5}$M$_\odot$ (black), 10^{10-11}M$_\odot$ (red). These cover the typical stellar mass ranges of kinematic samples in the literature. Three bins in mass ratio between central and satellite are shown – 1:4 (i.e., major pairs; left), 4:10 (i.e., minor pairs; middle), and 10:30 (i.e., very minor pairs; right). These will be used to estimate the correction to the observed fraction of galaxies with disks.

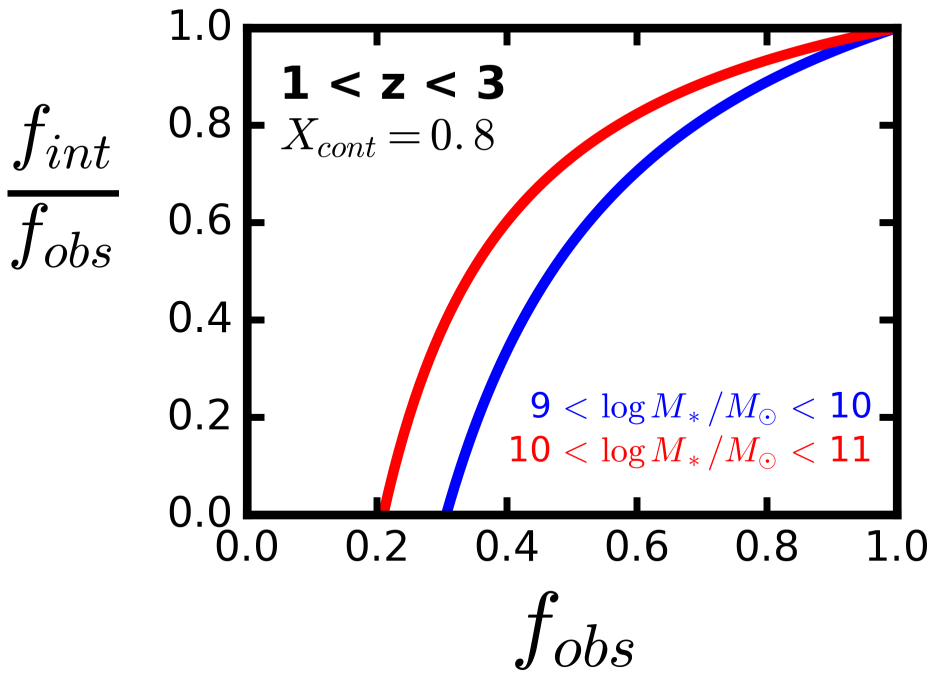

Figure 5.7: Toy-model conversion between observed disk fraction f_{obs} and true disk fraction f_{int} at $1 < z < 3$ using pair fraction estimates from Illustris (Figure 5.6) and assuming 80% of companions separated by < 35 kpc will masquerade as disks (as found in Figure 5.5). The correction is smaller for high mass ($M_* = 10^{10-11}$ $M_\odot$) galaxies than it is for low mass galaxies ($M_* = 10^{9-10}$ $M_\odot$).

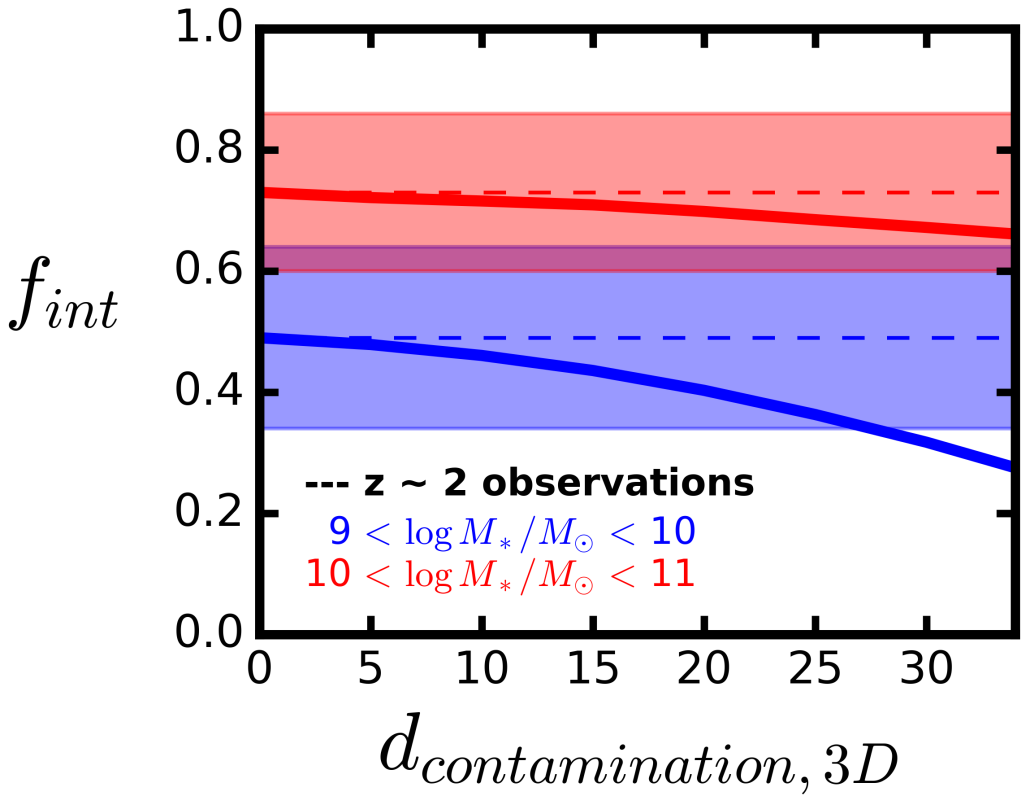

Figure 5.8: The difference between observed disk fraction f_{obs} (dashed line) and true disk fraction f_{int} (solid line) at $1 < z < 3$ as a function of $d_{contamination,3D}$, i.e., the minimum 3D distance that a hypothetical observer can separate disks from mergers. This uses pair fraction estimates from Illustris (Figure 5.6) and assumes 100% of companions separated by less than $d_{contamination,3D}$ kpc will masquerade as disks. Observed values at $z \sim 2$, f_{obs} are shown from (Simons et al., 2017). The uncertainty on f_{obs} is shown with the shaded region.

have sufficiently strong $H\alpha$ emission to contaminate the velocity of a spaxel. It is not straightforward to convert between a mass ratio-selected pair fraction and an Hα ratio-selected pair fraction. For instance, Mantha et al. 2018 find that ∼20% of galaxies qualify as a major pair at $z \sim 3$ when selecting by H-band flux ratio (4:1 flux ratio), while only 5% qualify when selecting by stellar mass ratio (4:1 mass ratio).

5.7.1 The Fraction of Central Galaxies with a Companion in the Illustris Simulation

In lieu of using observed pair fractions (e.g, Mantha et al. 2018), which are subject to incompleteness limits at low stellar masses, we use results from the (106.5 Mpc)^3 Illustris cosmological galaxy formation simulation box (Genel et al., 2014; Vogelsberger et al., 2014). Pair fractions are measured from realistic mock lightcones in Snyder et al. (2017) — we refer to this paper for details.

Cumulative pair fractions at $1.5 < z < 3$ are shown in Figure 5.6 using the mock Illustris lightcone catalog. These are broken into three bins of stellar mass: $9 < \log \mathrm{M}_*/\mathrm{M}_\odot < 10$ (i.e., low mass), $9.5 < \log \mathrm{M}_*/\mathrm{M}_\odot < 10.5$ (i.e., intermediate mass), and $10 < \log \mathrm{M}_*/\mathrm{M}_\odot < 11$ (i.e., high mass). We split them three further bins in stellar mass ratio (i.e., mass ratio between the central and companion galaxy): 4:1 (i.e., major pair), 4:10 (i.e., minor pair), and 10:30 (i.e., very minor pair).

5.7.2 Calculating the Effect of Mergers on the Observed Disk Fractions

The observed fraction of galaxies with disks (f_{obs}) is related to the true fraction of galaxies with disks (f_{int}), the fraction of central galaxies with a sufficiently massive close pair (f_{pair}) and the probability that, given random sightlines, a close pair will masquerade as a disk ($X_{contamination}$) as:

$$f_{obs} = (1 - f_{int}) \times f_{pair} \times X_{contamination} + f_{int} \tag{5.2}$$

In §5.6.3, we determine that $X_{contamination}$ ranges between 0.4 and 0.8 for pair separations less than 35 kpc, with only a mild dependance on the separation distance (Figure 5.5). We use the Illustris lightcone pair fractions to determine f_{pair} (Figure 5.6).

In Figure 5.7, we show results assuming $X_{contamination} = 0.8$ for all pairs < 35 kpc. The correction is smaller for high mass galaxies ($M_* = 10^{10-11}$ $M_\odot$). Given the observed value of $f_{obs} \simeq 70\%$ (Wisnioski et al., 2015; Simons et al., 2017), the correction is $5 - 10\%$. The correction is more significant for low mass galaxies ($M_* = 10^{9-10}$ $M_\odot$). The observed disk fraction at these masses is $f_{obs} \simeq 50\%$ (Simons et al., 2017) and the correction is a factor of 2 ($f_{int}/f_{obs} \simeq 0.5$). Note that we are using our upper limit for $X_{contamination}$, and so these are upper limits to the correction.

In Figure 5.8, we estimate the intrinsic disk fraction given observed disk fractions

from Simons et al. (2017), assuming that 100% of pairs inside some 3D separation ($d_{contamination}$) masquerade as disks. This is shown as a function of $d_{contamination,3D}$. At high mass, corrections for f_{obs} are only needed if pairs at 15 - 35 kpc contaminate the kinematic maps. For low-mass galaxies, the requirement is more strict — at 5 kpc in separation, pairs begin to significantly affect f_{obs}. We explicitly show the observed value of the disk fraction, with their uncertainties (dashed line and shaded region). The intrinsic disk fraction derived from Eq 5.2, i.e., f_{int}, is shown as a solid line. In the low mass bin, the observed disk fraction is 49 $\pm$ 15%. For $d_{contamination,3D} = 35$ kpc, the intrinsic disk fraction is 25%, implying a factor of two correction. In the high mass bin, the observed disk fraction is 73 $\pm$ 13%. For $d_{contamination,3D} = 35$, the intrinsic disk fraction is 65%, i.e., not significant relative to the error on the observation.

The takeaway from this exercise is that the discrepancy between the true disk fraction and the observed disk fraction, due to merger contamination, is most significant for low-mass galaxies ($10^9 < \mathrm{M_*/M_\odot} < 10^{10}$) — they can be discrepant by as much a factor of two. The correction is less significant for high-mass galaxies ($10^{10} < \mathrm{M_*/M_\odot} < 10^{11}$), not exceeding $\sim 10\%$.

5.8 A High-Redshift Merger through the Eyes of JWST

One can overcome this problem by increasing the spatial sampling of the velocity field, either with the aid of gravitational-lensing (e.g., Mason et al. 2017), adaptive optics (e.g., Law et al. 2009; Wright et al. 2009; Genzel et al. 2011; Swinbank et al. 2012; Mieda et al. 2016), or both (e.g., Jones et al. 2010; Leethochawalit et al. 2016). The situation will dramatically improve with next-generation facilities, largely due to improvements in spatial resolution. The NIRSpec spectrograph on the James Webb Space telescope will offer an unprecedented $0.''1$ resolution ($\sim$1 kpc at $z = 2$).

To illustrate this, we show mock *JWST*/NIRSpec observations in Figure 5.9. The ground-based velocity map presents a relatively simple picture: there exists a smooth single velocity gradient and a central-peak in the velocity dispersion map, both hallmarks of a well-ordered disk. However, NIRSpec reveals a much more complicated story. There are at least 2 coherent velocity gradients, one associated with the orbital motion of the merging companion galaxy and one with the rotation of the central disk, and the velocity dispersion map has several off-center spikes and no smooth profile. Taking a single rotation velocity measurement, i.e., along the steepest velocity gradient suggested from the ground-based map, would give you the *incorrect* answer.

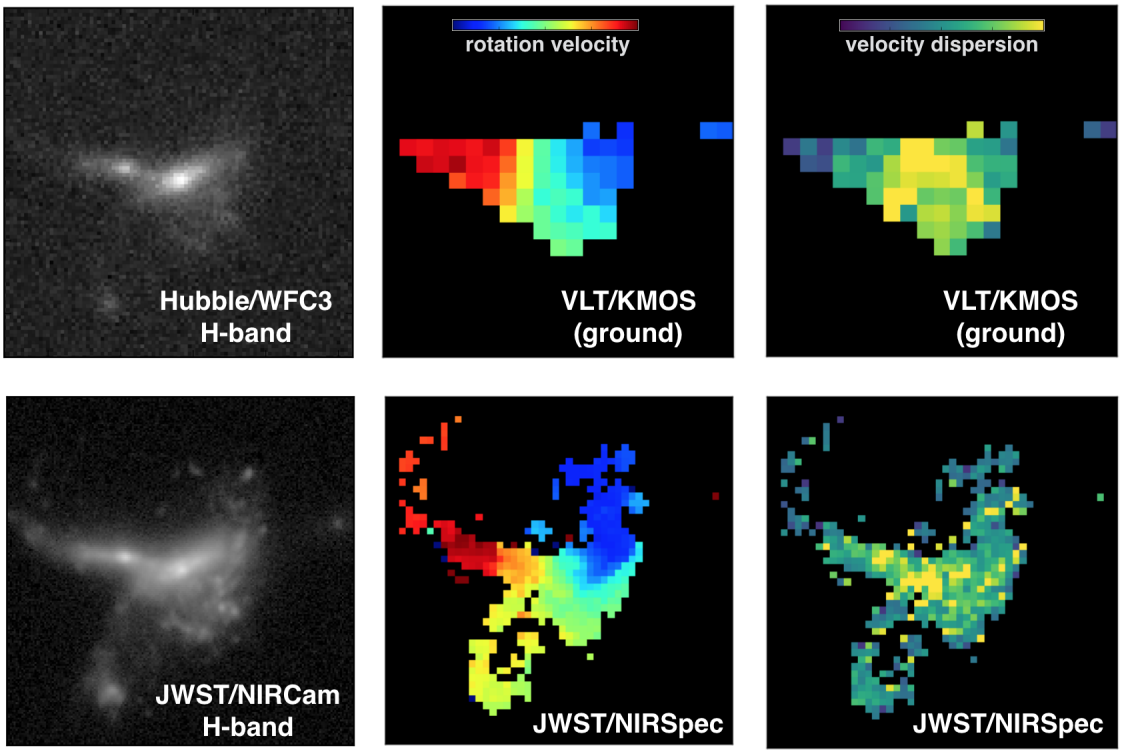

Figure 5.9: Mock images and Hα velocity maps of VELA20 at $z = 1.7$ with current (HST/WFC3, VLT/KMOS) and future facilities (*JWST*/NIRCam, *JWST*/NIRSpec). NIRSpec reveals rich detailed kinematic structure missed in the ground-based data. The velocity gradient in the ground-based map (top middle) is smooth and suggests that this galaxy is a simple disk, while the NIRSpec map (bottom middle) reveals that it is due to the orbital motion of a merger.

5.9 Conclusions

We use the SUNRISE dust-radiative transfer program to generate synthetic images and spectra for 34 zoom-in galaxy formation simulations from the VELA simulation suite (Ceverino et al., 2014), spanning a redshift range $1 < z < 3$. The synthetic observations — UV–NIR imaging and spectral cubes around the Hα emission line — are degraded in noise and resolution to simulate observations with *Hubble*/WFC3 and VLT/KMOS, respectively. Photometric and kinematic properties are measured from the degraded data. We adopt standard observational criteria to determine whether (or not) the synthetic data are consistent with being disk-like systems, i.e., kinematically regular and rotationally-supported. These results are then compared against the intrinsic *truth* of the simulations, i.e., whether they are rotation- or dispersion-supported and whether there is ongoing merger activity. Our conclusions are as follows:

- For isolated disk galaxies, the fraction of sight lines classified as disks from the observational disk criteria is high, $> 80\%$, demonstrating that the observational disk criteria are reliable when applied to regular and isolated disks.

- For galaxies with a disk and a nearby companion galaxy, within 30 kpc, the kinematic major axis is often drawn to the orbit of the merger and, on an average sightline, the derived rotation velocity *overestimates* the true circular velocity of the galaxy.

- For galaxies with no disk and a companion galaxy, the fraction of sight lines misclassified as a disk is high, increasing from $\sim$40 – 60% at 20 kpc separation to 60 – 100% at 10 kpc and below, demonstrating that regular kinematic structure in seeing-limited observations is not *unique* to disks.

- Using theoretically-derived close pair fractions at $z = 2$, we determine that this effect is significant for low mass galaxies — up to a factor of 2 difference between observed and true disk fractions — but insignificant for high mass galaxies.

Chapter 6

Conclusions, Open Questions and Future Directions

6.1 Conclusions

The main conclusions of this thesis are highlighted below.

6.1.1 A Mass of Disk Formation in the Local Universe.

In Chapter 2 and Simons et al. 2015, we examine the rotation velocity (V_{rot}), gas velocity dispersion (σ_g), and morphology of 119 low redshift ($z \sim 0.2$) star-forming galaxies. We find a transition stellar mass in the Tully-Fisher Relation (TFR) at

$\log M_*/M_\odot = 9.5$. Above this mass, nearly all galaxies are rotation-dominated, morphologically disk-like according to quantitative morphology, and lie on a relatively tight TFR. Below this mass, the TFR has significant scatter to low rotation velocity and galaxies can either be rotation-dominated disks on the TFR or asymmetric or compact galaxies which scatter off. We refer to this as the 'mass of disk formation', because above it nearly all star-forming galaxies form disks, whereas below it a galaxy may or may not form a disk.

6.1.2 The Kinematic State of Star-forming Galaxies at z $\sim$ 2.

In Chapter 3 and Simons et al. 2016, we present a $z \sim 2$ kinematic survey with Keck/MOSFIRE, named SIGMA. This sample includes 49 star-forming galaxies at $1.3 < z < 2.5$, the peak of cosmic star-formation. We find that, by $z \sim 2$, massive star-forming galaxies ($\log M_*/M_\odot \geq 10.2$) have assembled primitive disks: their kinematics are dominated by rotation, they are consistent with a marginally stable disk model, and they form a TFR. These massive galaxies have values of V_{rot}/σ_g that are factors of $2-5$ lower than local well-ordered galaxies at similar masses. Low-mass galaxies ($\log M_*/M_\odot \leq 10.2$) at this epoch are still in the early stages of disk assembly: their kinematics are often dominated by gas velocity dispersion and they fall from the TFR to significantly low values of V_{rot}. This kinematic downsizing implies

that the process(es) responsible for disrupting disks at $z \sim 2$ have a stronger effect and/or are more active in low-mass systems.

6.1.3 The emergence of well-ordered disks at z $\sim$ 2. The evolution of the gas velocity Dispersion over the past 10 Billion Years.

In chapter 4 and Simons et al. 2017, we combine kinematics samples from DEEP2 at low redshift (Kassin+ 07; $0.1 < z < 1.2$) and SIGMA at high redshift (Simons+ 16; $1.3 < z < 2.5$) to examine the evolution of kinematics from $z \sim 2$ to now, spanning 10 Gyr of cosmic time. We find that galaxies exhibit remarkably smooth kinematic evolution on average. All galaxies tend toward rotational support with time, and higher mass systems reach it earlier. This is largely due to a mass-independent decline in the velocity dispersion, dropping by a factor of 3 since $z = 2$. At low redshift, nearly all sufficiently massive star-forming galaxies are rotationally supported ($V_{rot} > \sigma_{gas}$). By $z = 2$, 50% and 70% of galaxies are rotationally supported at low ($10^9 - 10^{10}\ M_\odot$) and high ($10^{10} - 10^{11}\ M_\odot$) stellar mass, respectively. For $V_{rot} > 3\,\sigma_{gas}$, the percentage drops below 35% for all masses, indicating that $z = 2$ is a period of nascent disk assembly, during which strong rotational support is only just beginning to emerge.

6.1.4 The Inability to Distinguish Mergers from Disks from Observations of Kinematics.

In chapter 5, we create mock observations of a suite of state-of-the-art galaxy formation simulations. We compare measurements made on mock kinematic maps, as would be seen from the ground, against the intrinsic kinematic state of the simulations. We find that mergers can masquerade as disks in seeing-limited observations — up to 80% of the time in a close-pair separation (< 35 kpc intrinsic) — implying that the fraction of galaxies we measure to be "disks" from seeing-limited observations at $z = 2$ is an *upper-limit* of the true disk fraction. We use theoretically-derived close pair fractions at $z = 2$ to determine how severe this effect is in real observations. We find that it is significant for low mass galaxies — up to a factor of 2 difference between observed and true disk fractions — but insignificant for high mass galaxies.

6.2 Open Questions and Future Directions

Below is a brief listing of interesting, outstanding questions on the formation, evolution and transformation of galaxy structure/kinematics — those for which we can make significant progress over the next decade.

1. **When do galaxies first start rotating? Does the kinematic evolution we measure out to z = 2 continue to higher redshifts?**

As shown in Chapter 4, star-forming galaxies at $z = 2$ are unlike star-forming galaxies today. Gas velocity dispersions are, on average, factors of a few higher. Even still, the majority ($50 - 70\%$) of star-forming galaxies at $z = 2$ have at least marginal rotational support ($V_{rot}/\sigma_g > 1$).

This raises the question: when do galaxies *first* start rotating? Perhaps at $4 \lesssim z \lesssim 9$ will we see the first coherent and sustained spin in galaxies. Pioneering work with ALMA revealed a handful of galaxies at $z \sim 5$ with smooth gradients in their velocity maps (De Breuck et al., 2014; Smit et al., 2017) providing tantalizing hints of rotation (although see Chapter 5). However, with less than five galaxies in total, a demographic picture has yet to emerge. Unfortunately, a large kinematics survey at $z \gtrsim 4$ is not achievable with current ground-based facilities.

Fortunately, *JWST*/NIRSpec is on the horizon. NIRSpec will detect strong optical lines (e.g., Hα and/or [O III]λ5007) out to $z = 9$ at up to $\sim$0.″1 resolution. In its slit-based mode (MSA), NIRSpec can target up to 55 objects at high spectral resolution (STScI documentation). With this multiplexing capability, the MSA will be the primary mode for all large spectroscopic surveys with *JWST*. The strategy developed in Chapter 3 serves as a model for these next-generation surveys.

2. **What process(es) drive/sustain the high random motions observed in**

the ionized gas of high redshift galaxies?

We have yet to determine the physical process(es) that drive and sustain such high values of σ_g at $z = 2$. Krumholz & Burkhart (2016) posit that it is either gravitationally-driven (i.e., gas is regulated in such a way that it remains marginally-stable against gravitational collapse) and/or driven by star-formation feedback (i.e., turbulence induced by supernovae explosions). Each model predicts its own unique dependence of σ_g on gas fraction and star-formation rate. Unfortunately, neither can not be ruled out by current data (e.g., Krumholz & Burkhart 2016; Johnson et al. 2018). An important complication to consider is that low-mass star-forming galaxies are not well-described by a Toomre-critical disk model (Chapter 3; Simons et al. 2016).

One heuristic approach is to push the observed relation between σ_g and z (Chapter 4, Kassin et al. 2012; Simons et al. 2017) to slightly higher redshifts ($z = 3 - 6$). If σ_g is driven by star-formation or star-formation surface density, e.g., energy injection by supernova feedback, clustered young stellar winds, etc. then one might expect σ_g(z) to decline after $z = 2$, following the decline in the cosmic star-formation rate density (Madau & Dickinson, 2014). If, instead, σ_g is driven by galaxy-galaxy mergers or generic clumpy mass accretion, then one might expect $\sigma_g(z)$ to continue to rise past $z = 2$, following the expected elevation in merger activity towards higher redshifts (Rodriguez-Gomez et al., 2015).

3. **Does the kinematics of the ionized gas trace that of the bulk of the baryonic mass, i.e., the cold gas and old stars?**

   The majority of kinematics measurements in the literature, including those in this thesis, are made using strong optical emission lines (e.g., Hα), tracing the $\sim 10^4$ K ionized gas component of galaxies.

   At $z \gtrsim 1$, we have much more limited information on the *spatially-resolved* kinematics of the stars (although see Bezanson et al. 2018 at $z \sim 0.8$), roughly half of the total baryonic mass, or the *spatially-resolved* kinematics of the cold gas (although see e.g., Swinbank et al. 2011; Genzel et al. 2013; Smit et al. 2017; Übler et al. 2018), roughly the other half of the total baryonic mass. This is due to the intractable sensitivity needed to detect stellar absorption lines from the ground, and, until ALMA, limited facilities in the radio/millimeter/sub-millimeter sensitive enough to detect emission lines from cold gas (from e.g., C, CO) at these redshifts.

   Whether, for a large and representative sample, kinematics/dynamics measured from ionized gas reflect the kinematics/dynamics of the *bulk* of the baryonic mass of a galaxy remains an open and important question.

4. **How does the angular momentum content of galaxies evolve with time? What role does the circumgalactic medium play in regulating the re-distribution of angular momentum and the growth of galaxy**

disks?

Angular momentum ($\sum \vec{r} \times \vec{V}$) is a conserved quantity — in a closed box, its *net* magnitude and direction are constant — and is thus as fundamental a galaxy property as mass and energy (Romanowsky & Fall, 2012; Fall & Romanowsky, 2013). However, galaxies are not closed boxes. Their cold gas supply is thought to be regulated through a balance of gas exhaustion through star-formation, inflows and outflows (Bouché et al., 2010; Davé et al., 2012; Dekel & Mandelker, 2014). In order for this to work, cold gas must be continuously supplied by gas-rich mergers, cold streams, cooling of hot gas in the halo, and/or the cycling of gas into and out of the galaxy. Much like energy and mass, all of these can significantly alter the angular momentum content of the gas (Kimm et al., 2011; Übler et al., 2014; Genel et al., 2015; Danovich et al., 2015).

Jiang et al. (2018) find that the spin of dark matter and baryonic matter are uncorrelated in simulations at $z > 1$, i.e. consistent with an open-box and/or angular momentum exchange between dark and baryonic matter (see also Kimm et al. 2011). Shockingly, Genel et al. (2015) find that the angular momentum retention factor (i.e., angular momentum retained from primordial tidal torques) is near-unity for simulated late-type galaxies by $z = 0$. How does this happen?

To better understand the exchange of angular momentum between gas and dark matter, we must look to the circumgalactic medium (CGM). The CGM has gained much attention in recent years (see review by Tumlinson et al.

2017). A significant fraction ($\sim$ 80%) of the total "baryon budget" (i.e., $M_{halo} \times \Omega_{baryon}/\Omega_{matter}$) of galaxies/halos resides in the CGM (Werk et al., 2014), in the form of a kinematically-complex (Werk et al., 2016) and multi-phase gas (Sembach et al., 2003; Werk et al., 2014).

The CGM is the arena which, arguably, most determines how the gas supply in galaxies is regulated (important for understanding star-formation, quenching and the stellar mass growth of galaxies) and how the angular momentum and orbital energy of cycling gas/cold flows is deposited onto galaxies (important for the size growth and structural transformation of galaxies).

New and upcoming UV-optical-NIR facilities, *HST*, MUSE, KCWI, GMT, TMT, LUVOIR, will allow us to measure the 2D emission line structure in the CGM, in turn revealing the gas ionization state, metallicity and — most important for understanding angular momentum exhange — mass and kinematic structure. Mock observations of simulations that accurately capture the complex physics and multi-phase and multi-scale nature of the CGM will play a critical role in bridging these data back to the physical models.

Somehow, through the chaotic exchange of angular momentum between the CGM/IGM/dark halo/galaxy, the galaxy is kept (or put back) in spin equilibrium with the dark matter (i.e., the initial assumption of the standard disk formation picture). Understanding how this happens is an open question, and one which mystifies this author.

6.3 Final Remarks

This decade brought forth tremendous advances in our understanding of galaxy assembly at $z = 2$. Three billion years after the Big Bang, nearly two-thirds of the star-forming galaxy population have significant dynamical support from random motions. This is a puzzling result. High random gas motions are not sustainable — why haven't all galaxies formed thin gas disks by $z = 2$? With new and upcoming near-/mid- infrared and submillimeter facilities (*JWST*, ALMA, TMT, GMT) and an emerging synergy between observations and state-of-the-art simulations, this next decade promises to shed light on this mystery.

Bibliography

Abraham, R. G., Tanvir, N. R., Santiago, B. X., et al. 1996, MNRAS, 279, L47

Abraham, R. G., Valdes, F., Yee, H. K. C., & van den Bergh, S. 1994, ApJ, 432, 75

Abraham, R. G., van den Bergh, S., & Nair, P. 2003, ApJ, 588, 218

Agertz, O., & Kravtsov, A. V. 2016, ApJ, 824, 79

Amorín, R., Vílchez, J. M., Hägele, G. F., et al. 2012, ApJ, 754, L22

Arribas, S., Colina, L., Bellocchi, E., Maiolino, R., & Villar-Martín, M. 2014, A&A, 568, A14

Astropy Collaboration, Robitaille, T. P., Tollerud, E. J., et al. 2013, A&A, 558, A33

Aumer, M., Burkert, A., Johansson, P. H., & Genzel, R. 2010, ApJ, 719, 1230

Aumer, M., White, S. D. M., Naab, T., & Scannapieco, C. 2013, MNRAS, 434, 3142

Barnes, J. E., & Hernquist, L. 1996, ApJ, 471, 115

BIBLIOGRAPHY

Barrera-Ballesteros, J. K., García-Lorenzo, B., Falcón-Barroso, J., et al. 2015, A&A, 582, A21

Barro, G., Trump, J. R., Koo, D. C., et al. 2014, ApJ, 795, 145

Barton, E. J., Geller, M. J., Bromley, B. C., van Zee, L., & Kenyon, S. J. 2001, AJ, 121, 625

Begeman, K. G. 1987, PhD thesis, , Kapteyn Institute, (1987)

Begum, A., Chengalur, J. N., Karachentsev, I. D., & Sharina, M. E. 2008a, MNRAS, 386, 138

Begum, A., Chengalur, J. N., Karachentsev, I. D., Sharina, M. E., & Kaisin, S. S. 2008b, MNRAS, 386, 1667

Bell, E. F., & de Jong, R. S. 2001, ApJ, 550, 212

Bell, E. F., Papovich, C., Wolf, C., et al. 2005, ApJ, 625, 23

Bershady, M. A., Verheijen, M. A. W., Swaters, R. A., et al. 2010, ApJ, 716, 198

Bertin, E., & Arnouts, S. 1996, A&AS, 117, 393

Bezanson, R., van der Wel, A., Pacifici, C., et al. 2018, ApJ, 858, 60

Blumenthal, G. R., Faber, S. M., Primack, J. R., & Rees, M. J. 1984, Nature, 311, 517

BIBLIOGRAPHY

Bond, J. R., Kofman, L., & Pogosyan, D. 1996, Nature, 380, 603

Bothwell, M. S., Kennicutt, R. C., & Lee, J. C. 2009, MNRAS, 400, 154

Bouché, N., Dekel, A., Genzel, R., et al. 2010, ApJ, 718, 1001

Bradford, J. D., Geha, M. C., & van den Bosch, F. C. 2016, ApJ, 832, 11

Brammer, G. B., van Dokkum, P. G., & Coppi, P. 2008, ApJ, 686, 1503

Brammer, G. B., van Dokkum, P. G., Franx, M., et al. 2012, ApJS, 200, 13

Brinchmann, J., & Ellis, R. S. 2000, ApJ, 536, L77

Brooks, A. M., Governato, F., Quinn, T., Brook, C. B., & Wadsley, J. 2009, ApJ, 694, 396

Bruzual, G., & Charlot, S. 2003, Monthly Notices of the Royal Astronomical Society, 344, 1000

Buitrago, F., Conselice, C. J., Epinat, B., et al. 2014, MNRAS, 439, 1494

Bundy, K., Ellis, R. S., Conselice, C. J., et al. 2006, ApJ, 651, 120

Bundy, K., Bershady, M. A., Law, D. R., et al. 2015, ApJ, 798, 7

Calzetti, D., Armus, L., Bohlin, R. C., et al. 2000, ApJ, 533, 682

Cannon, J. M., McClure-Griffiths, N. M., Skillman, E. D., & Côté, S. 2004, ApJ, 607, 274

BIBLIOGRAPHY

Catinella, B., Kauffmann, G., Schiminovich, D., et al. 2012, MNRAS, 420, 1959

Ceverino, D., Dekel, A., & Bournaud, F. 2010, Monthly Notices of the Royal Astronomical Society, 404, 2151

Ceverino, D., Dekel, A., Mandelker, N., et al. 2012, MNRAS, 420, 3490

Ceverino, D., Klypin, A., Klimek, E. S., et al. 2014, Monthly Notices of the Royal Astronomical Society, 442, 1545

Ceverino, D., Primack, J., & Dekel, A. 2015, MNRAS, 453, 408

Ceverino, D., Primack, J., Dekel, A., & Kassin, S. A. 2017, MNRAS, 467, 2664

Chabrier, G. 2003, Publications of the Astronomical Society of the Pacific, 115, 763

Chary, R., & Elbaz, D. 2001, ApJ, 556, 562

Conselice, C. J., Bundy, K., Ellis, R. S., et al. 2005, ApJ, 628, 160

Contini, T., Garilli, B., Le Fèvre, O., et al. 2012, A&A, 539, A91

Contini, T., Epinat, B., Bouché, N., et al. 2016, A&A, 591, A49

Cortese, L., Fogarty, L. M. R., Ho, I.-T., et al. 2014, ApJ, 795, L37

Courteau, S., Dutton, A. A., van den Bosch, F. C., et al. 2007, ApJ, 671, 203

Covington, M. D., Kassin, S. A., Dutton, A. A., et al. 2010, ApJ, 710, 279

Cowie, L. L., Songaila, A., Hu, E. M., & Cohen, J. G. 1996, AJ, 112, 839

BIBLIOGRAPHY

Cresci, G., Hicks, E. K. S., Genzel, R., et al. 2009, ApJ, 697, 115

Daddi, E., Elbaz, D., Walter, F., et al. 2010a, ApJ, 714, L118

Daddi, E., Bournaud, F., Walter, F., et al. 2010b, ApJ, 713, 686

Dahlen, T., Mobasher, B., Faber, S. M., et al. 2013, ApJ, 775, 93

Danovich, M., Dekel, A., Hahn, O., Ceverino, D., & Primack, J. 2015, MNRAS, 449, 2087

Davé, R., Finlator, K., & Oppenheimer, B. D. 2012, MNRAS, 421, 98

Davies, R., Förster Schreiber, N. M., Cresci, G., et al. 2011, ApJ, 741, 69

Davis, M., Guhathakurta, P., Konidaris, N. P., et al. 2007, ApJ, 660, L1

de Blok, W. J. G., Walter, F., Brinks, E., et al. 2008, AJ, 136, 2648

De Breuck, C., Williams, R. J., Swinbank, M., et al. 2014, Astronomy and Astrophysics, 565, A59

De Rossi, M. E., Tissera, P. B., & Pedrosa, S. E. 2012, A&A, 546, A52

Dekel, A., & Mandelker, N. 2014, MNRAS, 444, 2071

Dekel, A., Sari, R., & Ceverino, D. 2009, ApJ, 703, 785

Dekel, A., & Silk, J. 1986, ApJ, 303, 39

Dib, S., Bell, E., & Burkert, A. 2006, ApJ, 638, 797

BIBLIOGRAPHY

Dopita, M. A., Groves, B. A., Fischera, J., et al. 2005, ApJ, 619, 755

Doroshkevich, A. G. 1970, Astrofizika, 6, 581

Draine, B. T., & Li, A. 2007, ApJ, 657, 810

Dutton, A. A., van den Bosch, F. C., Dekel, A., & Courteau, S. 2007, ApJ, 654, 27

Dutton, A. A., van den Bosch, F. C., Faber, S. M., et al. 2011, MNRAS, 410, 1660

El-Badry, K., Wetzel, A., Geha, M., et al. 2016, ApJ, 820, 131

Elbaz, D., Dickinson, M., Hwang, H. S., et al. 2011, A&A, 533, A119

Elmegreen, B. G., & Burkert, A. 2010, ApJ, 712, 294

Epinat, B., Amram, P., Balkowski, C., & Marcelin, M. 2010, MNRAS, 401, 2113

Epinat, B., Amram, P., & Marcelin, M. 2008, MNRAS, 390, 466

Erb, D. K., Steidel, C. C., Shapley, A. E., et al. 2006, ApJ, 646, 107

Faber, S. M., & Jackson, R. E. 1976, ApJ, 204, 668

Faber, S. M., Phillips, A. C., Kibrick, R. I., et al. 2003, in Proc. SPIE, Vol. 4841, Instrument Design and Performance for Optical/Infrared Ground-based Telescopes, ed. M. Iye & A. F. M. Moorwood, 1657–1669

Fall, S. M., & Efstathiou, G. 1980, MNRAS, 193, 189

Fall, S. M., & Romanowsky, A. J. 2013, ApJ, 769, L26

BIBLIOGRAPHY

Flores, H., Hammer, F., Puech, M., Amram, P., & Balkowski, C. 2006, A&A, 455, 107

Ford, A. B., Davé, R., Oppenheimer, B. D., et al. 2014, MNRAS, 444, 1260

Förster Schreiber, N. M., Genzel, R., Lehnert, M. D., et al. 2006, ApJ, 645, 1062

Förster Schreiber, N. M., Genzel, R., Bouché, N., et al. 2009, ApJ, 706, 1364

Galametz, A., Grazian, A., Fontana, A., et al. 2013, ApJS, 206, 10

Gallazzi, A., Charlot, S., Brinchmann, J., & White, S. D. M. 2006, MNRAS, 370, 1106

García-Lorenzo, B., Márquez, I., Barrera-Ballesteros, J. K., et al. 2015, A&A, 573, A59

Garrido, O., Marcelin, M., Amram, P., & Boissin, O. 2003, A&A, 399, 51

Genel, S., Dekel, A., & Cacciato, M. 2012, MNRAS, 425, 788

Genel, S., Fall, S. M., Hernquist, L., et al. 2015, ApJ, 804, L40

Genel, S., Vogelsberger, M., Springel, V., et al. 2014, MNRAS, 445, 175

Genzel, R., Tacconi, L. J., Eisenhauer, F., et al. 2006, Nature, 442, 786

Genzel, R., Burkert, A., Bouché, N., et al. 2008, ApJ, 687, 59

Genzel, R., Newman, S., Jones, T., et al. 2011, ApJ, 733, 101

BIBLIOGRAPHY

Genzel, R., Tacconi, L. J., Kurk, J., et al. 2013, ApJ, 773, 68

Genzel, R., Tacconi, L. J., Lutz, D., et al. 2015, ApJ, 800, 20

Genzel, R., Schreiber, N. M. F., Übler, H., et al. 2017, Nature, 543, 397

Glazebrook, K. 2013, Publications of the Astronomical Society of Australia, 30, e056

Gnerucci, A., Marconi, A., Cresci, G., et al. 2011, A&A, 528, A88

Gonçalves, T. S., Basu-Zych, A., Overzier, R., et al. 2010, ApJ, 724, 1373

Gordon, K. D., Clayton, G. C., Misselt, K. A., Landolt, A. U., & Wolff, M. J. 2003, ApJ, 594, 279

Governato, F., Brook, C. B., Brooks, A. M., et al. 2009, MNRAS, 398, 312

Green, A. W., Glazebrook, K., McGregor, P. J., et al. 2014, MNRAS, 437, 1070

Grogin, N. A., Kocevski, D. D., Faber, S. M., et al. 2011, The Astrophysical Journal Supplement Series, 197, 35

Groves, B., Dopita, M. A., Sutherland, R. S., et al. 2008, ApJS, 176, 438

Guo, Y., Ferguson, H. C., Giavalisco, M., et al. 2013, ApJS, 207, 24

Hammer, F., Flores, H., Elbaz, D., et al. 2005, A&A, 430, 115

Hammer, F., Flores, H., Puech, M., et al. 2009, A&A, 507, 1313

Harrison, C. M., Johnson, H. L., Swinbank, A. M., et al. 2017, MNRAS, 467, 1965

BIBLIOGRAPHY

Heckman, T. M., Hoopes, C. G., Seibert, M., et al. 2005, ApJ, 619, L35

Hernquist, L., & Mihos, J. C. 1995, ApJ, 448, 41

Hibbard, J. E., van Gorkom, J. H., Rupen, M. P., & Schiminovich, D. 2001, in Astronomical Society of the Pacific Conference Series, Vol. 240, Gas and Galaxy Evolution, ed. J. E. Hibbard, M. Rupen, & J. H. van Gorkom

Hopkins, P. F., Cox, T. J., Younger, J. D., & Hernquist, L. 2009, ApJ, 691, 1168

Hoyle, F. 1951, in Problems of Cosmical Aerodynamics, 195

Huertas-Company, M., Bernardi, M., Pérez-González, P. G., et al. 2016, MNRAS, 462, 4495

Hung, C.-L., Hayward, C. C., Smith, H. A., et al. 2016, ApJ, 816, 99

Hung, C.-L., Rich, J. A., Yuan, T., et al. 2015, ApJ, 803, 62

Hunter, D. A., Ficut-Vicas, D., Ashley, T., et al. 2012, AJ, 144, 134

Inoue, S., Dekel, A., Mandelker, N., et al. 2016, MNRAS, 456, 2052

Jiang, F., Dekel, A., Kneller, O., et al. 2018, ArXiv e-prints, arXiv:1804.07306

Johnson, H. L., Harrison, C. M., Swinbank, A. M., et al. 2018, MNRAS, 474, 5076

Jones, T. A., Swinbank, A. M., Ellis, R. S., Richard, J., & Stark, D. P. 2010, Monthly Notices of the Royal Astronomical Society, 404, 1247

BIBLIOGRAPHY

Jonsson, P. 2006, Monthly Notices of the Royal Astronomical Society, 372, 2

Jonsson, P., Groves, B. A., & Cox, T. J. 2010, MNRAS, 403, 17

Jonsson, P., & Primack, J. R. 2010, New Astronomy, 15, 509

Joung, M. K. R., & Mac Low, M.-M. 2006, ApJ, 653, 1266

Juneau, S., Glazebrook, K., Crampton, D., et al. 2005, ApJ, 619, L135

Kannappan, S. J., Fabricant, D. G., & Franx, M. 2002, AJ, 123, 2358

Kassin, S. A., Brooks, A., Governato, F., Weiner, B. J., & Gardner, J. P. 2014, ApJ, 790, 89

Kassin, S. A., de Jong, R. S., & Weiner, B. J. 2006, ApJ, 643, 804

Kassin, S. A., Weiner, B. J., Faber, S. M., et al. 2007, ApJ, 660, L35

—. 2012, ApJ, 758, 106

Kennicutt, Jr., R. C. 1998a, ARA&A, 36, 189

—. 1998b, ApJ, 498, 541

Kimm, T., Devriendt, J., Slyz, A., et al. 2011, ArXiv e-prints, arXiv:1106.0538

Kirby, E. N., Bullock, J. S., Boylan-Kolchin, M., Kaplinghat, M., & Cohen, J. G. 2014, MNRAS, 439, 1015

Klypin, A. A., & Shandarin, S. F. 1983, MNRAS, 204, 891

BIBLIOGRAPHY

Koekemoer, A. M., Faber, S. M., Ferguson, H. C., et al. 2011, The Astrophysical Journal Supplement Series, 197, 36

Krajnović, D., Cappellari, M., de Zeeuw, P. T., & Copin, Y. 2006, MNRAS, 366, 787

Kravtsov, A. V., Klypin, A. A., & Khokhlov, A. M. 1997, The Astrophysical Journal Supplement Series, 111, 73

Kriek, M., van Dokkum, P. G., Labbé, I., et al. 2009, ApJ, 700, 221

Kriek, M., Shapley, A. E., Reddy, N. A., et al. 2015, ApJS, 218, 15

Kronberger, T., Kapferer, W., Schindler, S., & Ziegler, B. L. 2007, A&A, 473, 761

Kroupa, P. 2001, MNRAS, 322, 231

Krumholz, M. R., & Burkhart, B. 2016, MNRAS, 458, 1671

Lang, P., Förster Schreiber, N. M., Genzel, R., et al. 2017, ApJ, 840, 92

Law, D. R., Shapley, A. E., Steidel, C. C., et al. 2012, Nature, 487, 338

Law, D. R., Steidel, C. C., Erb, D. K., et al. 2007, ApJ, 669, 929

—. 2009, The Astrophysical Journal, 697, 2057

Lee, J. C., Kennicutt, Jr., R. C., Funes, S. J. J. G., Sakai, S., & Akiyama, S. 2009, ApJ, 692, 1305

Leethochawalit, N., Jones, T. A., Ellis, R. S., et al. 2016, ApJ, 820, 84

BIBLIOGRAPHY

Lehnert, M. D., Nesvadba, N. P. H., Le Tiran, L., et al. 2009, ApJ, 699, 1660

Leitherer, C., Schaerer, D., Goldader, J. D., et al. 1999, ApJS, 123, 3

Lelli, F., Verheijen, M., & Fraternali, F. 2014, A&A, 566, A71

Lemoine-Busserolle, M., & Lamareille, F. 2010, MNRAS, 402, 2291

Li, C., & White, S. D. M. 2009, MNRAS, 398, 2177

Lin, L., Koo, D. C., Weiner, B. J., et al. 2007, ApJ, 660, L51

Livermore, R. C., Jones, T. A., Richard, J., et al. 2015, Monthly Notices of the Royal Astronomical Society, 450, 1812

Lotz, J. M., Jonsson, P., Cox, T. J., et al. 2011, ApJ, 742, 103

Lotz, J. M., Madau, P., Giavalisco, M., Primack, J., & Ferguson, H. C. 2006, ApJ, 636, 592

Lotz, J. M., Primack, J., & Madau, P. 2004, AJ, 128, 163

Lotz, J. M., Davis, M., Faber, S. M., et al. 2008, ApJ, 672, 177

Ma, X., Hopkins, P. F., Wetzel, A. R., et al. 2017, MNRAS, 467, 2430

Mac Low, M.-M., & Ferrara, A. 1999, ApJ, 513, 142

Madau, P., & Dickinson, M. 2014, ARA&A, 52, 415

Magnelli, B., Popesso, P., Berta, S., et al. 2013, A&A, 553, A132

BIBLIOGRAPHY

Mahajan, S., Drinkwater, M. J., Driver, S., et al. 2015, MNRAS, 446, 2967

Mandelker, N., Dekel, A., Ceverino, D., et al. 2017, MNRAS, 464, 635

—. 2014, MNRAS, 443, 3675

Mantha, K. B., McIntosh, D. H., Brennan, R., et al. 2018, MNRAS, 475, 1549

Mason, C. A., Treu, T., Fontana, A., et al. 2017, The Astrophysical Journal, 838, 14

Masters, D., & Capak, P. 2011, PASP, 123, 638

Masters, K. L., Springob, C. M., & Huchra, J. P. 2008, AJ, 135, 1738

Mateo, M. L. 1998, ARA&A, 36, 435

McConnachie, A. W. 2012, AJ, 144, 4

McGaugh, S. S. 2005, ApJ, 632, 859

McKee, C. F., & Ostriker, J. P. 1977, ApJ, 218, 148

McLean, I. S., Steidel, C. C., Epps, H., et al. 2010, in Proc. SPIE, Vol. 7735, Ground-based and Airborne Instrumentation for Astronomy III, 77351E–77351E–12

McLean, I. S., Steidel, C. C., Epps, H. W., et al. 2012, in Proc. SPIE, Vol. 8446, Ground-based and Airborne Instrumentation for Astronomy IV, 84460J

Mieda, E., Wright, S. A., Larkin, J. E., et al. 2016, ApJ, 831, 78

Miller, S. H., Bundy, K., Sullivan, M., Ellis, R. S., & Treu, T. 2011, ApJ, 741, 115

Miller, S. H., Ellis, R. S., Newman, A. B., & Benson, A. 2014, ApJ, 782, 115

Miller, S. H., Ellis, R. S., Sullivan, M., et al. 2012, ApJ, 753, 74

Mo, H. J., Mao, S., & White, S. D. M. 1998, MNRAS, 295, 319

Mobasher, B., Dahlen, T., Ferguson, H. C., et al. 2015, ApJ, 808, 101

Momcheva, I. G., Brammer, G. B., van Dokkum, P. G., et al. 2016, ApJS, 225, 27

Moody, C. E., Guo, Y., Mandelker, N., et al. 2014, MNRAS, 444, 1389

Morris, A. M., Kocevski, D. D., Trump, J. R., et al. 2015, AJ, 149, 178

Mortlock, A., Conselice, C. J., Hartley, W. G., et al. 2013, MNRAS, 433, 1185

—. 2015, MNRAS, 447, 2

Moster, B. P., Naab, T., & White, S. D. M. 2013, MNRAS, 428, 3121

Muratov, A. L., Kereš, D., Faucher-Giguère, C.-A., et al. 2017, MNRAS, 468, 4170

Muzzin, A., Marchesini, D., Stefanon, M., et al. 2013, ApJ, 777, 18

Naab, T., & Burkert, A. 2003, ApJ, 597, 893

Navarro, J. F., & Steinmetz, M. 2000, ApJ, 538, 477

Nelson, E. J., van Dokkum, P. G., Förster Schreiber, N. M., et al. 2016, ApJ, 828, 27

Newman, J. A., Cooper, M. C., Davis, M., et al. 2013a, ApJS, 208, 5

Newman, S. F., Genzel, R., Förster Schreiber, N. M., et al. 2013b, ApJ, 767, 104

Noeske, K. G., Weiner, B. J., Faber, S. M., et al. 2007, ApJ, 660, L43

Olivares, V., Treister, E., Privon, G. C., et al. 2016, ApJ, 827, 57

Ott, J., Stilp, A. M., Warren, S. R., et al. 2012, AJ, 144, 123

Papovich, C., Labbé, I., Quadri, R., et al. 2015, ApJ, 803, 26

Patil, A., Huard, D., & Fonnesbeck, C. 2010, Journal of Statistical Software, 35, 1

Peebles, P. J. E. 1969, ApJ, 155, 393

—. 1980, The large-scale structure of the universe

Peng, C. Y., Ho, L. C., Impey, C. D., & Rix, H.-W. 2010, AJ, 139, 2097

Pérez-Gallego, J., Guzmán, R., Castillo-Morales, A., et al. 2011, MNRAS, 418, 2350

Pérez-González, P. G., Rieke, G. H., Villar, V., et al. 2008, ApJ, 675, 234

Peth, M. A., Lotz, J. M., Freeman, P. E., et al. 2016, MNRAS, 458, 963

Pizagno, J., Prada, F., Weinberg, D. H., et al. 2005, ApJ, 633, 844

—. 2007, AJ, 134, 945

Price, S. H., Kriek, M., Shapley, A. E., et al. 2016, ApJ, 819, 80

Puech, M., Hammer, F., Flores, H., et al. 2010, A&A, 510, A68

Puech, M., Flores, H., Hammer, F., et al. 2008, A&A, 484, 173

Rampazzo, R., Plana, H., Amram, P., et al. 2005, MNRAS, 356, 1177

Reddy, N. A., Pettini, M., Steidel, C. C., et al. 2012, ApJ, 754, 25

Rees, M. J., & Ostriker, J. P. 1977, MNRAS, 179, 541

Reyes, R., Mandelbaum, R., Gunn, J. E., Pizagno, J., & Lackner, C. N. 2011, MNRAS, 417, 2347

Roberts, M. S., & Haynes, M. P. 1994, ARA&A, 32, 115

Robertson, B., Bullock, J. S., Cox, T. J., et al. 2006, ApJ, 645, 986

Rodriguez-Gomez, V., Genel, S., Vogelsberger, M., et al. 2015, MNRAS, 449, 49

Rodriguez-Gomez, V., Sales, L. V., Genel, S., et al. 2017, MNRAS, 467, 3083

Rodríguez-Puebla, A., Behroozi, P., Primack, J., et al. 2016, MNRAS, 462, 893

Rodríguez-Puebla, A., Primack, J. R., Avila-Reese, V., & Faber, S. M. 2017, MNRAS, 470, 651

Romanowsky, A. J., & Fall, S. M. 2012, ApJS, 203, 17

Roychowdhury, S., Chengalur, J. N., Begum, A., & Karachentsev, I. D. 2010, MNRAS, 404, L60

Sales, L. V., Navarro, J. F., Theuns, T., et al. 2012, MNRAS, 423, 1544

BIBLIOGRAPHY

Santini, P., Fontana, A., Grazian, A., et al. 2012, A&A, 538, A33

Scannapieco, C., Gadotti, D. A., Jonsson, P., & White, S. D. M. 2010, MNRAS, 407, L41

Scoville, N., Lee, N., Vanden Bout, P., et al. 2017, ApJ, 837, 150

Sembach, K. R., Wakker, B. P., Savage, B. D., et al. 2003, ApJS, 146, 165

Shapiro, K. L., Genzel, R., Förster Schreiber, N. M., et al. 2008, ApJ, 682, 231

Sharples, R. M., Bender, R., Lehnert, M. D., et al. 2004, in Proc. SPIE, Vol. 5492, Ground-based Instrumentation for Astronomy, ed. A. F. M. Moorwood & M. Iye, 1179–1186

Shields, G. A. 1990, ARA&A, 28, 525

Silk, J. 1997, ApJ, 481, 703

Simard, L., Willmer, C. N. A., Vogt, N. P., et al. 2002, ApJS, 142, 1

Simons, R. C., Kassin, S. A., Weiner, B. J., et al. 2015, Monthly Notices of the Royal Astronomical Society, 452, 986

Simons, R. C., Kassin, S. A., Trump, J. R., et al. 2016, The Astrophysical Journal, 830, 14

Simons, R. C., Kassin, S. A., Weiner, B. J., et al. 2017, The Astrophysical Journal, 843, 46

Smit, R., Bouwens, R. J., Carniani, S., et al. 2017, ArXiv e-prints, arXiv:1706.04614

Snyder, G. F., Lotz, J., Moody, C., et al. 2015, MNRAS, 451, 4290

Snyder, G. F., Lotz, J. M., Rodriguez-Gomez, V., et al. 2017, MNRAS, 468, 207

Somerville, R. S., & Davé, R. 2015, ARA&A, 53, 51

Somerville, R. S., & Primack, J. R. 1999, MNRAS, 310, 1087

Speagle, J. S., Steinhardt, C. L., Capak, P. L., & Silverman, J. D. 2014, ApJS, 214, 15

Stark, D. V., McGaugh, S. S., & Swaters, R. A. 2009, AJ, 138, 392

Stewart, K. R., Brooks, A. M., Bullock, J. S., et al. 2013, ApJ, 769, 74

Stott, J. P., Swinbank, A. M., Johnson, H. L., et al. 2016, MNRAS, 457, 1888

Straatman, C. M. S., Glazebrook, K., Kacprzak, G. G., et al. 2017, ApJ, 839, 57

Strickland, D. K., & Heckman, T. M. 2009, ApJ, 697, 2030

Swaters, R. A., Sancisi, R., van Albada, T. S., & van der Hulst, J. M. 2009, A&A, 493, 871

Swaters, R. A., van Albada, T. S., van der Hulst, J. M., & Sancisi, R. 2002, A&A, 390, 829

Swinbank, A. M., Sobral, D., Smail, I., et al. 2012, MNRAS, 426, 935

Swinbank, A. M., Papadopoulos, P. P., Cox, P., et al. 2011, ApJ, 742, 11

Tacchella, S., Dekel, A., Carollo, C. M., et al. 2016a, MNRAS, 458, 242

—. 2016b, MNRAS, 457, 2790

Tacconi, L. J., Neri, R., Genzel, R., et al. 2013, ApJ, 768, 74

Thuan, T. X., Hibbard, J. E., & Lévrier, F. 2004, AJ, 128, 617

Tomassetti, M., Dekel, A., Mandelker, N., et al. 2016, MNRAS, 458, 4477

Toomre, A. 1977, in Evolution of Galaxies and Stellar Populations, ed. B. M. Tinsley & R. B. G. Larson, D. Campbell, 401

Torres-Flores, S., Epinat, B., Amram, P., Plana, H., & Mendes de Oliveira, C. 2011, MNRAS, 416, 1936

Trump, J. R., Konidaris, N. P., Barro, G., et al. 2013, The Astrophysical Journal Letters, 763, L6

Tully, R. B., & Fisher, J. R. 1977, A&A, 54, 661

Tumlinson, J., Peeples, M. S., & Werk, J. K. 2017, ARA&A, 55, 389

Turk, M. J., Smith, B. D., Oishi, J. S., et al. 2011, ApJS, 192, 9

Turner, O. J., Harrison, C. M., Cirasuolo, M., et al. 2017a, ArXiv e-prints, arXiv:1711.03604

Turner, O. J., Cirasuolo, M., Harrison, C. M., et al. 2017b, MNRAS, 471, 1280

Übler, H., Naab, T., Oser, L., et al. 2014, MNRAS, 443, 2092

Übler, H., Förster Schreiber, N. M., Genzel, R., et al. 2017, ApJ, 842, 121

Übler, H., Genzel, R., Tacconi, L. J., et al. 2018, ApJ, 854, L24

Vaduvescu, O., McCall, M. L., Richer, M. G., & Fingerhut, R. L. 2005, AJ, 130, 1593

van der Wel, A., Bell, E. F., Häussler, B., et al. 2012, The Astrophysical Journal Supplement Series, 203, 24

van der Wel, A., Franx, M., van Dokkum, P. G., et al. 2014a, ApJ, 788, 28

van der Wel, A., Chang, Y.-Y., Bell, E. F., et al. 2014b, ApJ, 792, L6

van Zee, L., Salzer, J. J., & Skillman, E. D. 2001, AJ, 122, 121

van Zee, L., Skillman, E. D., & Salzer, J. J. 1998, AJ, 116, 1186

Vergani, D., Epinat, B., Contini, T., et al. 2012, A&A, 546, A118

Verheijen, M. A. W. 2001, ApJ, 563, 694

Vogelsberger, M., Genel, S., Springel, V., et al. 2014, MNRAS, 444, 1518

Walter, F., Brinks, E., de Blok, W. J. G., et al. 2008, AJ, 136, 2563

Weiner, B. J., Willmer, C. N. A., Faber, S. M., et al. 2006a, ApJ, 653, 1027

—. 2006b, ApJ, 653, 1049

Weiner, B. J., Papovich, C., Bundy, K., et al. 2007, ApJ, 660, L39

Weingartner, J. C., & Draine, B. T. 2001, ApJ, 548, 296

Werk, J. K., Prochaska, J. X., Tumlinson, J., et al. 2014, ApJ, 792, 8

Werk, J. K., Prochaska, J. X., Cantalupo, S., et al. 2016, ApJ, 833, 54

Wheeler, C., Pace, A. B., Bullock, J. S., et al. 2017, MNRAS, 465, 2420

Whitaker, K. E., van Dokkum, P. G., Brammer, G., & Franx, M. 2012, ApJ, 754, L29

Whitaker, K. E., Franx, M., Leja, J., et al. 2014, ApJ, 795, 104

White, S. D. M. 1984, ApJ, 286, 38

White, S. D. M., & Frenk, C. S. 1991, ApJ, 379, 52

White, S. D. M., & Rees, M. J. 1978, MNRAS, 183, 341

Wirth, G. D., Trump, J. R., Barro, G., et al. 2015, AJ, 150, 153

Wisnioski, E., Glazebrook, K., Blake, C., et al. 2011, MNRAS, 417, 2601

Wisnioski, E., Förster Schreiber, N. M., Wuyts, S., et al. 2015, The Astrophysical Journal, 799, 209

Wright, S. A., Larkin, J. E., Law, D. R., et al. 2009, ApJ, 699, 421

Wright, S. A., Larkin, J. E., Barczys, M., et al. 2007, ApJ, 658, 78

Wuyts, S., Förster Schreiber, N. M., Lutz, D., et al. 2011, ApJ, 738, 106

Yegorova, I. A., & Salucci, P. 2007, MNRAS, 377, 507

Young, L. M., van Zee, L., Lo, K. Y., Dohm-Palmer, R. C., & Beierle, M. E. 2003, ApJ, 592, 111

Zel'dovich, Y. B. 1970, A&A, 5, 84

Zhao, Y., Gao, Y., & Gu, Q. 2013, ApJ, 764, 44

Zolotov, A., Dekel, A., Mandelker, N., et al. 2015, MNRAS, 450, 2327

Vita

Raymond Clifford Simons was born on December 11, 1989 in New Brunswick, New Jersey to Donna Dee Simons (Née Dixon) and Derrick Michael Simons. He received his high school diploma from Charlotte High School in 2008 and received B.Sc. degrees in Astronomy & Astrophysics and Physics from Florida Institute of Technology in 2012. He enrolled in the Physics & Astronomy Ph.D. program at Johns Hopkins University in 2012. This thesis was defended on June 21, 2018.